Diss. ETH No. 12925

Photoacoustic and Photothermal Laser Spectroscopy Applied to Trace Gas Detection and Molecular Dynamics

A dissertation submitted to the *Swiss Federal Institute of Technology* ***ETH*** *Zürich*

for the degree of *Doctor of Natural Sciences*

presented by ***Irio Giuseppe Calasso***
Dipl. Phys. ETH
born October 11, 1966
citizen of Italy and Switzerland

accepted on the recommendation of *Prof. Dr. M.W. Sigrist, ETH Zürich, referee*
Prof. Dr. H. Melchior, ETH Zürich, co-referee
Dr. W. Faubel, Forschungszentrum Karlsruhe, Germany, co-referee

Zürich, December 1998

To my daughter

Lara Francesca

Table of Contents

Summary

In this study we have focused on photoacoustic and photothermal investigations of gases and multicomponent gas mixtures by using a home-built continuously tunable high pressure CO_2 laser. A theoretical model for the description of the temporal evolution of the gas density after laser pulse excitation is presented. We extended a previous model developed for thermal lensing signals by including a third molecular species in order to distinguish between all molecular states involved in a deexcitation process. Besides the excited absorbing molecules and buffer gas molecules we considered also non-excited absorbing molecules. With this improvement we achieve an excellent agreement with experimental results obtained with the photothermal beam deflection technique even in cases where previous models failed. This new model has been applied for the investigation of microphone characteristics suitable to increase the signal-to-noise ratio (SNR) in pulsed photoacoustics (PA) and for the analysis of photothermal beam deflection (PTBD) signals for the derivation of molecular relaxation times and thermal conductivities of gases.

All our measurements have been performed using a previously built continuously tunable high pressure CO_2 laser. In order to achieve better pulse-to-pulse stability and higher repetition rate, the laser design has been improved. Important modifications were the change of the electronic control responsible for the charging process of the laser capacitors and the trigger electronics of the discharge with a new self-made development. The occurrence of arcing between the brass electrodes was successfully reduced by insulating the borders of the electrodes. These measures enabled us to increase the original maximal pulse repetition rate from 0.2 Hz to 1 Hz. This represents the maximum allowed repetition rate with the current laser gas flow configuration. Continuous tunability over 76 cm^{-1} within the four laser branches between 932 cm^{-1} and 1088 cm^{-1} with a bandwidth of 0.017 cm^{-1}, a pulse duration of 140 ns and a repetition rate from 0.1 to 1 Hz are the main features of this laser that render it to a powerful radiation source for spectroscopic investigations.

In view of optimizing the performance for pulsed PA detection with microphones in a non-resonant cell, we have investigated the dependence of the SNR on the microphone responsivity and bandwidth for the first time both theoretically and experimentally. We demonstrate that the measured SNR can be represented by an analytical function derived from the microphone specifications. This relation allows to select the most appropriate microphone for maximum detection sensitivity.

The high detection selectivity achieved with our tunable laser source and PA detection scheme is demonstrated with the analysis of a mixture of six CO_2 isotopes ($^{12}C^{16}O_2$, $^{12}C^{18}O_2$, $^{13}C^{16}O_2$, $^{13}C^{18}O_2$, $^{16}O^{12}C^{18}O$, $^{16}O^{13}C^{18}O$). Based on the known absorption cross sections of $^{13}C^{16}O_2$, $^{12}C^{16}O_2$, and $^{16}O^{12}C^{18}O$, the specified $\Sigma^{12}C/\Sigma^{13}C$ and $\Sigma^{16}O/\Sigma^{18}O$ ratios in the isotopic mixture and our PA measurements, the concentrations of all six isotopes in the mixture were determined. Theoretically predicted absorption lines of the various isotopes were confirmed. Furthermore, unknown absorption cross sections of the $^{12}C^{18}O_2$, $^{13}C^{18}O_2$ and $^{16}O^{13}C^{18}O$ isotopes in the 9-11 μm were derived for some of the prominent absorption lines.

Finally, the theoretical predictions of the temporal evolution of the gas density following laser pulse excitation have been examined with a PTBD setup involving a HeNe laser probe beam and a position sensor or knife edge / photodiode combination. This scheme senses the density variation after laser pulse excitation optically allowing non contact measurements both inside and outside the gas region excited with the pump beam. PTBD experiments have been performed on SF_6, C_2H_4, C_2H_3Cl and C_2H_3Br buffered in N_2, rare gases and various rare gas mixtures. The temporal PTBD signal shapes were found to be in excellent agreement with those theoretically predicted. From the signal shapes vibrational-translational (V-T) deactivation rates and/or relaxation times as well as thermal conductivity data can be derived directly. A criterion has been developed for optimum experimental conditions, particularly pump beam radius and distance between pump and probe beam, under which the relaxation rates are obtained with a given accuracy. The deduced parameters agree well with available data and many new results are obtained. This concerns in particular rates of the asymmetric molecules C_2H_3Cl and C_2H_3Br or of C_2H_4 molecules diluted in rare gas mixtures.

Riassunto

Questo studio è finalizzato all'indagine di metodi fotoacustici e fototermici per l'analisi di singoli gas e di miscele gassose a più componenti che utilizzano come sorgente un laser costruito in sede a CO_2 ad alta pressione accordabile in frequenza in maniera continua. Viene discusso un modello teorico che descrive lo sviluppo temporale della densità del gas dopo l'eccitazione con un impulso laser. A questo scopo, un modello precedentemente sviluppato per la descrizione dei segnali generati dalla lente termica é stato esteso includendo una terza specie molecolare, in modo da separare i contributi dei diversi stati molecolari coinvolti nel processo di diseccitazione. Oltre alle molecole assorbenti eccitate e a quelle del gas solvente, abbiamo considerato nel nuovo modello anche le molecole assorbenti non-eccitate. I risultati sono in eccellente accordo con le misure ottenute tramite la tecnica della deviazione fototermica del fascio, anche nei casi in cui i modelli precedenti risultavano inadeguati. In questo lavoro il nuovo modello è stato adottato sia negli studi fotoacustici (PA) impulsati, per studiare le caratteristiche del microfono al fine di migliorare il rapporto segnale rumore (SNR), sia per l'analisi dei segnali ottenuti con la tecnica fototermica della deviazione di fascio (PTBD) per la misura dei tempi di rilassamento molecolare e della conducibilità termica dei gas.

Tutte le nostre misure sono state realizzate utilizzando un laser a CO_2 ad alta pressione accordabile in frequenza in maniera continua, modificato al fine di aumentare la stabilità degli impulsi del laser e ottenere una ripetizione più elevata degli stessi. Gli interventi più importanti hanno riguardato la progettazione di nuovi schemi per l'elettronica responsabile del processo di carica dei condensatori del laser e per l'elettronica di innesco della scarica elettrica tra gli elettrodi del laser. Le scariche ad arco fra gli elettrodi d'ottone presenti originariamente sono state ridotte con successo isolando i bordi degli elettrodi. Tali interventi ci hanno permesso di aumentare la frequenza massima di ripetizione dell'impulso originale da 0,2 Hz ad 1 Hz raggiungendo il limite massimo ottenibile con la configurazione usata del flusso del gas laser. L'accordabilità continua in lunghezza d'onda in un intervallo di 76 cm^{-1} all'interno dei quattro rami di emissione del laser a CO_2 fra 932 cm^{-1} e 1088 cm^{-1}, la larghezza di banda di 0,017 cm^{-1}, la durata dell'impulso di 140 ns e la sua frequenza di ripetizione compresa tra 0,1 ed 1 Hertz sono le principali caratteristiche che rendono questo laser una importante sorgente di radiazione per uso spettroscopico.

Per ottimizzare, agendo sulle caratteristiche del microfono, le prestazioni di rilevazione dei sistemi PA che utilizzano celle non-risonanti, abbiamo studiato per la prima volta sia teoricamente che sperimentalmente la dipendenza del rapporto segnale-rumore (SNR) da

alcuni dati tecnici dei microfoni come la risposta e larghezza di banda. Abbiamo dimostriamo che il SNR misurato può essere rappresentato da una funzione analitica considerando le specifiche del microfono. Ciò consente di selezionare il microfono in maniera da ottimizzare la sensibilità di rilevazione.

L'alta selettività, realizzata accoppiando il nostro laser accordabile in frequenza in maniera continua ad uno schema di rilevazione PA, viene dimostrata con l'analisi d'una miscela composta da 6 isotopi del CO_2 ($^{12}C^{16}O_2$, $^{12}C^{18}O_2$, $^{13}C^{16}O_2$, $^{13}C^{18}O_2$, $^{16}O^{12}C^{18}O$, $^{16}O^{13}C^{18}O$). Note le sezioni d'urto di assorbimento di $^{13}C^{16}O_2$, $^{12}C^{16}O_2$, e di $^{16}O^{12}C^{18}O$, ed essendo specificati i rapporti $\Sigma^{12}C/\Sigma^{13}C$ e $\Sigma^{16}O/\Sigma^{18}O$ nella miscela isotopica, le misure PA hanno permesso di ricavare le concentrazioni dei 6 isotopi presenti nella miscela e di confermare le corrispondenti righe di assorbimento previste teoricamente. In oltre, per alcune delle righe di assorbimento più forti, sono state misurate le sezioni d'urto di assorbimento nell'intervallo 9-11 μm degli isotopi $^{12}C^{18}O_2$, $^{13}C^{18}O_2$ e $^{16}O^{13}C^{18}O$ finora sconosciute.

Infine sono state esaminate le previsioni teoriche dello sviluppo temporale della densità del gas che segue l'eccitazione di un impulso laser con la tecnica PTBD, utilizzando un laser ad He-Ne di sonda in combinazione con un sensore di posizione, oppure uno schema "knife edge"/fotodiodo. Questa tecnica permette di compiere misure sia all'interno che all'esterno della regione del gas eccitata dal fascio di pompaggio. Vari esperimenti sono stati effettuati con i gas SF_6, CH_4, C_2H_3Cl e C_2H_3Br diluiti in N_2, in gas rari e in varie miscele di gas rari. L'andamento temporale del segnale PTBD misurato è in ottimo accordo con quello previsto teoricamente. Dalla forma del segnale sono stati derivati direttamente la velocità di diseccitazione dei modi vibrazionali - traslazionali (V-T) e/o i tempi di rilassamento ed il valore della conducibilità termica. Si è inoltre sviluppato un criterio per ottimizzare l'assetto sperimentale, in particolare il raggio del fascio laser di pompaggio e la distanza tra fascio e sonda, al fine di ottenere il valore del tempo di rilassamento molecolare con una voluta precisione. I parametri ottenuti sono in buon accordo con i dati disponibili. In più sono stati ottenuti molti nuovi risultati. Tra questi contano le velocità di rilassamento di molecole asimmetriche come C_2H_3Cl e C_2H_3Br, e di molecole eccitate diluite in miscele di gas rari.

Chapter 1

Introduction

The investigation of trace gas species is of great current interest in atmospheric research with respect to both the determination of their concentrations and to the study of their chemical reactivity. The detection of the great number of gaseous air pollutants requires schemes capable of high sensitivity and selectivity. Some of the most promising approaches are based on optical spectroscopic techniques such as UV and IR spectroscopy, Lidar and photoacoustic techniques (Sigrist [1994]). Spectroscopic methods allow the distinction of different molecular species by their characteristic absorption spectrum like a molecular fingerprint. In particular, laser spectroscopy has been put forward recently, fostered by the rapid progress of new tunable radiation sources that yield feasible detection schemes with excellent sensitivity and selectivity for a large group of both organic and inorganic compounds. Particularly suitable kinds of spectroscopy in this context are photoacoustic (PA) and photothermal (PT) detection schemes owing to their exceptional insensibility to scattering processes. Both PA and PT spectroscopy have been applied to trace gas monitoring by various research groups including our own laboratory.

An favorable radiation source for spectroscopic investigations is the CO_2 laser with its emission in the 9-11 μm region of the infrared spectrum where many molecules exhibit their characteristic fingerprints. However, conventional CO_2 lasers like low pressure or waveguide CO_2 lasers provide only line tunability or at most limited tunability around each CO_2 transition. This lack of tunability reduces the detection selectivity required for multicomponent samples. In this respect, our home made high-pressure continuously tunable CO_2 laser with a total tuning range of 76 cm^{-1} and a linewidth of only 0.017 cm^{-1} (Repond and Sigrist [1996/a]) as described in chapter 3, represents a valuable tool. Furthermore, the detection of the absorbed laser pulse energy in a gas by the PA or the PT effect offers some unique features. Laser irradiation of a gas sample generates a nonequilibrium population distribution in rovibrational states. As a consequence of non-radiative relaxation processes a temperature variation in the gas occurs which induces an acoustic pulse (photoacoustic effect) and a density variation (photothermal effect). The resulting pressure pulse, proportional to the absorbed energy, is recorded with a microphone in PA spectroscopy. Unlike conventional transmission spectroscopy where a minute decrease of the power transmitted through an air sample needs to be detected, the

PA detection scheme thus allows the direct measurement of the small amount of laser radiation that is absorbed by the molecules. This results in an inherently high sensitivity. This feature combined with the narrowband tunable laser source reveals a great potential for trace gas monitoring. This was already demonstrated in previous studies on trace gases (Repond [1995], Repond and Sigrist [1996/b]) and again with the present quantitative analysis of a mixture of six CO_2 isotopes as presented in chapter 4. Emphasis is also placed on the optimization of the PA detection performance in the non-resonant pulsed regime by selecting the microphones with appropriate bandwidth and responsivity.

The knowledge of the rates of the different possible processes by which transitions between molecular energy states take place is important in many fields. As an example, it is known that molecules excited to highly energetic states may react more rapidly than molecules in the ground state and products may be formed in highly energetic states (Cottrell [1965]). The absorptivity and emissivity of a system of radiation will certainly depend on the relative rates of non-radiative and radiative energy transfer processes. The laser process is a typical example in which the rates of energy transfer within the active medium play a key role. Various methods have been developed to determine energy transition rates such as vibrational-vibrational (V-V), vibrational-rotational (V-R), and vibrational-translational (V-T) rates. Pioneering schemes involve acoustic methods such as the shock-tube or those based on the dispersion effect that occurs when the period of the compression-rarefaction cycle of a sound frequency becomes comparable with the relaxation time. A review of acoustic methods was given by Lamber (Lamber [1977]). With the progress made in laser technology, a variety of optically-based methods with the advantage of exciting molecules to specific vibrational states and studying their relaxation rates have found important applications. Frequently used techniques specially suited to study vibrational-vibrational energy transfers are the laser-induced fluorescence and the laser double resonance (Weitz and Flynn [1974], Yuan et al. [1973/a-b], Flynn [1973], Häger et al. [1979]). On the other hand, photothermal techniques like thermal lensing or photothermal beam deflection are preferable to investigate rovibrational-translational (V-T) energy transfers.

For the first time, we apply a continuously tunable CO_2 laser to photothermal beam deflection (PTBD) studies on gaseous media. The theoretical treatment of the gas dynamics following laser excitation is outlined in chapter 2. Thanks to a new approach that distinguishes between the excited and non-excited absorbing molecules under study and the buffer gas molecules, we obtain a mathematical description of the time-resolved density variation after laser excitation. The derived temporal signal shapes are verified by our PTBD measurements on various gas mixtures. This enabled us to determine V-T relaxation rates of excited molecules (SF_6, C_2H_4, C_2H_3Cl, C_2H_3Br) in buffer gases

(N_2, He, Ar, Kr) and gas mixtures. New and previously unavailable relaxation rates are reported in chapter 5. As a unique feature thermal conductivity data can be deduced simultaneously by this method.

Chapter 2

Theoretical Background

Absorption of infrared light in gases promotes the excitation of vibrational/rotational molecular states. The transformation of the absorbed energy into translational energy consists of several processes. In this chapter we firstly describe the differences of such processes giving an overview of their time-scale (Table 2.1). In view of the investigation of these processes with the photothermal beam deflection (PTBD) technique we present a theoretical treatment of gas dynamics after laser pulse excitation. Thanks to our new proposed approach that distinguishes between non-excited and excited absorbing gas molecules and buffer gas molecules, we obtain a generally valid mathematical model for gas density variations after laser pulse excitation. The analysis of experimental data by this model is not restricted to PTBD measurements (chapter 5) but can also be applied to thermal lens (TL) and to photoacoustic (PA) measurements (chapter 4).

2.1 Absorption and Relaxation

The energy of photons in the infrared region (2 μm < wavelength λ < 50 μm), corresponds to the energy of most molecular vibrational states. Optical absorption promotes an absorbing gas species to an excited state. The light absorption increases the internal energy of the absorber by an amount equal to the photon energy absorbed. As a result, the population density of the molecular energy states, which in equilibrium are given by a Boltzmann distribution, are changed. In most cases, the relaxation occurs almost exclusively via collisional processes. The radiative relaxation is negligible in the spectral region considered due to the λ^3-dependence of the lifetime for spontaneous emission which is many orders longer than the collisional relaxation lifetime. The process of transferring the absorbed energy into translational energy is not instantaneous and may consist of several contributions (rates). It is necessary to distinguish between the lifetime of a particular excited level and the relaxation time for the analysis of such processes. The level lifetime is the average residence time for a molecule in a particular vibrational or rotational level before making a transition to another level. Individual level lifetimes are generally shorter than relaxation times because they involve transitions to all levels, not just to those resulting in an increased translational energy.

Individual level lifetimes apparently depend on the same parameters as the relaxation rates do. Rates of rotational and vibrational equilibration and relaxation depend on the collisional rate, on the temperature, and on the kind of the collisional partner. In the gas phase, rovibrational relaxation rates follow an empirical behaviour called energy gap law that was found with rare-gas collision partners (Flygare [1968]) and later confirmed using an entropy-based approach (Steinfeld et al. [1989]). This law says that for a collection of excited states of a gas molecule buffered in a solvent that is in equilibrium at a temperature T, the relaxation to an equilibrium state can be generally described through

$$\frac{1}{\tau_{relax}} = \eta \cdot e^{-\Delta E/kT} \quad , \tag{1}$$

where τ_{relax} [s] is the relaxation time, η [s^{-1}] is the frequency of occurrence of conditions resulting in energy transfer (e.g. by collisions), ΔE is the energy gap between excited and equilibrium state, k is the Boltzman constant and T denotes the temperature. The relaxation times τ_{relax} thus strongly depend on ΔE and on the interaction term η which itself depends on the nature of the particular interaction. As a consequence, translational (T-T) energy relaxation is very efficient since the translational energy gap is essentially zero and species with higher transitional energy collide at higher rates. Rotational to rotational (R-R) relaxation is also a highly efficient processes due to the small energy-level spacing. Flygare (Flygare [1978]) pointed out that molecules with large dipole-dipole interaction can actually have a faster R-R relaxation than T-T relaxation, since T-T relaxation is a purely collisional process and requires physical contact. Rotational to translational (R-T) relaxation is a collision-induced process and is about a factor 100 slower than R-R relaxation, and about a factor 10 slower than T-T relaxation. The reason is that not all collisions have the correct geometry for coupling angular momentum to translational momentum. Excited vibrational levels transfer the energy primarily via collisions, although longer-range dipole interaction can also occur. The types of vibrational relaxation are V-V, V-R, and V-T.

V-V relaxation is well distinguished from V-R and V-T in both the time scale for relaxation and the way excess energy is distributed among the degrees of freedom. V-V energy exchange can lead to vibrational-level equilibration that is independent of the rotational and translational temperature. V-V processes can distribute the energy among the vibrational levels according to the Boltzmann distribution law. As a general rule, V-R/T relaxation processes take considerably longer than V-V processes. Table 2.1 gives an estimation of relaxation times of typical gas-phase species at standard temperature and pressure (Flygare [1968]).

Table 2.1. *Estimated relaxation times for small molecules in the gas phase at 300K, 1 atm pressure from Flygare (Flygare [1968]). T denotes translation, R rotation, and V vibration.*

Process	Relaxation time [s]
T-T	10^{-9}
R-T	10^{-8}
R-R	10^{-10}
V-R	10^{-5}
V-V	10^{-8}
V-T	10^{-5}

Based on the energy gap argument, it is possible to predict the V-V versus V-R/T rates of particular species. However, the energy gap argument alone does not account for vibrational relaxation trends and breaks down when comparing one molecule to another. The significance of the factor η can vary strongly from molecule to molecule.

Theories are available to calculate efficiencies for V-R and V-T energy transfer. One of the most tested theories is the Schwartz, Slawsky and Herzfeld "SSH" (Schwartz et al. [1952]) and the Schwartz and Herzfeld (Schwartz and Herzfeld [1954]) theory. Unfortunately, most theories use parameters that are difficult to obtain from independent experiments and tend to yield erroneous predictions.

2.2 Energy Transfers after Laser Pulse Excitation

Laser pulses with duration τ_L in the ns range or shorter (in this work $\tau_L \approx 10^{-7}$ [s]), generate a nonequilibrium population distribution in rovibrational states. With the excitation, R-R, R-T, and T-T relaxation processes start immediately. The R-R relaxation produces a canonical redistribution of the rovibrational states. In the ground state, rotational hole filling takes place. The combined ground and excited-state relaxation can either release energy to the matrix or require energy from the matrix. The latter process

corresponds to actual cooling. Cooling after absorption of 9 to 10 μm radiation in a CO_2-N_2 system was predicted more then 20 years ago (Wood et al. [1971]) and was demonstrated afterwards in numerous experiments (Meyer and Sigrist [1990], Cannemeyer and Vries [1974], Gebhardt and Smith [1972], Bailey et al. [1985]). Cooling is not unique to CO_2-N_2 and has been observed for the ν_3 excitation of CH_3F buffered in Ar (Grabiner et al. [1972]) as well. Following the more rapid R-R/T and T-T steps, V-V relaxation takes place. V-V relaxation produces a quasi-equilibrium among the excited vibrational levels. Finally, these excited vibrational states return to the ground state in a time given by the fastest V-R/T rate. During the slow V-R/T step, faster V-V steps maintain the excited state populations in a canonical distribution. It is therefore impossible to distinguish between the V-R/T steps from the individual levels. The excited vibrational levels decay with a rate constant given by a combination of the individual rate. As a consequence of the relaxation process a temperature variation in the gas occurs which induces photoacoustic (PA) and photothermal (PT) effects. The study of such effects, as e.g. in this work with the photothermal beam deflection (PTBD) technique or the thermal lensing (TL) technique, represents an indirect method to resolve the molecular dynamics. However, it should be pointed out that PT methods do not sense individual energy transfer but only the overall energy contribution of all relaxation processes. Although in some cases V-V and V-T/R processes could be important in a relaxation mechanism they remain indistinguishable. In such cases the infrared laser double resonance technique is more appropriate (Yuan et al. [1973/b]). Here an intense radiation field, such as a pulsed pump laser, is used to excite molecules, while a second weak radiation source (such a continuous probe laser) tuned to another wavelength of the absorption spectrum of the gas monitors the population changes induced by the absorption.

In this study we apply the PTBD technique to resolve molecular dynamics, therefore we focus now on a detailed investigation of gas dynamics after laser pulse excitation.

2.3 Gas Dynamics

The main dynamic molecular mechanisms which take place in an absorbing gas diluted in a nonabsorbing buffer gas after being irradiated by a short pump laser pulse are: **(i)** energy deposition through relaxation, **(ii)** generation of acoustic waves by such a heat deposition, **(iii)** binary diffusion of the excited molecules through the bath gas and **(iv)** further dissipation of the gas perturbation through thermal conductivity (Barker et al. [1982, 1988], Toselli et al. [1990]). Analyses of energy-transfer and gas-dynamic

processes in gases due to the absorption of a short laser pulse have been performed by several authors (Barker et al. [1982, 1988], Toselli et al. [1990], Grabiner et al. [1972], Siebert et al. [1974], Bailey et al. [1978, 1980, 1983, 1985], Diebold [1989], Jacobs [1989]). In most treatments the modelling is simplified according to the importance of the different mechanisms at different time scales (Grabiner et al. [1972], Siebert et al. [1974], Bailey et al. [1978, 1980, 1983, 1985], Diebold [1989]). Since these time regimes are not always well defined the analysis in the present work is based on the comprehensive treatment performed by Barker and co-workers (Barker et al. [1982, 1988]) which takes into account all of the above mentioned molecular mechanisms and which therefore constitutes a unified time scale approach.

In order to determine mathematically the time-dependent thermal lensing signal obtained under irradiation of a gas probe enclosed in a cylindrical cell of radius b by a short pump laser pulse of photon energy $h\nu$, Barker and Rothem (Barker and Rothem [1982]) have used the fact that this signal can be written in terms of the gas density variation $\rho(r,t)$ that depends on the position (r in cylindrical coordinates) and time (t). To obtain $\rho(r,t)$ the governing dynamic equations for mass, momentum and energy of the system are employed (Hirschfelder et al. [1964]), in conjunction with the expression for the temporal and spatial profile of the number density $N_1(r,t)$ of the excited molecules. Barker and collaborators treat the energy transfer process between the excited molecules A^* which have absorbed the laser photon energy $h\nu$ and the unexcited molecules A of the absorbing gas that are diluted in the buffer gas of molecules M as a chemical reaction

$$A^* + M \rightarrow A + M \quad . \tag{2}$$

This reaction is further assumed to be characterised by the relaxation time τ_{relax} or first-order rate coefficient $k_e = 1/\tau_{relax}$ (Barker and Rothem [1982]). The authors then use the energy balance equation given by Hirschfelder and co-workers (Hirschfelder et al. [1964]) for reacting gases. Under simplifications valid for very low concentrations of the absorbing molecules and absence of viscosity and external forces, a third-order partial differential equation in $\rho(r,t)$ is obtained (see Eq. (5) below). In order to solve this equation the number density profile of the excited molecules and hence of the gas density variation is expressed as a series of zeroth-order Bessel functions $J_0(\nu_j r)$

$$\rho(r,t) = \sum_{j=1}^{\infty} c_j(t)\, J_0\left(\nu_j r\right) \quad . \tag{3}$$

Here, v_j denotes the ratio X_j / b where the X_j is the j-th zero of $J_0(X)$ and b is the cell radius. The solution of the resulting ordinary differential equation for the corresponding expansion coefficients $c_j(t)$ is obtained through the Laplace transformation method. The coefficients derived are then substituted into the series expression for the density variation (Eq. (3)), enabling a numerical evaluation of ρ for a finite number of terms.

The use of such an approach has already been fruitfully applied to the analysis of time-dependent thermal lensing signals (Toselli et al. [1990]), and has been successfully extended to the mathematical description of photothermal beam deflection (PTBD) signals (Calasso et al. [1996]). It is, however, useful to stress the existence of a problem within the resulting expansion coefficients $c_j(t)$ given by Barker for future applications. The coefficients $c_j(t)$ are expressed as directly proportional to a "general factor" (Barker and Toselli [1988]) as

$$c_j(t) \propto \left(U v_j^2 - k_e Q\right) \quad . \tag{4}$$

Here U and Q are coefficients of the third order partial differential equation for $\rho(r,t)$ mentioned above

$$B\frac{\partial^3 \rho}{\partial t^3} - E\frac{\partial^2 \vec{\nabla}^2 \rho}{\partial t^2} + (W-F)\vec{\nabla}^2\frac{\partial \rho}{\partial t} - C\vec{\nabla}^2\vec{\nabla}^2\rho - U\vec{\nabla}^2\vec{\nabla}^2 N_1 + k_e Q\vec{\nabla}^2 N_1 = 0 \quad . \tag{5}$$

The expressions for the factors B, E, W, F, C, U and Q in terms of physical parameters are summarised in Table I of Ref. (Barker and Toselli [1988]). We just recall here the key parameters U and Q given as

$$U = D_{12} kT(1 - m_1 / m_2) \tag{6a}$$

$$Q = u_{\text{int}} + \frac{3}{2} kT(1 - m_1 / m_2) \quad . \tag{6b}$$

In these equations m_1, m_2 are the molecular masses of absorber gas (A) and buffer gas (M), D_{12} is the binary molecular diffusion coefficient and $u_{\text{int}} = h\nu$ is the excitation energy per molecule. The problem with the expansion coefficients $c_j(t)$ evidences at thermal energies kT that are comparable to or larger than the excitation energy $h\nu$. In such cases, and according to Eqs. (3), (6a) and (6b), a change in the mass relationship m_1 / m_2 may result in a change of sign of $c_j(t) \propto \left(U v_j^2 - k_e Q\right)$ for all j and hence of the

density variation $\rho(r,t)$. Besides, a change of the density in absence of any excitation energy $h\nu$ is implied. These implications are physically not sound and indicate the presence of an inconsistency in the treatment.

The origin of the problem may be found by comparing the hydrodynamic energy balance equations under neglectance of external forces and viscosity (as in Barker and co-workers' treatment) for non-reacting (Eq. (7a)) and reacting (Eq. (7b)) gases (Hirschfelder et al. [1964])

$$\rho c_V \frac{\partial T}{\partial t} = -\vec{\nabla}\cdot\vec{q} - \vec{p} * \vec{\nabla}\vec{v} + \sum_i u_i^0 \ \vec{\nabla}\cdot\vec{j}_i \tag{7a}$$

$$\rho c_V \frac{\partial T}{\partial t} = -\vec{\nabla}\cdot\vec{q} - \vec{p} * \vec{\nabla}\vec{v} + \sum_i u_i \ (\vec{\nabla}\cdot\vec{j}_i - m_i K_i) \quad . \tag{7b}$$

In these equations, $\vec{p}$ denotes the pressure tensor, c_V the average specific heat capacity at constant volume with respect to the average molecular mass, $\vec{q}$ the total energy flux due to the temperature gradient and the molecular diffusion and $\vec{v}$ the respective bulk average flow velocity. The parameter K_i is given as

$$K_i = \partial N_i / \partial t + \vec{\nabla}\cdot\vec{j}_i / m_i \tag{8}$$

which represents the total increase of the number of molecules of species i per unit volume and unit time due to chemical reactions, $\vec{j}_i$ denotes the corresponding diffusive mass fluxes whereas u_i^0 and $u_i = u_i^0 + \delta_{1,i}\, h\nu / m_i$ (with $\delta_{j,i}$ denoting the Kronecker delta symbol) are the internal and total energy per gram of each of the molecular species, respectively. Obviously, the difference between the equations for reacting and non-reacting gases is encountered in the last terms of Eqs. (7 a & b), which we separately write as

$$L_{non-reacting} = \sum_i u_i^0 \ \vec{\nabla}\cdot\vec{j}_i \quad , \tag{9a}$$

and

$$L_{reacting} = \sum_i u_i \ (\vec{\nabla}\cdot\vec{j}_i - m_i K_i) \quad . \tag{9b}$$

Under the assumption that only species A^* ($i=1$) and M ($i=2$) exist, i.e. a two-species treatment as actually considered in Ref. (Barker and Rothem [1982]), the following

expression was derived for $L_{reacting}$ for the energy-transfer process considered in our case

$$L_{reacting}^{\text{Barker}} = \sum_i u_i^0 (\vec{\nabla} \cdot \vec{j}_i - m_i K_i) + \frac{h\nu}{m_1} (\vec{\nabla} \cdot \vec{j}_1 - m_1 K_1) \quad . \tag{10}$$

One striking problem of this simplified two-species approach is evidenced by the fact that the original expression for $L_{non-reacting}$ is not recovered when $h\nu$ is set equal to zero in Eq. (10), i.e. when the gas is not irradiated at all. This problem is solved by our novel treatment which considers a third species, namely non-excited molecules of the absorbing gas species A ($i = 3$) (Calasso et al. [1998]). With such a three-species approach of the type of chemical reaction

$$A^* + A + M \rightarrow A + A + M \quad , \tag{11}$$

it is possible to express $L_{reacting}$ as

$$L_{reacting}^{(A,A^*,M)} = (u_1^0 - u_2^0)[\vec{\nabla} \cdot \vec{j}_1 + \vec{\nabla} \cdot \vec{j}_3] + \frac{h\nu}{m_1} (\vec{\nabla} \cdot \vec{j}_1 - m_1 K_1) \quad , \tag{12}$$

since $K_3 = -K_1$. Because of the total mass flux conservation $\sum_i \vec{j}_i = 0$, and since $u_1^0 = u_3^0$ for $h\nu = 0$, we do recover $L_{non-reacting}$ in absence of radiation.
In view of these arguments, it is clear that the three-species formulation, which explicitly considers that not all of the absorbing molecules are excited, represents a more correct treatment than the two-species one. The time-dependent expansion coefficients $c_j(t)$ have now to be derived within this new formalism.

In the following, we summarize the derivation by Barker and co-workers using their formalism and introduce the new tree species treatment. Consider a small concentration $N_1(r,t)$ of laser-excited molecules in a bath of total gas concentration N. N_1 decays only due to mass diffusion and collisional deactivation with the effective first-order rate coefficient k_e given by

$$\frac{\partial N_1}{\partial t} = -k_e N_1 \quad . \tag{13}$$

The governing rate equation may be written in cylindrical coordinates as

$$\frac{dN_1}{dt} = D_{12}\frac{1}{r}\frac{\partial}{\partial r}\left(r\frac{\partial N_1}{\partial r}\right) - k_e N_1 \quad , \tag{14}$$

where D_{12} is the binary diffusion coefficient for the excited molecules diffusing among the unexcited molecules.

The initial spatial profile of the excited molecules is controlled by the shape of the exciting laser beam assumed Gaussian and characterised by the radius r_b.

The boundary conditions of equation (14) are

$$N_1(r,t=0) = N_{01}e^{-\left(r/r_b\right)^2} \tag{15a}$$

$$N_1(r,t\to\infty) = 0 \tag{15b}$$

$$N_1(r\to\infty,t) = 0 \quad . \tag{15c}$$

Using the method of variable separation, the general solution of Eq. (14) becomes

$$N_1(r,t) = \sum_i G_i e^{\alpha_i t} J_0(\nu_i r) \quad , \tag{16}$$

where $\alpha_i = -\left(D_{12}\nu_i^2 + k_e\right)$ and $\nu_i = X_i/b$ with X_i denoting the zeroes of the zeroth order Bessel $J_0(X)$ function and b the cell radius. The coefficients G_i are determined by the initial conditions. For a exciting Gaussian laser beam with radius r_b much smaller than the cell radius, G_i can be written as

$$g_i = G_i = \frac{N_{01}r_b}{b^2\left[J_1(X_i)\right]^2}e^{-\left(\frac{\nu_i^2 r_b^2}{4}\right)} \quad , \tag{17}$$

where $J_1(X)$ is the first order Bessel function. The coefficient g_i is defined as in Barker and Rothem (Barker and Rothem [1982]) within the coefficient G_i for a Gaussian laser profile.

The expression $N_1(r,t)$ may now be used in conjunction with the dynamic equations for mass, momentum and energy to obtain an expression for the density variation $\rho(r,t)$. Considering that the density variation produced is small compared to the total system density, the governing equations are linearized, and higher order terms involved in $\rho(r,t)$ are neglected. The hydrodynamic equations for the system become

$$\frac{\partial \rho}{\partial t} = -\rho \vec{\nabla} \cdot \vec{v} \tag{18a}$$

$$\frac{\partial \vec{v}}{\partial t} = -\frac{1}{\rho} \vec{\nabla} p \quad , \tag{18b}$$

and

$$\rho_0 c_v \frac{\partial T}{\partial t} = -\vec{\nabla} \cdot \vec{q} - \vec{p} * \vec{\nabla} \vec{v} + \sum_i u_i \left(\vec{\nabla} \cdot \vec{j}_i - m_i K_i \right) \quad . \tag{18c}$$

The linearized continuity equation (18a) and the momentum equation (18b) are the same as those given by Barker and Rothem (Barker and Rothem [1982]). Equation (18c) represents the energy balance equation written in the Hirschfelder formalism as mentioned before (7b). This equation allows the calculation with the new three species model. The index $i = 1, 2, 3$ in this equation represents the three species A^*, M, and A respectively. Like in Barker and Rothem's (Barker and Rothem [1982]) derivation, external (body) forces and viscosity are neglected. From the momentum equation (18a), the term in Eq. (18c) involving tensor multiplication may be written as

$$\vec{p} * \vec{\nabla} \vec{v} = -\frac{p}{\rho} \frac{\partial \rho}{\partial t} \quad . \tag{19}$$

The remaining left part of equation (18c) can be written with the total energy flux $\vec{q}$ considered in Ref. (Hirschfelder et al. [1964]) as

$$-\vec{\nabla} \cdot \vec{q} + \sum_i u_i \left(\vec{\nabla} \cdot \vec{j}_i - m_i K_i \right) = \lambda \vec{\nabla}^2 T + \sum_i \left[(u_i - h_i) \vec{\nabla} \cdot \vec{j}_i - u_i m_i K_i \right] \tag{20}$$

where λ is the thermal conductivity and

$$h_i = u_i + \frac{5}{2} \frac{kT}{m_i} \tag{21}$$

represents the enthalpy per gram of molecules of type i.

Taking into account that the species of type $i = 1$ represents the excited one, the energies u_i are given by

$$u_1 = \frac{3}{2}\frac{kT}{m_1} + \frac{h\nu}{m_1} \quad , \quad u_2 = \frac{3}{2}\frac{kT}{m_2} \quad , \quad u_3 = \frac{3}{2}\frac{kT}{m_1} \quad , \tag{22}$$

where $h\nu$ is the absorbed photon energy.
With equations (21) (22) and (8), and taking into account that the excited molecules relax with the first-order rate coefficient k_e as previously described in Eq. (13), equation (20) is written as

$$-\vec{\nabla}\cdot\vec{q} + \sum_i \hat{u}_i\left(\vec{\nabla}\cdot\vec{j}_i - m_i K_i\right) = \lambda\vec{\nabla}^2 T - \frac{h\nu}{m_1}\vec{\nabla}\cdot\vec{j}_1 + h\nu k_e N_1 - 4kT\sum_i \frac{\vec{\nabla}\cdot\vec{j}_i}{m_i} \quad . \tag{23}$$

Using the total mass flux conservation equation

$$\sum_i \vec{j}_i = 0 \quad , \tag{24}$$

and considering the definition of $\vec{j}_i$ given in Ref. (Hirschfelder et al. [1964]), the following binary molecular diffusion coefficient equalities hold

$$D_{11} = D_{22} = D_{33} = 0 \tag{25a}$$

$$D_{ik} = D_{ki} \qquad \text{for } i, k = 1, 2, 3 \tag{25b}$$

$$D_{12} = D_{32} \tag{25c}$$

$$D_{13} = D_{12}\frac{m_2}{m_1} \quad . \tag{25d}$$

These equations are used for the evaluation of the coefficients $\vec{j}_i$ that appear in Eq. (23). In addition, it is considered that the weighted molecular mass of the system of total $N = \sum_i N_i$ molecules per unit volume can be written as

$$m = \beta m_1 + (1-\beta)m_2 \tag{26}$$

in terms of the constant concentration ratio of absorbing molecules $\beta = (N_1 + N_3)/N$. On the other hand, the relationships for the distributions of N, N_1, N_2 and N_3 in terms of m, β and ρ can be expressed as

$$\vec{\nabla}N = \frac{1}{m}\vec{\nabla}\rho \tag{27a}$$

$$\vec{\nabla}N_3 = \frac{\beta}{m}\vec{\nabla}\rho - \vec{\nabla}N_1 \tag{27b}$$

$$\vec{\nabla}N_2 = \frac{1-\beta}{m}\vec{\nabla}\rho \quad . \tag{27c}$$

Substituting of all these equations in (23) yield

$$-\vec{\nabla}\cdot\vec{q} + \sum_i \hat{u}_i\left(\vec{\nabla}\cdot\vec{j}_i - m_i K_i\right) = \lambda\vec{\nabla}^2 T + h\nu k_e N_1 + \frac{D_{12}h\nu m_2 n}{\rho}\vec{\nabla}^2 N_1 \quad . \tag{28}$$

The energy balance equation is rewritten using (19) and (28) as

$$\rho_0 C_v \frac{\partial T}{\partial t} = \lambda\vec{\nabla}^2 T + h\nu k_e N_1 + \frac{D_{12}h\nu m_2 n}{\rho}\vec{\nabla}^2 N_1 + \frac{p}{\rho}\frac{\partial\rho}{\partial t} \quad . \tag{29}$$

Operating with $\vec{\nabla}^2$ on both sides, including

$$\vec{\nabla}^4 T = \left(\frac{\partial T}{\partial\rho}\right)_{p_0}\vec{\nabla}^4\rho + \left(\frac{\partial T}{\partial p}\right)_{\rho_0}\vec{\nabla}^4 p \quad . \tag{30}$$

Here, p_0 and ρ_0 denote the constant pressure and mass density, respectively, within the cell in the absence of excitation. Using the equality

$$\frac{\partial^2\rho}{\partial t^2} = \vec{\nabla}^2 p \tag{31a}$$

which is obtained from the continuity and momentum equation, and

$$\vec{\nabla}^4 p = \frac{\partial^2\vec{\nabla}^2\rho}{\partial t^2} \tag{31b}$$

$$\vec{\nabla}^2\frac{\partial p}{\partial t} = \frac{\partial^3\rho}{\partial t^3} \quad , \tag{31c}$$

the density equation can be written as

$$B\frac{\partial^3\rho}{\partial t^3}-E\frac{\partial^2\vec{\nabla}^2\rho}{\partial t^2}+(W-F)\vec{\nabla}^2\frac{\partial\rho}{\partial t}-C\vec{\nabla}^2\vec{\nabla}^2\rho-U\vec{\nabla}^2\vec{\nabla}^2N_1+k_eQ\vec{\nabla}^2N_1=0 \qquad (32)$$

where the coefficient *B, C, E, F, W, U, Q* for ideal gases are given by,

$$B=\frac{C_V}{R} \qquad (32a)$$

$$C=-\frac{RT_0{}^2}{P_0M}\lambda \qquad (32b)$$

$$E=\frac{T_0}{P_0}\lambda \qquad (32c)$$

$$F=\frac{RT_0}{M} \qquad (32d)$$

$$W=-\frac{C_VT_0}{M} \qquad (32e)$$

$$U=\frac{m_2\,N}{\rho_0}D_{12}h\nu \qquad (32f)$$

$$Q=-h\nu \quad . \qquad (32g)$$

In these equations, R is the universal gas constant and T_0 the temperature within the cell in the absence of excitation.

The final differential equations obtained with the three species approach resemble those reported by Barker and Toselli (Barker and Toselli [1988]) (see Eq. (5)). It should be remarked that the factors B, E, F and W (Eq. (32a, b, c, d)) of equation (32) do not experience any changes under this new approach. C (Eq. (32b)) has in contrast an additional term (Eq. (32b)) which is not reported because it is negligible for very low concentrations of excited molecules and can be therefore considered as identical to that obtained with the use of the two-species approach. The coefficients U and Q are, however, new. The similarity encountered in the differential equations within both the three- and two-species approaches (32) and (5), respectively, allows to use the above expression for the time-dependent density equation

$$\rho(r,t)=\sum_{j=1}^{\infty} c_j(t)\, J_0\left(v_j r\right) \quad . \tag{33}$$

The coefficients $c_j(t)$ now include the new identities (32a to g), as follows

$$c_j(t)=\left\{C_{1,j}e^{\left(\alpha_j t\right)}+C_{2,j}e^{\left(r_{1,jj}t\right)}+e^{\left(-a_{2,j}t\right)}\left[C_{3,j}\cos\left(b_{2,j}t\right)+\frac{1}{b_{2,j}}\left(C_{4,j}+a_{2,j}C_{3,j}\right)\sin\left(b_2 t\right)\right]\right\}\cdot \left(\frac{g_j {v_j}^2}{B}\right)\left(U{v_j}^2-k_e Q\right) \tag{34}$$

where $r_{1,j}$ is the real root and $a_{2,j}$ and $b_{2,j}$ are the real and imaginary parts of the complex conjugate roots ($r_{2,j}=a_{2,j}\pm ib_2$) of the cubic equation with variable s

$${s_j}^3+\frac{E{v_j}^2}{B}{s_j}^2-\frac{(W-F){v_j}^2}{B}s-\frac{C{v_j}^4}{B}=0 \quad . \tag{34a}$$

Here the coefficients $C_{1,j}$ to $C_{4,j}$ are given by

$$C_{1,j}=\frac{1}{\left(\alpha_j-r_{1,j}\right)\left[\left(\alpha_j-a_{2,j}\right)^2+{b_{2,j}}^2\right]} \tag{34b}$$

$$C_{2,j}=-\frac{1}{\left(\alpha_j-r_{1,j}\right)\left[\left(r_{1,j}-a_{2,j}\right)^2+{b_{2,j}}^2\right]} \tag{34c}$$

$$C_{3,j}=-\left(C_{1,j}+C_{2,j}\right) \tag{34d}$$

$$C_{4,j}=\left(\frac{{a_{2,j}}^2+{b_{2,j}}^2-\alpha_j r_{1,j}}{\alpha_j+r_{1,j}}\right)\left(C_{1,j}+C_{2,j}\right)+\frac{2a_{2,j}\left(r_1 C_{1,j}+\alpha_j C_{2,j}\right)}{\alpha_j+r_{1,j}} \quad . \tag{34e}$$

Since the mathematical model expressed in equation (33), describes the temporal and spatial dependence of the density after a transient heat production by laser pulse

absorption, this model can be generally applied for the analysis of signals obtained by photothermal (PT) methods. Photothermal beam deflection (PTBD), thermal lens (TL) and fast pulsed photoacoustic (PA) signals are typical representatives.

In the chapters 4 & 5 we applied this model in a study for specifying important characteristics of microphones for PA investigations as well as for the analysis of PTBD signals.

2.4 Remarks

Finally, it should be noted that in the mathematical derivation of section 2.3, the boundary condition of vanishing fluid velocity at the cell wall, or, in terms of acoustic wave, of vanishing density gradient, is not fulfilled. Therefore the obtained equation (33) describes the density variation accurately within the cell, except for values of r near the cell wall and for the reflected acoustic waves which present anomalies due to the assumed boundary condition. However, the reflected acoustic wave is of little interest for most measurements and its influence can be reduced by considering a larger cell radius in the signal processing.

It should also be considered that the influence of convection induced from the gravity in samples with inhomogeneous density is neglected. Convection usually happens in cases when induced density variations at high temperatures become significant enough that gravity effects came into play, so that the less dense, heated portion of the sample rises while the cooler, more dense sample sinks (Whinnery [1967], Cremers and Keller [1982]). As pointed out by Davis and Petuchowski (Davis and Petuchowski [1981]), the influence of convection can be neglected if the displacement of the heated region of the sample is much smaller that the width of the excitation region during thermal diffusion. For pulsed excitation and weakly absorbing media convection does not induce any significant effect.

Chapter 3

Experimental Arrangements

3.1 High Pressure CO_2 Laser

All experiments described in chapter 4 and 5 were performed with a home-built continuously tunable high pressure CO_2 laser. This laser was first accomplished by Repond and Sigrist (Repond and Sigrist [1996/a]) and used for several PA investigations (Repond and Sigrist [1996/b]). The mechanical and electrical design of the laser is similar to that of the CO_2 laser amplifier presented by Kesselring and co-workers (Kesselring et al. [1993]). In view of better stability and higher repetition rates, a lot of effort has been invested to upgrade the previous setting of the laser. In the following, the original set-up as described by Repond and Sigrist is briefly reported. Emphasis is put on the effectuated modifications. Present laser characteristics are described and reported in Table 3.1.

3.1.1 Discharge

The original design of Repond and Sigrist (Repond and Sigrist [1996/a]) featured a laser tube with an inner diameter of 50 mm. The tube was manufactured from a Makrolon (policarbonat) rod and sealed with Brewster windows made of 5 mm thick uncoated ZnSe plates. The 32 cm long brass electrodes are milled in tangential section sides according to an Ernst profile (Ernst [1983, 1984]) in order to obtain a spatial uniform electric field. The UV preionisation is of the sliding-spark type. The preionisation rods are fixed on the side of the brass electrodes (see Fig. 3.1). The arc discharges between 1 cm long pieces of nickel wire pieces with a diameter of 1.5 mm, and separated by 1 mm gaps generate the required UV illumination needed for the preionisation of the laser gas in order to favour a homogeneous discharge between the brass electrodes (Werling [1988]). In the configuration reported by Repond and Sigrist (Repond and Sigrist [1996/a]) the laser operates at a gas pressure of about 11.5 bar with a premixed gas mixture composed of $CO_2 : N_2 : He = 5 : 5 : 90$ at a flow rate of ca. 1.7 $l \cdot min^{-1}$. Although the discharge repetition rate was 0.2 Hz, the occurrence of arc discharges reduced the actual laser emission repetition rate by 10%.

In order to achieve a better pulse-to-pulse stability and higher pulse repetition rates two measures were taken. The first one included a change of the electronic control responsible for the charging process of laser capacitors and the trigger electronic circuit of the discharge. This modification permits a variable discharge repetition rate between 0.1 to 1.5 Hz. However, the original laser pulse repetition rate of 0.2 Hz could not be increased by this procedure because most discharges were of arcing type instead of the desired glow discharges. The arcing occurred near the borders of the brass electrodes which is due to the influence of the preionizer rods that modified the electric field between the brass electrodes. In fact, at high gas pressures the discharges are highly unstable, and minimum fluctuations of the free electron density lead to the formation of arcs (Jaeger and Wang [1987]). An effective elimination of these arcs could only be obtained by sticking an adhesive insulating tape along the borders of the brass electrodes.

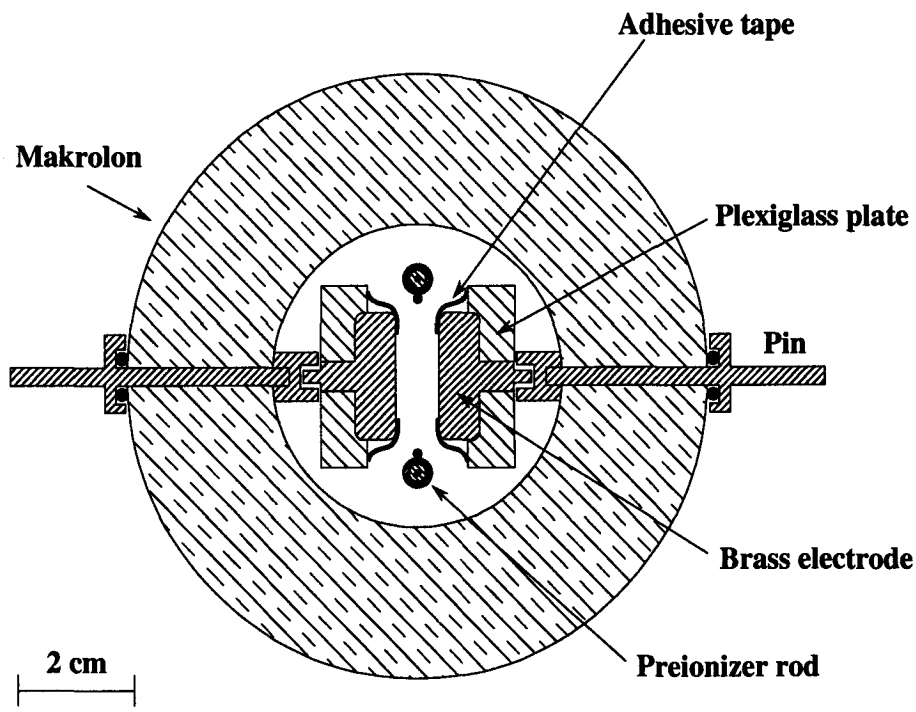

Figure 3.1. *Simplified cross sectional view of the high pressure CO_2 laser as reported by Repond and Sigrist (Repond and Sigrist [1996/a]) with the additional adhesive tapes.*

This unconventional solution resulted in homogeneous gas discharges and an improved pulse-to-pulse stability. The pulse repetition rate could be increased up to 1 Hz by slightly reducing the laser gas pressure and flow to 10 bar and to 0.2 $l \cdot min^{-1}$, respectively. However, optimal laser operation with stable pulse energy was achieved with a pulse repetition rate below 0.7 Hz. By increasing the pulse frequency up to 1 Hz, the pulse energy exhibits a stronger fluctuation although the discharge remains homogeneous. By a

further increase of the discharge rate arcing discharges take place and laser activity does not occur for every discharge anymore. Intracavity thermal lens measurements during laser operation have shown that the gas density equilibrates after about 1 sec, which explains well the restriction of the repetition rate to 1 Hz.

3.1.2 Optical Design

As reported by Repond and Sigrist (Repond and Sigrist [1996/a]), the laser is equipped with a Littman resonator and the tuning is achieved by rotating a flat cavity mirror (M_2 in Fig. 3.2) by means of a computer-controlled high-resolution DC motor. The grating is mounted at a large incidence angle of 77^0 much larger than the 52.7^0 grating blaze angle. Thanks to the large groove coverage and the double pass of the beam on the grating, this configuration is suitable to obtain small bandwidths still maintaining cavity losses suitable for laser activity. In fact cavity losses become significant when increasing the incident angle, since the zeroth-order outcoupling efficiency increases (Raouf [1987]) and, for angles exceeding the blaze angle, a second zeroth-order outcoupling takes place from the reflection of the mirror M_2. The aperture *A* (see Fig. 3.2) further enhances the overall resonator losses, favouring thereby oscillation in the TEM_{00} mode.

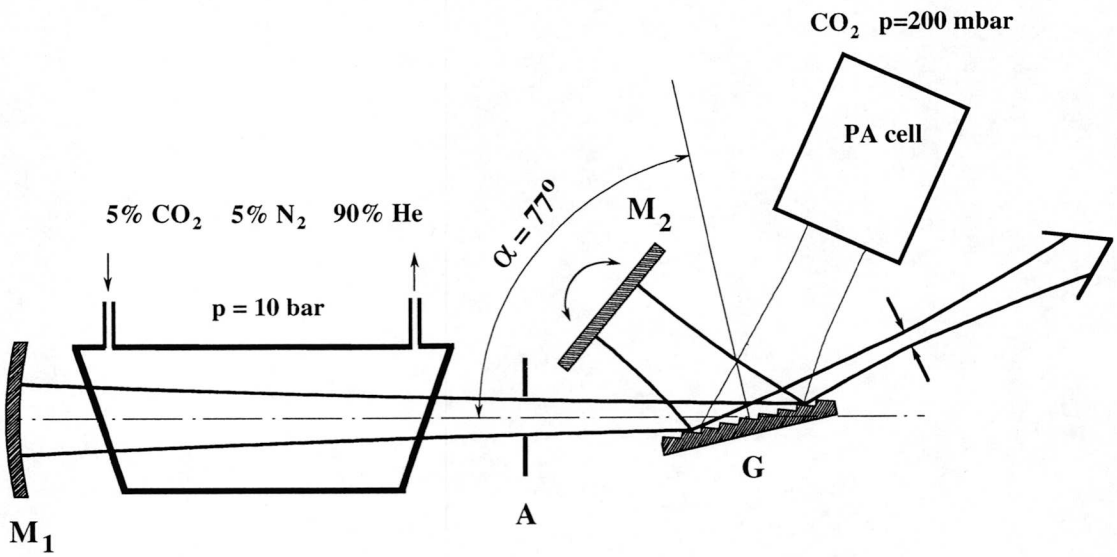

Figure 3.2. *Optical resonator (not in scale) as reported by Repond and Sigrist (Repond and Sigrist [1996/a]). The resonator length is 1.05 m while the distance M_2G is 59 mm. The signals recorded in the photoacoustic (PA) cell filled with 200 mbar CO_2 serve as frequency markers for the spectroscopic measurements.*

As shown in Figure 3.2, the second zeroth-order (hitherto unused) grating reflection is directed through a photoacoustic cell filled with 200 mbar of CO_2 gas used to infer the laser radiation wavelength. At such a reduced pressure, the width of the CO_2 gas absorption lines are small. The transitions can be accurately identified via the photoacoustic signal by tuning the laser wavelength by means of a high-resolution rotational stage (wavelength resolution of $6.8 \cdot 10^{-3}$ cm^{-1} corresponding to 25 encoder counts) across the transition. Fitting the acquired photoacoustic data by a Lorentzian profile allows to locate the centre of the absorption lines with an accuracy equal to the wavelength resolution of the tuning mechanism. Through a computer controlled process that identifies the centre of transition and uses the latter as wavelength marker, the wavelength of the laser radiation is automatically derived.

Furthermore, in order to protect the mirror M_1 we inserted it into a Faraday box that contains the laser tube and the high voltage electronics, reducing the original resonator length M_1M_2 from 1.29 to 1.15 m by diminishing the distance between mirror M_1 and grating G. Measurements have shown that this reduction does not affect the laser performance.

3.1.3 Performance

The laser allows pulsed operation with a continuous tunability in all four branches, i.e. 9R, 9P, 10R and 10P of the emission spectrum of the CO_2, laser for a total range of 76 cm^{-1} between 9.2 and 10.8 μm. The tuning behaviour is linear throughout the entire tuning range and an absolute accuracy in wavelength calibration of $\pm 10^{-2}$ cm^{-1} is achieved. A narrow linewidth of 0.017 cm^{-1} corresponding to about 500 MHz and pulse duration of ca. 140 ns (FWHM) is obtained. The laser pulse energy is controlled by the voltage applied to the capacitors. At a pulse repetition rate of 0.7 Hz, the laser pulse energy is in the range between 10 mJ and of 70 mJ. At higher energies, sparks form at the surface of the grating resulting in the destruction of the grooves. Optimum energy stability is achieved at ca. 30 mJ where the fluctuations are less that 5 %. The discharge failure rate due to arcing between the brass electrodes is below 1 %. Thanks to the achieved stabilisation of the laser, a lifetime of laser activity of about 450 hours, corresponding to approximately $1.1 \cdot 10^6$ pulses at 0.7 Hz and 30 mJ pulse energy, is achieved before the incidence of arcing increases dramatically requiring the replacement of the preionizer rods (Knittel et al. [1995]). Table 3.1 summarizes the laser characteristics.

Table 3.1. *Laser characteristics of the high pressure CO_2 laser*

Operation pressure	10 bar
Gas composition	$CO_2 : N_2 : He = 5 : 5 : 90$
Tunability : continuously (totally 76 cm^{-1})	from 10P(32) to 10P(8), from 10R(6) to 10R(30), from 9P(28) to 9P(8), from 9R(4) to 9R(36)
Linewidth	0.017 cm^{-1} ≅ 500 MHz
Pulse duration	140 ns
Pulse energy	10 mJ to 70 mJ
Repetition rate	0.1 Hz to 1 Hz
Pulse energy stability	< 5 % @ 0.7 Hz
Absolute tuning accuracy	$\pm 10^{-2}$ cm^{-1}
Lifetime	450 hours or $1.1 \cdot 10^6$ pulses at 0.7 Hz and 30 mJ pulse energy.

3.2 Experimental Setup for Photoacoustic Studies

The tuning characteristics, the narrow linewidth and the good pulse-to-pulse energy stability render the CO_2 laser described above a versatile light source for spectroscopic studies. Several photoacoustic (PA) investigations on trace gases and gas mixtures have been performed with this laser (Repond [1995], Repond and Sigrist [1996/a-b]). The PA arrangement employed is shown in figure 3.3. It is similar to the one reported earlier by Repond and Sigrist (Repond and Sigrist [1996/b]). Here only a briefly description is given with focus placed on some alterations made. The PA setup consists of the continuously tunable CO_2 and a non-resonant PA cell (of type A see (Repond [1995], Repond and Sigrist [1996/b])). The PA cell is machined of a stainless steel, has a length of 412 mm and an inner diameter of 14 mm, and is sealed by uncoated ZnSe Brewster windows. The CO_2 laser beam is slightly focused into the PA cell with a long focal length mirror. After crossing the cell, the radiation is directed to a pyroelectric detector (Molectron J25) with a responsivity of 32.6 V/J for the measurement of the pulse energy.

A miniature electret microphone (Knowles 3133) placed at the centre of the cell with its membrane flush with the wall, records the transient pressure changes. The microphone signal is amplified (hundredfold) by a new amplifier with a bandwidth of 20 kHz. The amplifier and the battery supply are accommodated in a shielding box near the microphone. The use of this amplifier reduced previously described electrical perturbations (Repond [1995]) caused by the strong electrical field of the laser discharge.

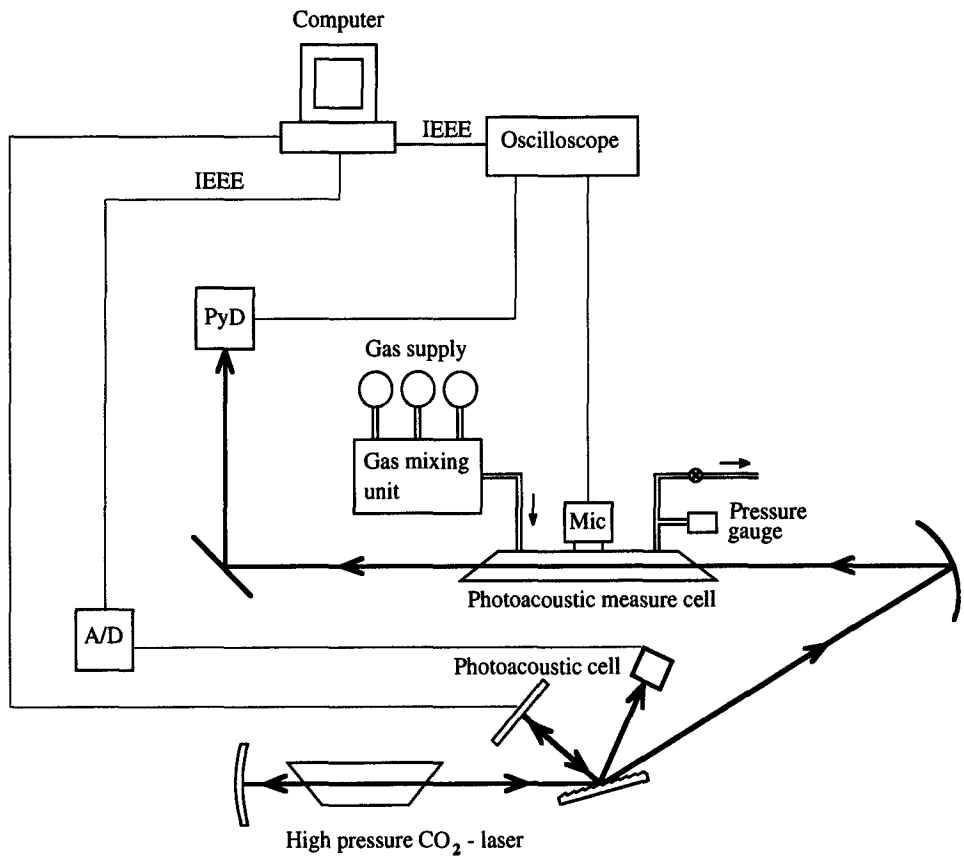

Figure 3.3. *Experimental setup for PA investigations with the continuously tunable CO_2 laser. The laser is tuned by rotating the flat cavity mirror. A grating reflection is used to record continuously the laser wavelength with the aid of a photoacoustic cell and A/D converter. The pyroelectric detector (PyD) serves to measure the laser pulse energy. The microphone (Mic) records the PA pulse of the gas under study.*

Finally, a passive lowpass filter with a cut-off frequency of 9.8 kHz mounted at the entrance port of the oscilloscope (Lecroy 9450), reduced random noise and the electrical perturbations picked up by the 1 m long cable connecting the oscilloscope and the amplifier. These modifications resulted in a tenfold sensitivity enhancement when compared to previous experiments. The entire system is computer-controlled and allows comfortable handling and data recording. Thanks to the stability and handling facilities of

the CO_2 laser achieved with the modifications described above, it was possible to improve the control software of the PA system reaching a user friendly configuration and a data recording practically without the need of external intervention. A more detailed description of the system is found elsewhere (Calasso et al. [1997], Repond and Sigrist [1994, 1996/a]).

3.3 Experimental Setup for Photothermal Beam Deflection Studies

The experimental setup used for the PTBD studies is presented in Fig 3.4.

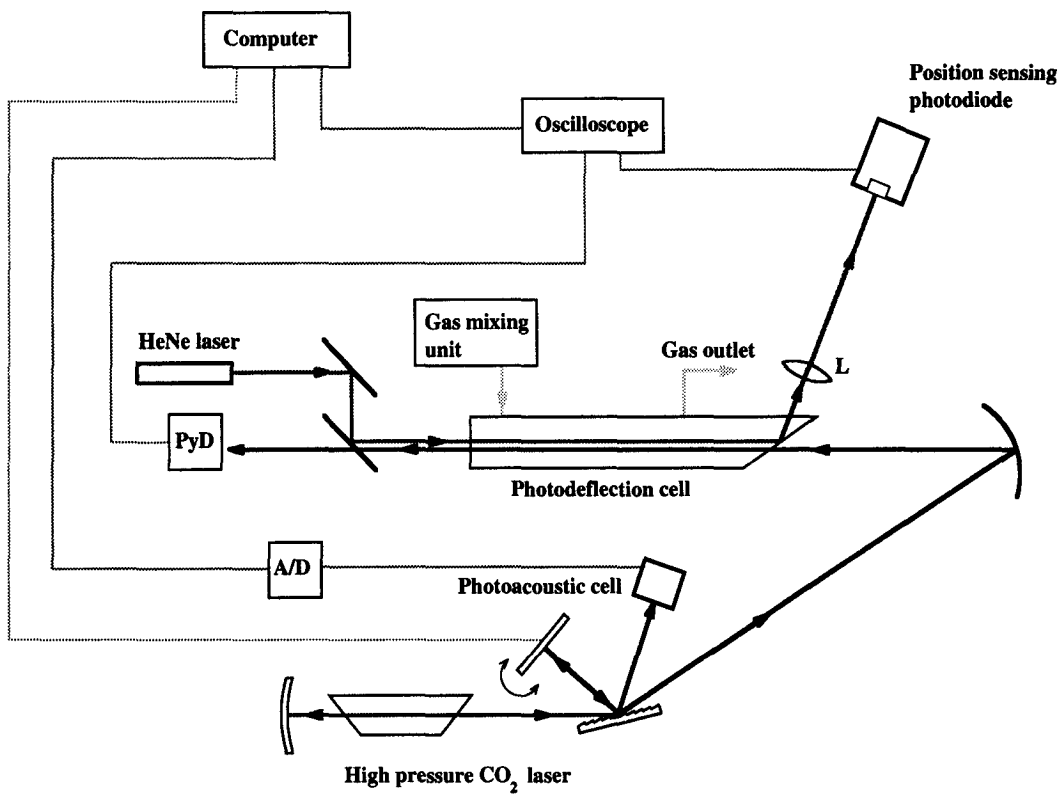

Figure 3.4. *Experimental setup for photothermal beam deflection studies with the high pressure CO_2 laser. The laser is tuned by rotating the flat cavity mirror. A grating reflection is used to record continuously the laser wavelength with the aid of a photoacoustic cell and A/D converter. The pyroelectric detector (PyD) serves to measure the laser pulse energy. The lens L with focal length of 1 m allows an amplification of the deflection (see text). The beam deflection is sensed either by a position sensor or a knife-edge and photodiode.*

The beam of our continuously tunable high pressure CO_2 laser (see section 3.1) is used as a pump beam in the forthcoming PTBD experiments. This beam is slightly focused to a

diameter of typically 3 mm and directed through a cylindrical cell that contains the gas mixture under study with a long focal length mirror. The cell (40 cm long, 3.5 cm inner radius) is made out of stainless steel. It is closed on the side of the incoming CO_2 laser pump beam by an uncoated ZnSe Brewster window. The opposite side is sealed with a flat ZnSe window, AR coated for HeNe and CO_2 wavelengths. Additionally, a quartz window near the Brewster window is used to couple out the HeNe laser beam. After traversing the cell, the pump laser pulse energy is monitored with a pyroelectric detector. The beam of a cw HeNe laser (probe beam) is directed through the cell parallel to the CO_2 laser beam (pump beam) at a variable distance *d*. Its polarisation direction is perpendicular to that of the CO_2 laser in order to obtain a reflection at the Brewster window. This reflection is then coupled out by the quartz windows. The probe beam deflection is sensed by a position sensor (UDT LSC-5D) having a detector surface of 5.33 x 2.15 mm and a spatial resolution of 10 μm or by using the same sensor as a photodiode in the combination with a knife edge. Both configurations yield a rise time of 0.3 μs. The lens L (focal length of 1 m) is placed near the cell allows to increase the distance between cell and detector. This results in a larger displacement of the HeNe laser spot on the detector and thus of the sensitivity by still maintaining the spot on the detector surface. It should be pointed out that only lenses with long focal distance are appropriate. In fact, only when the focal point of the lens, on the side facing the cell, has a length longer than the cell length so that it is well outside the cell, the lens focuses the beam thereby letting the displacement invariant. In the other case, when the focus of the lens does not extend beyond the cell, the lens focuses the probe beam and the displacement is even reduced. The detector and cell are separated by approximately 2.3 m, which is the maximum distance allowing to maintain the HeNe spot on the detector. The PTBD signals are recorded by a digital oscilloscope (LeCroy 9361). Our measurement on gases and gas mixtures have been performed by the use of a gas mixing unit (MKS GMS6), provided with individual gas bottles at certified concentrations. This device was used either to dilute the absorbing gas to be analysed in a nonabsorbing buffer gas, or to prepare multicomponent mixtures of reliable concentrations. Six mass flow controllers with a full scale range extending form 10 SCCM (cm^3 min^{-1} at STP) to 200 SCCM allow the preparation of concentrations with an error between 0.9 % and 5 %.

Chapter 4

Photoacoustic Investigations

In the first section of this chapter, theoretical and experimental investigations aimed to optimize the detection performance in non-resonant pulsed photoacoustic (PA) studies by selecting microphones with appropriate characteristics are presented. Comparisons between various condenser and electret microphones having different characteristics are performed using 100 ppm ethylene buffered in synthetic air. The measurements confirm the theoretical expectations. Based solely on the knowledge of microphone specifications the theory allows the selection of the most appropriate microphone.

The second section describes on a PA study on a mixture containing six CO_2 isotopes. Their concentrations could be determined with a good accuracy. Furthermore, previously unknown absorption cross sections of some important lines of the $^{12}C^{18}O_2$, $^{13}C^{18}O_2$ and $^{16}O^{13}C^{18}O$ isotopes in the 9 to 11 μm range are reported.

4.1 Microphones for Pulsed PA Investigations

In photoacoustic measurements microphones are generally used as sensing elements of the acoustic waves generated by the heat deposition of the absorbing molecules. The microphone characteristics therefore play an important role for the pressure wave detection. The selection of a microphone is a compromise between many factors. It is actually impossible to select a microphone that is suitable for PA measurement under any condition. In practice, it is necessary to select from the most significant features of the microphone, such as responsivity, dynamic range, and frequency dependence, those that are particularly important for the specific PA measurement. To our knowledge this important aspect has not been investigated in detail hitherto. For the detection of the fast processes involved in generation of the acoustic wave, piezoelectric transducers with a large bandwidth of ca 1 MHz, but with the disadvantage of small responsivity, were used to resolve ballistic pressure pulses (Beck and Gordon [1988], Tam [1986]). On the other hand, for trace gas monitoring, where the responsivity and linear dynamic range are the important features, microphones with high responsivity but with the disadvantage of small bandwidths of about 20 kHz, were applied (Tam [1986], Schäfer [1997]). In this section we attempt to provide a guide for the selection of the most appropriate microphone

for trace gas detection by pulsed PA. The key issue is to increase the signal-to-noise ratio (SNR) in order to improve the detection limit. Besides microphone characteristics, other factors contribute to the improvement of the SNR. The signal amplitude depends on the laser pulse energy but due to saturation effects it can not be arbitrarily increased by enlarging the laser pulse energy. On the other side, the important reduction of noise sources is not easy to realize in practice and only of limited use. In fact, various noise sources are involved in PA measurements (Melander [1997]). It can be distinguished between two types of noise: random or coherent external ambient noise, produced by, e.g., window heating, electrical discharge, or other external noise sources, and microphone-amplifier random noise. Elaborate shielding techniques are required to reduce external random noise. More feasible is the reduction in the case of coherent noise. Microphone noise, which is manifested as a noise voltage present at the microphone output terminals can be expressed as the product between the normalized noise pressure value due to thermal agitation of the diaphragm and the cartridge responsivity at the corresponding frequency and the square root of the measurement bandwidth. The noise spectrum corresponds to the cartridge frequency response when measured with a constant bandwidth; responsivity and noise level of microphones are therefore related to each other. Hence the use of high responsivity microphones does not increase the SNR significantly. Additionally, inevitable electrical noise, in general at a level lower than the microphone noise, is also superimposed to the signal. The ultimate solution towards increasing the SNR is to adapt the microphone characteristics like responsivity and frequency response to the generated PA signal in order to take full advantage of the energy stored in the PA pulse.

In the following, we present a theoretical study to obtain the required microphone characteristics that allow to maximize the PA signal. Furthermore, we discuss the results obtained with two types of high-quality condenser microphones of different characteristics as well as with three types of electret microphones.

4.1.1 Analysis of Microphone Signals

The linear relation (for small fluctuations) between density variation and pressure variation (Morse [1936]) in an acoustic wave enable to use the mathematical density description reported in equation (33) for simulations of the PA pressure pulse. It should be noted that the use of this approach is justified in the beam deflection part of this study by the excellent agreement between theory and measurements. Although this equation considers the contributions to the signal shape by thermal conductivity and molecular

diffusivity, the contribution of these parameters outside the laser-irradiated region and at atmospheric pressure can be neglected.

Important parameters of the PA pulse are the laser beam radius r_b, the laser pulsewidth, the acoustic velocity, thermal diffusivity, binary diffusivity, and molecular relaxation times τ_{relax} (chapter 1 of this study, Pugh [1989], Tam [1986]). In the case considered here where τ_{relax} is shorter than both, the acoustic transit time $\tau_S = r_b/v_S$, which is the time the acoustic pulse takes to cross the beam radius and the thermal diffusivity time $\tau_\kappa = r_b^2/4\kappa$, where κ is the thermal diffusivity, the dependence of the laser pulsewidth can be neglected. In such a case the relaxation time influences the temporal behaviour of the pressure pulse while the length of the PA pulse depends more on the acoustic transit time τ_S.

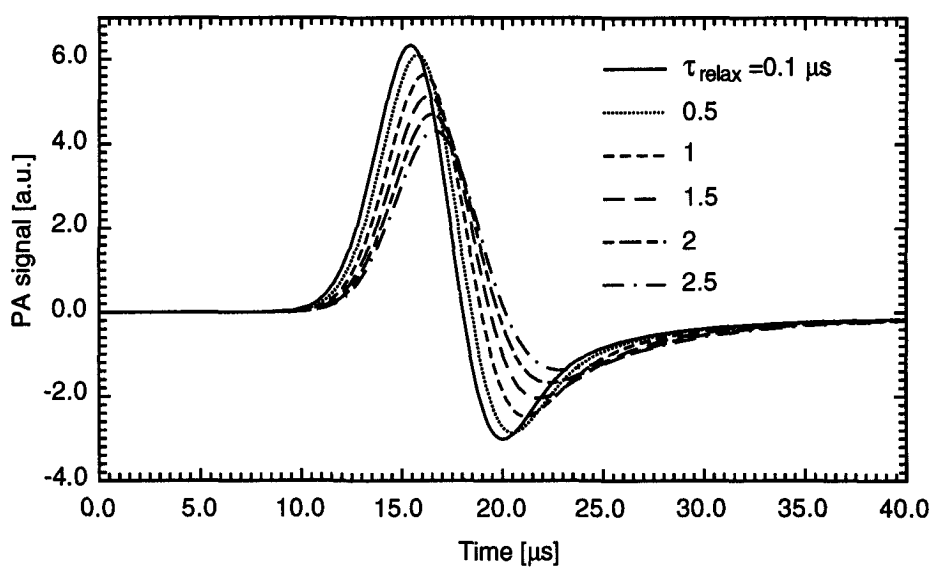

Figure 4.1. *Calculated PA pulse shapes for a highly diluted absorbing gas for different relaxation times τ_{relax} at a distance of 2 cm from the laser beam and for a radius of 1 mm. The time scale indicated in the figure is shifted for clarity.*

Figure 4.1 illustrates shapes of PA pressure pulse calculated from the density equation (33) assuming a strongly diluted absorbing gas in synthetic air (80 % N_2 and 20 % O_2) at 950 mbar, a distance of 2 cm from the laser beam with a radius of 1 mm, and for relaxation times τ_{relax} of 0.1, 0.5, 1, 1.5, 2, 2.5 μs. These are realistic times, as demonstrated by our beam deflection studies (section 5.5) and other investigations (Yuan and Flynn [1973/a]). Different PA signal shapes and peak amplitudes are obtained for varying τ_{relax}; the convergent behaviour is evident. For the example shown, the pulse shape obtained for τ_{relax} = 0.1 μs essentially represents the convergence limit, i.e. relaxation times below 0.1 μs generate PA pulses like the one for τ_{relax} = 0.1 μs. This

behaviour is explicitly studied in the photothermal beam deflection part of this work (section 5.4) where it is demonstrated that convergence occurs when the relaxation time becomes considerably shorter than the acoustic transit time. Hence, convergence sets in at longer times for larger laser beam radii.

If the microphone employed in a PA measurement completely resolves the acoustic pulse shapes, the dependence of the peak amplitude on the relaxation time looks as an unwelcome behaviour for PA spectroscopy measurements. In fact, the relaxation time of an absorbing molecule in a mixture depends on all constituents present in the gas mixture. In PA spectroscopy the concentration of the components is obtained through reference spectra sometimes measured under different relaxation conditions than those valid for multicomponent mixture. In such a case, the peak amplitude of the PA pulse from reference spectra differs from that of the mixture. Therefore, the use of reference spectra could predict an erroneous concentration value. However, the important key for the validity of this consideration is that the microphone resolves the acoustic pulse. This would require microphones with a large bandwidth on the order of a few 100 kHz as demonstrated by the Fourier transform spectra (FFT) of the calculated signals presented in Fig. 4.2.

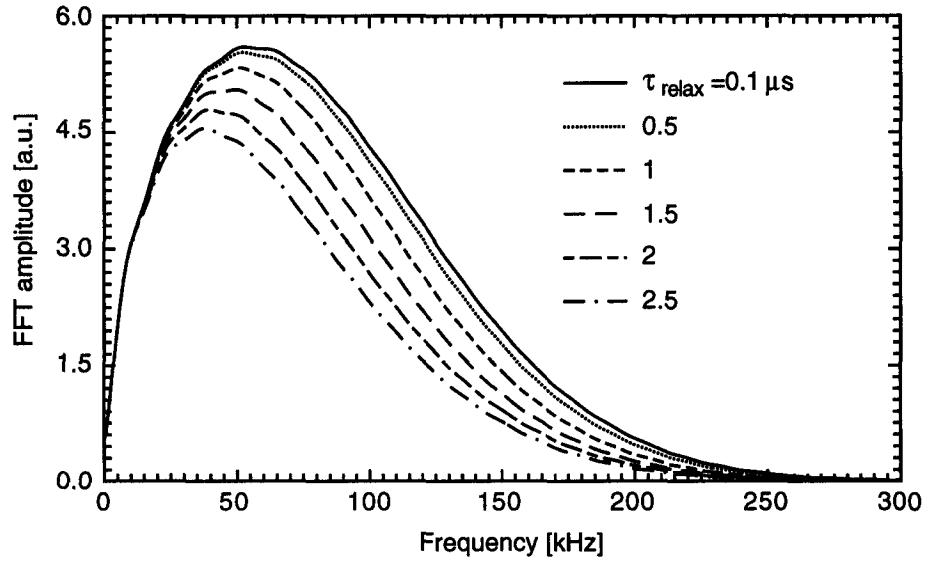

Figure 4.2. *Fast Fourier transform of the calculated photoacoustic pulses illustrated above in Fig. 4.1 for different relaxation times* τ_{relax}.

A different situation is encountered if standard microphones with bandwidths of a few 10 kHz are used. In this case, only minor deviations in amplitude result for different τ_{relax}. For example the amplitude deviation between the curve obtained for 0.1 μs and that for 2.5 μs is below 0.95 % for frequencies ≤ 10 kHz. From 10 to 15 kHz the

deviation reaches 2.60 %, and from 15 to 20 kHz 5.21 %. On the other hand for higher frequencies e.g. at 50 kHz the deviation becomes 27.22 % and at 60 kHz reaches 38.11 %. It is therefore necessary to pay attention to the bandwidth of microphones when taking reference spectra. Furthermore it should be noted, that the frequency bandwidth involved in PA pulses depends on the laser beam radius as it is shown below in Fig. 4.4. The larger the laser beam radius, the smaller is the frequency bandwidth and consequently we would expect that the frequency range with similar amplitudes becomes smaller. This enhances the problems with reference spectra and the microphone bandwidth mentioned above. However, a further consideration that also takes care of the convergence behaviour of the signal shapes as function of the relaxation time, changes the expectations. A very similar frequency deviation of pressure pulse amplitudes is obtained for different pump radii and identical relaxation time variations between 0.1 and 2.5 μs as considered above in Fig. 4.2. As an example, an increase of the beam radius to 2.5 mm results in a signal deviation of only 0.98 % at 10 kHz, 2.62 % at 15 kHz, 5.26 % at 20 kHz, 17.69 % at 40 kHz and 39.43 % at 60 kHz. These data are comparable to those for a beam radius of 1 mm. Hence, we conclude that relaxation time and microphone bandwidth considerations cannot be avoided when changing the dimension of the laser beam radius. However, small beam radii are advantageous to enhance PA signal amplitudes in actual measurements as is shown in Fig. 4.3.

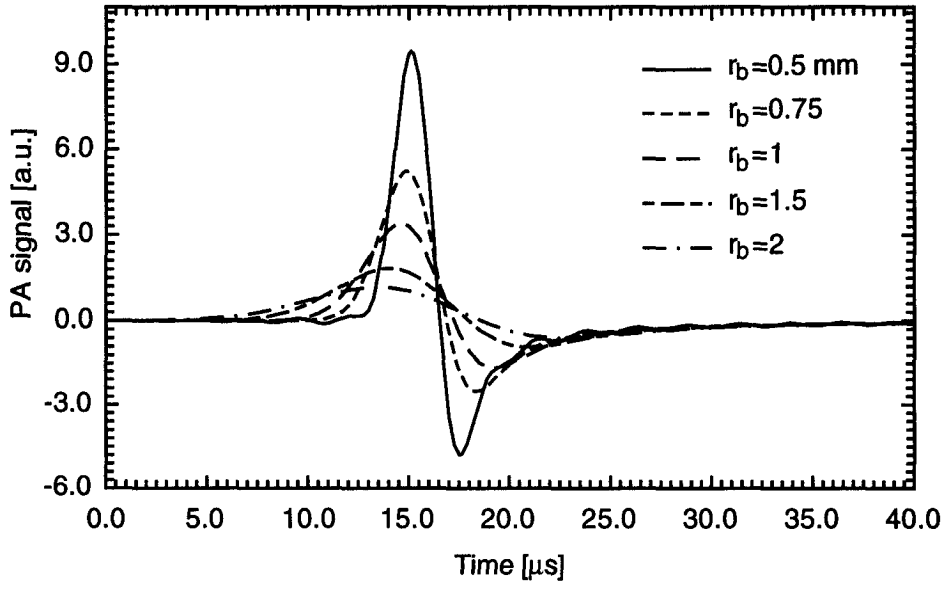

Figure 4.3. *Photoacoustic pulse shapes calculated for a strongly diluted absorbing gas buffered in air at 950 mbar with a relaxation time of 0.1 μs for different laser beam radii r_b at a distance of 2 cm from the laser beam.*

Here, calculated PA pressure pulses are plotted for the convergent case with τ_{relax} = 0.1 μs, for beam radii of 2, 1.5, 1, 0.75, 0.5 mm and for constant laser pulse energy. For all laser radii similar shapes are obtained. However, higher peak amplitudes and shorter time differences between the maximum and minimum of the signal are observed for smaller laser radii. The higher peak amplitude for small radii are not only an obvious manifestation of the higher temperature generated locally in the laser beam region with increased laser intensity, but occurs also when the beam radius is reduced and the laser intensity is kept constant. The shorter time difference Δt_{pk-tr} between the positive and negative peaks for smaller laser radii can be understood as a consequence of the size of the spatial perturbation generated by the laser. Tam (Tam [1986]) gives an estimation of $\Delta t_{pk-tr} = 1.66 \cdot \sqrt{\tau_L{}^2 + \tau_S{}^2}$ that takes into account also the laser pulsewidth τ_L. Considering the short laser pulses in our case, and the definition of the acoustic transit time, one gets $\Delta t_{pk-tr} = 1.66 \cdot r_b / v_S$ which agrees well with our experimental results. Obviously, the higher PA signal amplitudes at reduced beam radii can fully be exploited only by using microphones with a broadband frequency response. In fact, the Fourier transforms of the calculated acoustic pulses presented in Fig. 4.3 demonstrate that recordings with standard microphones with frequency response up to 20 kHz yield almost identical signal shapes for different radii (Fig. 4.4). The results in Fig. 4.4 imply that the range with identical frequency amplitude becomes larger at reduced beam radii and extends to 60 kHz for r_b = 0.5 mm.

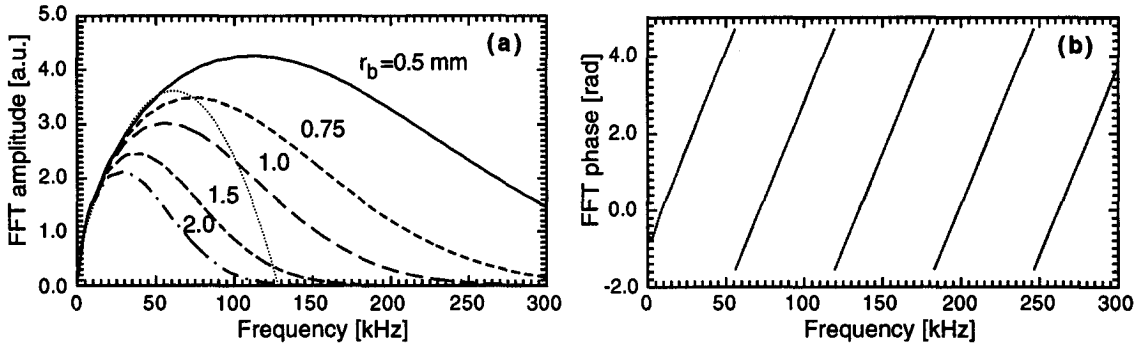

Figure 4.4. *FFT transformation amplitude (a) and phase (b) of the acoustic pulse for laser radii of 2, 1.5, 1, 0.75, and 0. 5 mm. In (a) the dotted thin line represents a parabolic fit of the curve referring to a beam radius of 0.5 mm (solid line) for frequencies up to 60 kHz.*

The phase function, illustrated in Fig. 4.4b for a beam radius r_b = 0.5mm, exhibits periodical lines with a period of about 60 kHz. The function is independent of r_b as it can be shown mathematically by analyzing the density equation and considering that each term of the series can be separated into two functions, one containing the beam radius and

another time dependent part. For beam radii below 0.5 mm and frequencies below 60 kHz, the amplitude and phase function of the FFT can therefore be considered as constant.

4.1.2 Microphone Bandwidth

Considering the broad frequency range present in the PA signal for small beam radii, microphones with large frequency bandwidths seem to be more appropriate for the detection of trace gases. In what follows we present a more complete analysis of the SNR and demonstrate the validity of this conclusion.

For this issue we simplify the analysis by making the following assumptions:

- The spectrum of the acoustic pulse is assumed as a rectangular function;
- The microphone frequency response in the range of the acoustic spectrum is also a rectangular function with a bandwidth $\Delta\nu$.

With these assumptions the PA amplitude can easily be derived. Since the measurement with a microphone can be considered as a convolution between the PA pulse and the transmission function of the microphone, the inverse Fourier transform method allows the simulation of the PA signal.

Since the amplitude of the inverse Fourier transformation of a rectangular function with bandwidth $\Delta\nu$ is proportional to $\Delta\nu$, the PA voltage V_{PA} amplitude is also proportional to the microphone bandwidth, and can be written as

$$V_{PA} \propto \alpha \cdot R \cdot \Delta\nu \quad , \tag{35}$$

where R indicates the microphone responsivity and α the amplification factor of the amplifier used. The total mean square noise voltage level $\overline{V}_T^2$ in the measurement is expressed as the sum of all mean square noise voltages involved, i.e.

$$\overline{V}_T^2 = \overline{V}_M^2 + \overline{V}_X^2 \quad , \tag{36}$$

where $\overline{V}_M^2$ represents the microphone noise due to the thermal pressure fluctuations and $\overline{V}_X^2$ denotes the sum of all other noise sources. The microphone noise $\overline{V}_M$ is the product of the microphone responsivity and the noise pressure $\overline{p}$ (Brüel & Kjær, Data Handbook [1982] p. 67) acting on the microphone diaphragm. The latter can be written as

$$\overline{p} = \sqrt{4 \cdot k \cdot T \cdot D \cdot \Delta\nu} \quad , \tag{37}$$

where D [Nsm^{-5}] is the acoustic damping resistance of the diaphragm system.
Considering the assumed flat microphone frequency response, the mean thermal-noise voltage level due to the thermal pressure fluctuation becomes

$$\overline{V}_M = \alpha \cdot R \cdot \sqrt{4 \cdot k \cdot T \cdot D \cdot \Delta\nu} \quad . \tag{38}$$

The SNR is now written as

$$\frac{Signal}{Noise} = \frac{V_{PA}}{\sqrt{\overline{V}_M{}^2 + \overline{V}_X{}^2}} \tag{39}$$

or, by substituting Eqs. (35) and (38),

$$\frac{Signal}{Noise} \propto \frac{\alpha \cdot R \cdot \Delta\nu}{\sqrt{\alpha^2 \cdot R^2 \cdot 4kTD \cdot \Delta\nu + \overline{V}_X{}^2}} \quad . \tag{40}$$

Realizing that the microphone responsivity is proportional to the microphone diaphragm surface A,

$$R \propto A \quad , \tag{41}$$

large diaphragm surfaces imply large masses of the latter and therefore reduced vibration ability. Hence, we assume that the microphone bandwidth $\Delta\nu$ is inversely proportional to the square root of the diaphragm mass, or to the surface A,

$$\Delta\nu \propto \frac{1}{\sqrt{A}} \quad . \tag{42}$$

Using equations (41) and (42) and by introducing a constant γ as a proportionality factor, we derive the responsivity R as

$$R = \gamma \frac{1}{\Delta\nu^2} \quad . \tag{43}$$

With this last equation, the SNR can be written as function of $\Delta\nu$

$$\frac{Signal}{Noise} \propto \frac{1}{\sqrt{\frac{4kTD}{\Delta\nu} + \frac{\overline{V}_X^2 \cdot \Delta\nu^2}{\alpha^2 \cdot \gamma^2}}} \quad . \tag{44}$$

This equation implies that the maximum SNR is obtained for a certain bandwidth $\Delta\nu$. Furthermore, it also indicates that for a very large $\Delta\nu$, the SNR tends to zero. This behaviour occurs because in the measurement there are additional noise sources $\overline{V}_X$ apart from the microphone thermal noise and that the bandwidth acts as an amplification term for such $\overline{V}_X$. In order to roughly estimate the optimum bandwidth for a microphone we consider the specifications of the broadband Brüel & Kjær microphone 4135 used in this work: $\Delta\nu$ = 100 kHz, responsivity R = 3.43 mV/Pa, cartridge thermal noise of $5.7 \cdot 10^{-6}\ Pa/\sqrt{Hz}$. With this data, the terms $(4 \cdot k \cdot T \cdot D)$ and γ can be calculated with Eqs. (37) and (43), respectively. Assuming an amplifier amplification factor $\alpha = 100$, the microphone bandwidth $\Delta\nu$ that yields maximum SNR according to Eq. (44) is obtained by solving the following relation

$$\overline{V}_X^2 \cdot \Delta\nu^3 = 0.194 \quad [V^2 \cdot kHz^3] \quad . \tag{45}$$

Assuming an external noise voltage $\overline{V}_X = 1$ mV, the maximum SNR is obtained for $\Delta\nu \approx 60$ kHz. For $\overline{V}_X > 1$ mV as encountered in our experiments, microphones with $\Delta\nu < 60$ kHz are thus better suited for achieving high SNR. However, it should be emphasized that the SNR expressed in equation (44) is only a rough approximation. A more rigorous approach is obtained by restricting the analysis to the microphones with $\Delta\nu < 60$ kHz and assuming the true frequency information up to 60 kHz contained in a PA pressure pulse instead of the rectangular function as used above. This analysis is presented in the following section.

4.1.3 Microphones with a Bandwidth < 60 kHz

In order to better evaluate the appropriate specifications of a microphone, we restrict the analysis to microphones with $\Delta\nu < 60$ kHz and approximate the PA FFT amplitude and phase for a laser beam radius of 0.5 mm and frequencies ≤ 60 kHz with a parabolic and a linear fit (see Fig. 4.4 above). The frequency limit chosen is in agreement with the previous noise considerations, covers a large spectrum of available microphones and offers a simple description of the occurring PA signal frequencies for signals related to laser beam radii below 0.5 mm. To further simplify the theoretical analysis, we again

assume that the microphone frequency response is a rectangular function with an amplitude R identifiable as the responsivity with a lower frequency limit ν_S and an upper frequency limit ν_E.

The PA signal amplitude is obtained from the inverse Fourier transform of the multiplication between the rectangular function that represents the microphone frequency response and the parabolic approximation of the amplitude and phase of the FFT of the PA pulse

$$PA(\nu) \propto \left(a\nu^2 + b\nu + c\right) \cdot e^{i\cdot(\alpha\nu+\beta)} \quad . \tag{46}$$

The PA peak voltage V_{PA} is proportional to the maximum value over the time of the calculated time-dependent PA pulse expressed between brackets in the following expression

$$V_{PA} \propto \max_t \left\{ R \cdot \int_{\nu_S}^{\nu_E} \left(a\nu^2 + b\nu + c\right) e^{i(\alpha\nu+\beta)} e^{i\nu t} d\nu \right\} \quad . \tag{47}$$

The solution of Eq. (47) can be approximated by

$$V_{PA} \propto R \cdot \left(\nu_E - \nu_S\right) \left[c + \frac{1}{2} b \left(\nu_E + \nu_S\right) + \frac{1}{3} a \left(\nu_E{}^2 + \nu_E \nu_S + \nu_S{}^2\right) \right] \quad , \tag{48}$$

where the constants

$$a = -7.86 \cdot 10^{-3} \quad [\mathrm{kHz}^{-2}] \tag{48a}$$

$$b = 9.79 \cdot 10^{-1} \quad [\mathrm{kHz}^{-1}] \tag{48b}$$

$$c = 5.69 \tag{48c}$$

are the coefficients of the parabolic function that fits the PA amplitude spectrum for frequencies up to 60 kHz. Assuming $\nu_S = 0$, one gets $\nu_E = \Delta\nu$ and the PA amplitude can be written as

$$V_{PA} \propto R \cdot \left(\frac{1}{3} a \cdot \Delta\nu^3 + \frac{1}{2} b \cdot \Delta\nu^2 + c \cdot \Delta\nu \right) \quad . \tag{49}$$

This general relation is useful to compare microphones with different responsivity R and bandwidth $\Delta\nu$ in view of their selection for obtaining maximum signal amplitudes. Obviously, $\Delta\nu$ is more important than R in this respect. This treatment holds true for most practical applications where external noise sources are independent of the microphone and exceed the microphone noise. Our predictions are verified by experimental studies as discussed below. It should be pointed out that the calculation does not assume fixed frequency boundaries $\nu_S = 0$ and $\nu_E = \Delta\nu$, but can instead be adapted to the actual case, e.g. to a microphone response reduced by a rectangular frequency filter. The 60 kHz upper limit is reasonable in practice because most commercial microphones operate within this frequency range. However, a general treatment again requires the consideration of the SNR. With the assumed flat frequency response between ν_S and ν_E, the microphone mean-square thermal-noise voltage $\overline{V_M}^2$ due to the thermal pressure fluctuations is described by Eq. (38) with $\Delta\nu = \nu_E - \nu_S$. In order to compare the suitability of microphones, we write $\overline{V_M}^2$ as

$$\overline{V_M}^2 = \alpha^2 \cdot N_M{}^2 \cdot (\nu_E - \nu_S) \quad , \tag{50}$$

where the introduced parameter N_M $[V/\sqrt{Hz}]$ represents the voltage noise per $\sqrt{Hz}$ usually given in the microphone specifications.

With equations (48), and (50) the SNR becomes

$$\frac{Signal}{Noise} \propto \frac{R \cdot (\nu_E - \nu_S)\left[c + \frac{1}{2}b(\nu_E + \nu_S) + \frac{1}{3}a(\nu_E{}^2 + \nu_E\nu_S + \nu_S{}^2)\right]}{\sqrt{\alpha^2 \cdot N_M{}^2 \cdot (\nu_E - \nu_S) + \overline{V_X}^2}} \quad . \tag{51}$$

This expression is suitable for the selection of microphones. With the coefficients given in equations (48a-c) the relation is valid for frequencies below 60 kHz and for beam radii below 0.5 mm. For $\overline{V_M} >> \overline{V_X}$, i.e. microphone voltage noise much higher than all other (external) noise sources, and considering for this case $\nu_S = 0$ and $\nu_E = \Delta\nu$, one gets

$$\frac{Signal}{Noise} \propto \frac{R \cdot \sqrt{\Delta\nu}\left[\frac{1}{3}a \cdot \Delta\nu^2 + \frac{1}{2}b \cdot \Delta\nu + c\right]}{N_M} \quad . \tag{52}$$

Using this equation the most appropriate microphone for the case $\overline{V}_M >> \overline{V}_X$ can be found by given microphone specifications R, N_M, and bandwidth $\Delta\nu$.

The following experimental part is aimed at verifying our theoretical considerations described above. We used amplifiers with large bandwidths suitable for a wide range of microphones without adapting the amplifier to the microphone frequency spectrum.

4.1.4 Experimental Setup

In order to compare the performance of different microphones, a new cylindrical cell with a length of 60 cm and a diameter of 50 cm has been built. The large dimensions allow to separate in time the directly generated acoustic pulse from its echoes caused by reflection at the cell wall, i.e. to obtain a microphone response that is independent from the influence of the cell geometry. The PA cell is filled with 100 ppm C_2H_4 buffered in synthetic air at gas pressure of 950 mbar. The CO_2 laser is tuned to the C_2H_4 absorption peak in the v_7 band. In order to avoid saturation, the laser beam crosses the cell coaxially. The laser radius is 2 mm and the fluence is reduced to 2 mJ/cm^2 using a Teflon foil. The microphones to be tested are placed in the middle of the cell at a distance of 6 cm from the CO_2 laser beam axis. At this distance, the generated cylindrical acoustic pulse reaches the surface of the microphones approximately as a plane wave even for the largest microphone with a diameter of 1 inch. In the following, we summarize the specifications of the selected condenser and electret microphones.

4.1.4.1 Condenser Microphones

Condenser microphones are generally accepted as the best microphone type for sound measurements. They provide the most satisfactory combination of all acoustical characteristics when the problem of precision measurements and high long-time stability is considered. The condenser microphones tested are B&K microphones (Brüel & Kjær, Denmark) provided with preamplifier and amplifier. A condenser microphone consists basically of a thin metal diaphragm and a rigid back plate constituting the electrodes of an air dielectric capacitor. A constant charge is applied to the capacitor by a DC voltage (the polarization voltage), the variations in capacitance caused by the varying sound pressure on the thin diaphragm are transformed into voltage variations. It becomes evident that responsivity and frequency response depend on many factors such as: a) stiffness of the diaphragm, b) mechanical damping of the diaphragm due to viscous resistance to air

movement between diaphragm and backplate, c) diaphragm mass, d) diaphragm surface, and e) interference and diffraction effects at frequencies where the microphone diameter is of the same order as the acoustic wavelength. In general, an increase of responsivity implies the reduction of frequency bandwidth $\Delta\nu$ and vice versa (Eq. (43)). In fact, a large diaphragm surface increases the responsivity by the resulting large capacitor, but reduces the bandwidth by its large diaphragm mass that lowers the vibration ability. In order to provide information about PA response from microphone with widely differing specifications, a high frequency but low responsivity microphone (model no. 4135), and a high responsivity microphone (model no. 4179) were chosen for the test. Their main features are summarized in Table 4.1.

Table 4.1. *Main specifications of the tested Brüel & Kjær microphones as indicated in the calibration report of the company. Note: The bandwidth reported is an approximation of frequency response specified in the chart in the Brüel & Kjær microphone description.*

Model	Diameter [inch]	Cartridge Capacitance [pF]	Open Circuit Responsivity [mV/Pa] at 250 Hz	Bandwidth [kHz]
4135	1/4	6.5	3.43	100
4179	1	38.3	100	12.5

A preamplifier stage (model B&K 2660) is placed in close proximity of the selected microphones. Such a configuration precludes loss of responsivity due to the stray capacitance of the connection. However, the coupling impedance of the preamplifier influences the responsivity of the microphone. In fact, when the microphone is loaded by the capacitance C_A [pF] of the preamplifier (0.3 pF for the 2660), the overall responsivity R [mV/Pa] of the microphone is given by

$$R = R_0 \cdot \frac{C_c}{C_c + C_A} \quad , \tag{53}$$

where R_0 is the open circuit responsivity of the microphone [mV/Pa] and C_c the microphone cartridge capacitance [pF], both given in Table 4.1. The preamplifier used, although suitable for almost all of the Brüel & Kjær microphones, offers a special adjustment design for the type 4179 that adapts the preamplifier to the microphone: the microphone resonance at approximately 7 kHz is suppressed in order to obtain a flat

frequency response until 12.5 kHz. In the present investigation, measurements with the 4179 have also been done without this special adjustment. Furthermore, an amplifier unit (model 5935) supplies the necessary power to the attached microphone-preamplifier assemblies, including microphone polarization voltages of 200 V.

4.1.4.2 Electret Microphones

Electret microphones are often miniature microphones widely used in hearing aids. The types tested here were two models by Knowles (EK-3133 and BT-1751) and one model by Sennheiser (KE 4-211-2). Their sizes are similar, the Knowles being a little smaller than the Sennheiser with a TO 18 transistor housing. Similar to the condenser microphones, electret microphones use a variable plate capacitor as an acoustic transducer, the front electrode being the microphone's diaphragm. As the diaphragm moves, the capacitance changes and a voltage proportional to the acoustic signal is produced.

The stationary back electrode (back plate) used in electret (pre-polarized) condensers is manufactured from a special synthetic material known as "electret". This material has a unique quality, being able to store a permanent electric charge; the charge is thus "frozen" in the electret material. It therefore requires no high external polarizing voltage and can be powered by low voltage batteries. The counter electrode is manufactured from a thin gossamer foil, which is made conductive by depositing a thin layer of gold by a coating process. Such an ultra-light diaphragm provides good transient response, high responsivity at low sound pressure levels and ensures highly accurate sound reproduction with minimal distortion.

Table 4.2. *Main specifications of the electret condenser microphones. Note: The bandwidth reported is an approximation of frequency response specified in microphone data sheets.*

Model	Responsivity [mV/Pa] at 1 kHz	Bandwidth [kHz]
Sennheiser KE 4-211-2	10	20
Knowles EK-3133	20	10
Knowles BT-1751	10	10

The Sennheiser microphone in particular is characterized by a very flat frequency response. Furthermore, a field-effect transistor (FET), integrated in the microphone capsule, adapts the high impedance of the condenser for further connections. A self-made amplifier stage with a bandwidth of 50 kHz based on a low noise operational amplifier (Burr-Brown INA103), amplifies the microphone signal by a factor of 100. The main features of the microphone are summarized above in Table 4.2.

4.1.5 Measurements and Discussion

In our investigations the signals recorded with the B&K microphones were amplified by 20 dB with the 2660 preamplifier stage and by another 10 dB with the 5935 amplifier unit. However, all data reported for B&K microphones are multiplied by the factor 3.16 corresponding to a total amplification of 100 (40 dB) as it was done in the studies with the electret microphones. The PA signal averaged over 30 shots measured with the large bandwidth 1/4 inch type B&K 4135 microphone is presented in Fig. 4.5 below.

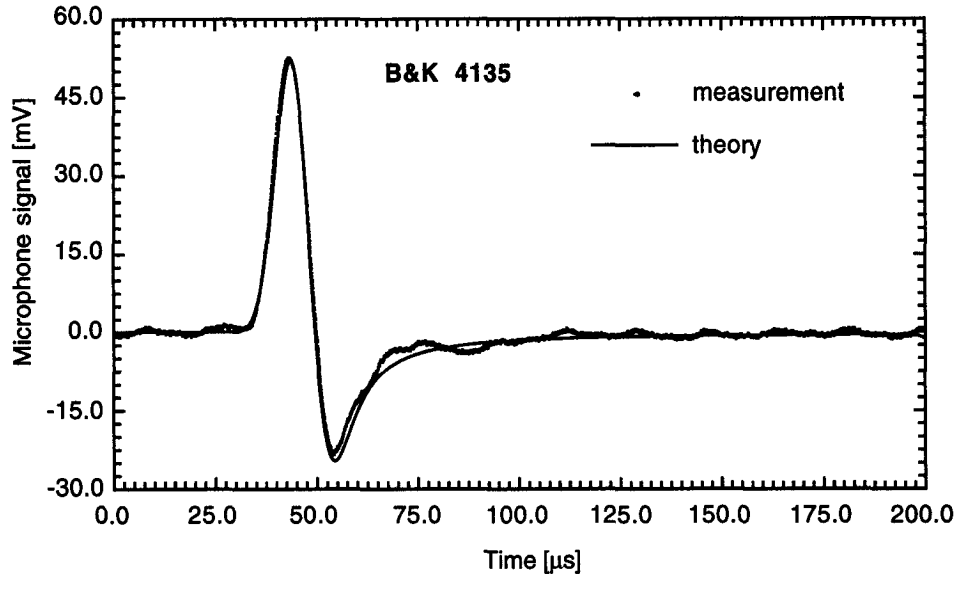

Figure 4.5. *Measured and calculated PA pulse generated in 100 ppm C_2H_4 buffered in synthetic air at 950 mbar for a beam radius of 2 mm. The measurement was recorded with the B&K 4135 microphone.*

The peak voltage is 52.55 mV. The calculated curve is derived from the density equation (33). A laser beam radius of 2 mm, as estimated by Gaussian beam propagation, and a relaxation time $\tau_{relax} = 2.4\ \mu s$ as obtained from independent probe beam deflection experiments (chapter 5) has been used. The calculated amplitude is fitted to the measured

one. As demonstrated in Fig. 4.5 the B&K 4135 microphone is able to resolve the temporal shape of the acoustic wave. The Fourier transform of the measured microphone signal is also in good agreement with the calculated spectrum as shown in Fig. 4.6. Since frequencies above 100 kHz are beyond the microphone frequency spectrum, the measured spectrum drops below the computed spectrum in the same range.

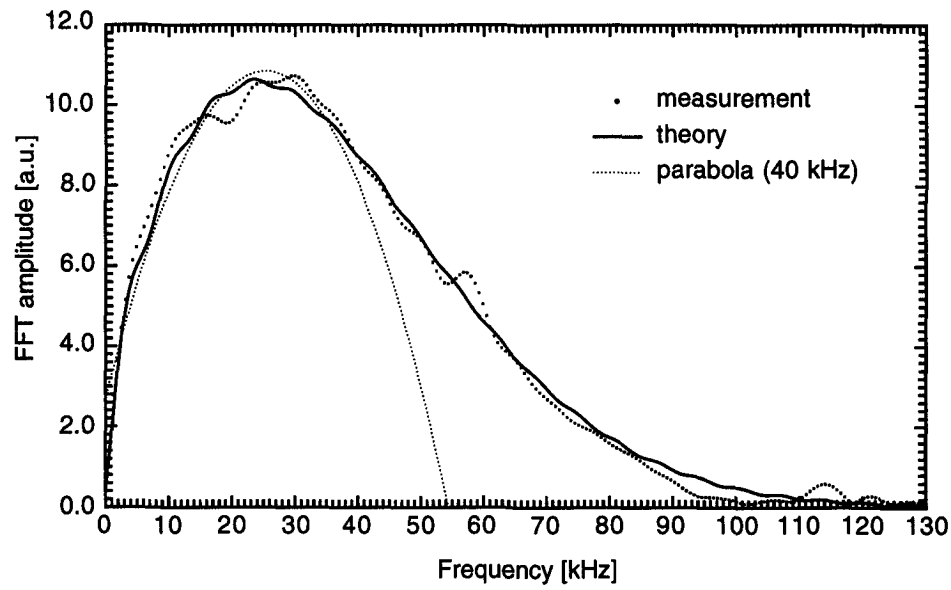

Figure 4.6. *FFT amplitude of the signals described in the previous figure 4.5. The parabola (dotted line) approximates the theoretical signal spectrum until 40 kHz.*

The parabolic function which approximates the frequency spectrum of the PA amplitude up to a certain frequency is indicated as dotted line in Fig. 4.6. Contrary to what was done in the theoretical part, the coefficients introduced above in Eq. (49) are adapted to the actual experimental conditions for a larger beam radius (2 mm instead of 0.5 mm). One gets for a parabolic fit up to 40 kHz:

$$a = -1.27 \cdot 10^{-2} \quad [\mathrm{kHz}^{-2}] \tag{54a}$$

$$b = 0.645 \quad [\mathrm{kHz}^{-1}] \tag{54b}$$

$$c = 2.69 \quad . \tag{54c}$$

These data are substituted into Eq. (49) to verify the measured data with the theoretical approximation of the PA amplitude. Two measurements are presented for the 1 inch high-responsivity B&K 4179 microphone. The first measurement represented by the solid line in Fig. 4.7 was performed with the preamplifier tailored for a flat frequency response of

the microphone for frequencies up to 12.5 kHz. The second signal, indicated by the dotted line, was obtained with the normal preamplifier configuration. The PA peak amplitudes for all B&K microphones are listed in Table 4.3. Figure 4.7 implies that different preamplifier configurations result in rather different signal shapes and amplitudes.

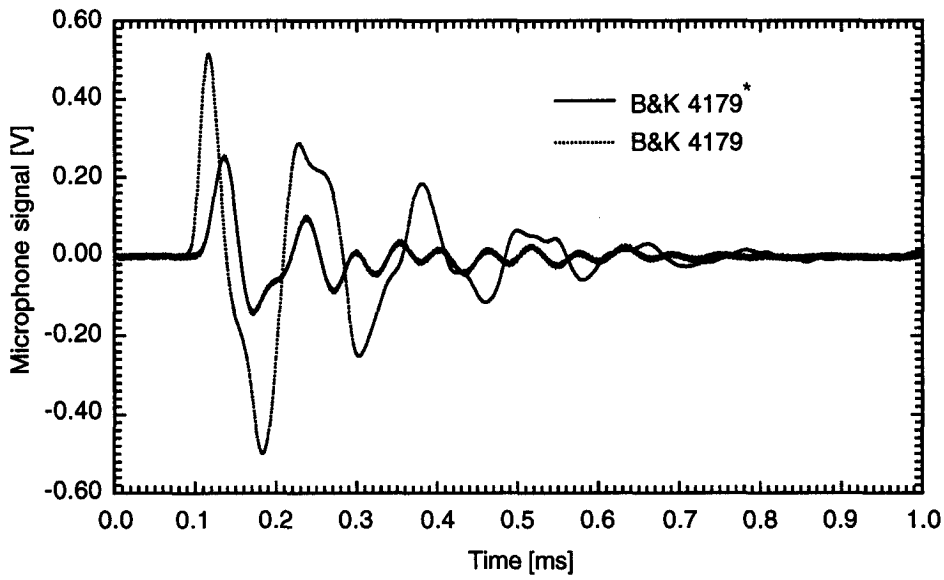

Figure 4.7. *PA signal measured with the B&K 4179 microphone with different preamplifier configurations. Adjustment for flat frequency response (B&K 4179*) up to 12.5 kHz (solid line), normal configuration (dotted line).*

The FFT signal analyses are depicted in Fig. 4.8 where the deviations are again evident. The high peak amplitude appearing at ca. 7.3 kHz is caused by a resonance vibration of the microphone membrane.

Table 4.3. *PA amplitude measured with the Brüel & Kjær microphones. The asterisk indicates the measurement obtained with the preamplifier configuration tailored for a flat frequency response up to 12.5 kHz.*

Brüel & Kjær Microphone	Peak amplitude [mV]
4135	52.55
4179*	251.9
4179	515.3

This high amplitude explains the higher PA peak measured with the standard preamplifier configuration. It should be remarked that the specified responsivity of 100 mV/ Pa over the specified frequency range is not valid in this case. The responsivity of the microphone-preamplifier system depends strongly on the frequency and the theoretical estimation of the PA pulse amplitude with the proposed theoretical model is thus not feasible.

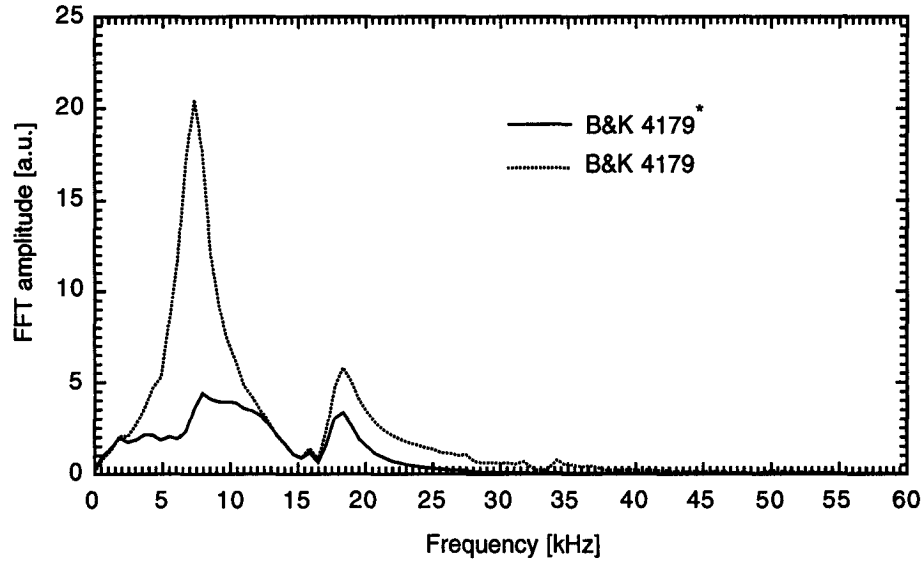

Figure 4.8. *FFT of the measurement obtained with the B&K 4179 microphone. The solid line is obtained using the special preamplifier configuration with flat frequency response up to 12.5 kHz (B&K 4179*). The dotted line is obtained using the normal preamplifier. The microphone resonance at 7.3 kHz is clearly pronounced in the normal configuration.*

As Fig. 4.8 implies, the resonance peak in the measurement recorded with the special preamplifier configuration is strongly suppressed but still visible. The specified flat frequency response is presumably achieved for measurements with a sinusoidal sound wave. In those cases, the frequency dependent phase of the preamplifier does not influence the signal amplitude of the measurement. Furthermore, the signal spectra for both preamplifier configurations exhibit a second unexpected peak near 18 kHz probably due to the second harmonic resonance. This extends the frequency response somewhat, though not continuously, to higher frequencies than expected. We estimate the overall frequency bandwidth $\Delta\nu$ to about 15 kHz and use this value for the theoretical estimation of the amplitude, i.e. the specified bandwidth is not a priori the value used for the calculation. This is also true for the electret microphones. An estimation of $\Delta\nu$ is made in each case separately. The measurements with the electret microphones are illustrated in Fig. 4.9.

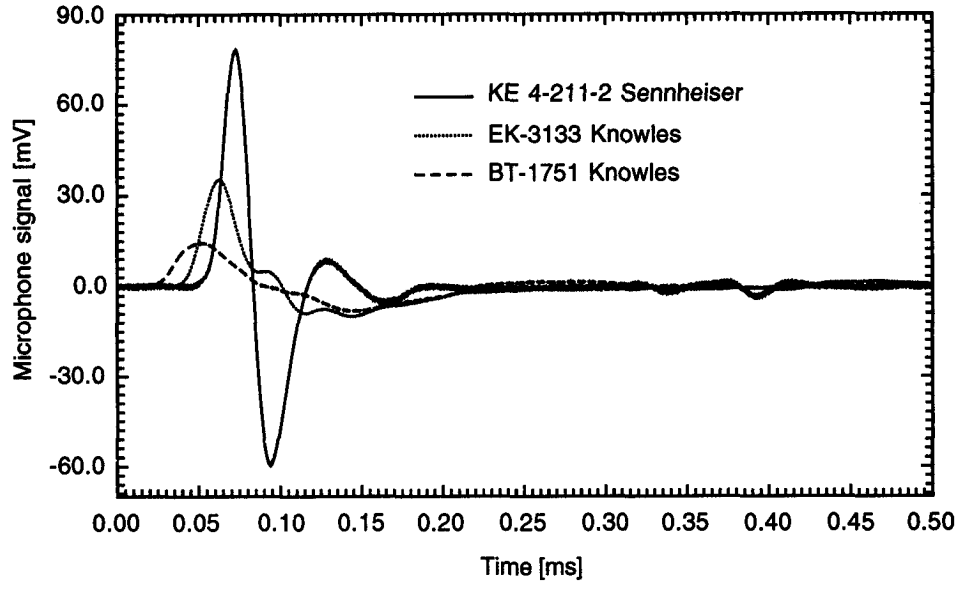

Figure 4.9. *PA pulses measured with the electret microphones*

From these measurements we deduce the following peak amplitudes:

Table 4.4. *PA amplitudes measured with electret microphones.*

Microphone	Peak amplitude [mV]
KE 4-211-2 Sennheiser	78.0
EK-3133 Knowles	35.3
BT-1751 Knowles	14.4

The comparison between the measurements obtained with the Knowles EK-3133 and the Sennheiser microphone with identical responsivity but different bandwidth, confirms the predicted increase in signal amplitude at larger frequency bandwidth (Eq. (49)). Furthermore, the stronger dependence of the overall responsivity on the bandwidth rather than on the microphone responsivity is demonstrated when comparing the results obtained with the Knowles EK-3133 and the Sennheiser microphone. Although the Sennheiser microphone has only half responsivity compared to the Knowles, a higher signal is obtained thanks to the larger bandwidth of the former. The FFT spectra of the measurements are shown in Fig. 4.10. It is evident that the application range of the Sennheiser microphone is significantly wider than the estimated 20 kHz. Although

frequencies above 20 kHz are strongly damped we assume an average microphone bandwidth of 28 kHz for the theoretical analysis.

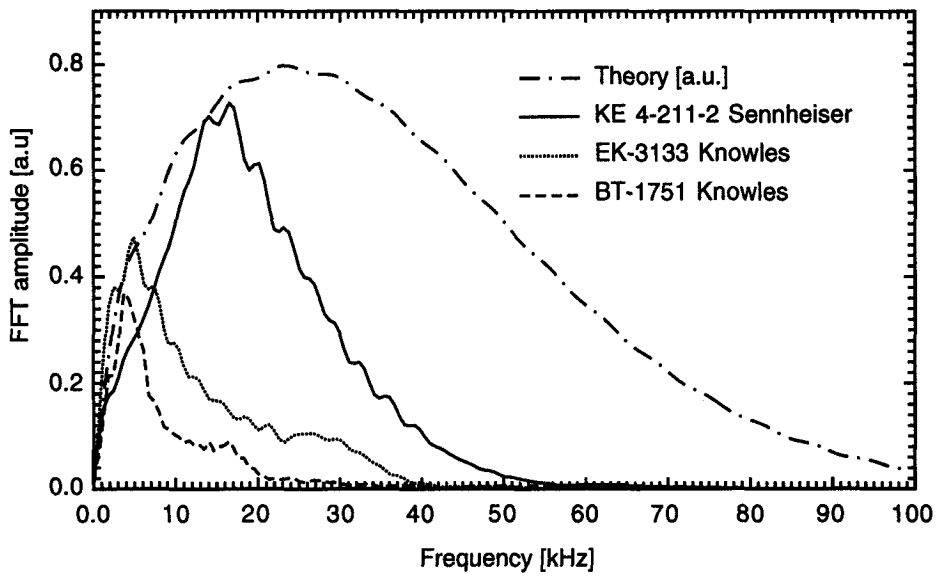

Figure 4.10. *FFT spectra of the PA pulse recorded with the electret microphones. The dashed-dotted line describes the involved frequency spectrum in the PA pulses calculated from the theoretical pulse shape.*

For the two Knowles microphones the frequency bandwidth is close to the specified 10 kHz although the bandwidth appears somewhat broader for the EK-3133 type. We thus assumed the specified bandwidth of 10 kHz and 11 kHz for the BT-1751 and the EK-3133 microphones, respectively.

4.1.6 Comparison Between Measured and Expected Amplitude of Photoacoustic Signals

On the basis of the coefficients of the parabolic fit for the FFT spectrum of the acoustic pulse given in equations (54a, b, c) and the assumed bandwidths $\Delta\nu$ of the different microphones as specified above, the theoretical PA amplitudes are calculated with equation (49). The results are summarized in Table 4.5. The measured and theoretical PA amplitudes are normalized with respect to the amplitude of the BT-1751 microphone in each case. Although good agreement between theory and measurement is obtained, the important role of a precise knowledge of $\Delta\nu$ for the accurate prediction of PA amplitudes should be pointed out. Since in reality, the frequency response deviates considerably from the assumed rectangular function, only a rough estimation is usually possible on the basis

of data sheets or prior own test measurements. Although $\Delta\nu$ is more important than R as implied by Eq. (49), the responsivity should not be underrated as it is demonstrated in Table 4.5.

Table 4.5. *Comparison between measured and calculated PA pulse amplitude. The peak amplitudes are normalized to the corresponding PA amplitude of the BT-1751 microphone of the respective column.*

Microphone	Responsivity R [mV/Pa]	Assumed bandwidth $\Delta\nu$ [kHz]	Normalised measured peak amplitude	Normalised theoretical peak amplitude
B&K 4179*	100	15	17.5	18
KE 4-211-2	10	28	5.4	4.3
EK-3133	20	11	2.5	2.3
BT-1751	10	10	1	1

** B&K 4179 microphone with specially adapted preamplifier configuration.*

The highest peak amplitude is obtained with the B&K microphone with the highest R but only second largest $\Delta\nu$. Hence, for the situation which is encountered in most practical applications where external noise sources exceed the microphone noise ($\overline{V}_M << \overline{V}_X$) and assuming constant external noise in all our measurements, the B&K microphone is the most appropriate of the microphones tested. However, it should be emphasized that besides the important physical properties, other factors like size and price may also play an important role concerning a final microphone selection. In the opposite case ($\overline{V}_M >> \overline{V}_X$), Eq. (52) should be applied for the evaluation. This case requires the knowledge of microphone noise data which are often difficult to obtain because they are either not specified or defined for a specific frequency range only or given in dB(A), i.e. as A-weighted noise level which refers to the noise level weighted to the human hearing capacity (Kinsler et al. [1982]).

4.1.7 Pressure Dependent Microphone Responsivity

Microphones are generally built to work in normal atmospheric conditions where they exhibit maximum responsivity. At a different pressure, or in environments other than air, the density ρ and/or the compressibility κ change the sound wave characteristic impedance $Z_s = \sqrt{\rho/\kappa}$. Therefore the acoustic energy transmitted to the microphone membrane also changes and hence influences the responsivity. In Fig. 4.11 (filled points) we show a PA measurement performed with a Knowles microphone (model EK-3133) that evidences the variation of the responsivity with gas pressure. The observed pressure dependence corresponds to the transmission function of an acoustic wave propagating from one medium to another with different acoustic impedance. The two media in this case are the gas and the microphone membrane.

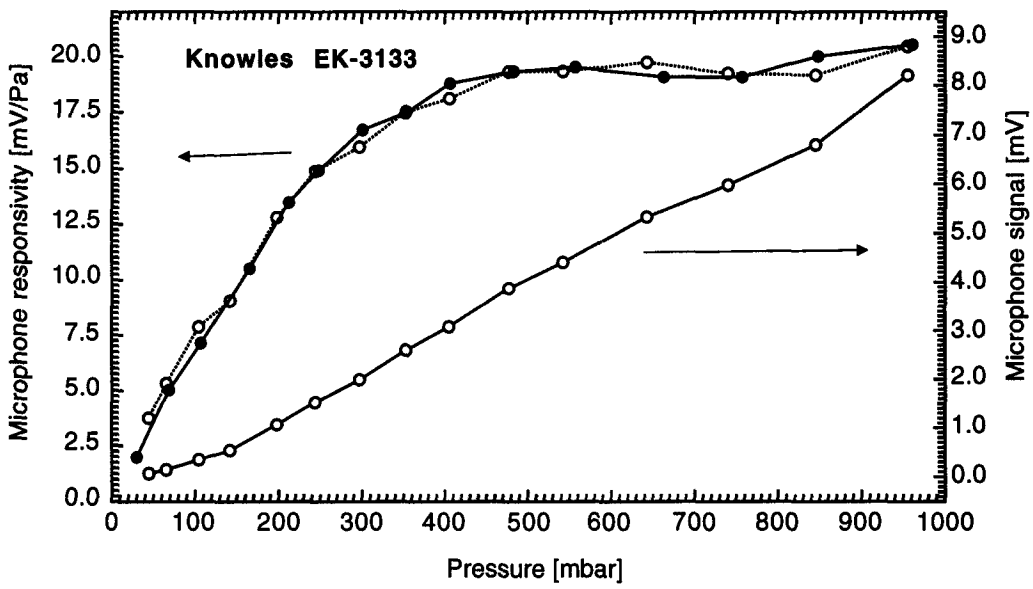

Figure 4.11. *Responsivity and PA signal of a Knowles microphone (model EK-3133) in function of total pressure p. Filled points: direct measurement of responsivity for a gas mixture containing 0.036 mbar C_2H_3Cl buffered in N_2 (mixture with constant amount of C_2H_3Cl). Lower open points: microphone signal for a gas mixture containing 140 ppm C_2H_3Cl buffered in N_2 (constant relative concentration of C_2H_3Cl). Upper open points: indirect measurement of responsivity obtained by dividing the microphone signal (represented by the lower open points) with the pressure p. The lines represent a visual guide.*

These measurements were performed under particular experimental conditions that induce PA pulses with identical temporal shapes and amplitudes within the entire pressure range between 30 and 950 mbar in order to obtain a true pressure dependence of the microphone responsivity not influenced by any other factors. We have thus selected a gas

mixture with a constant amount of vinyl-chloride C_2H_3Cl (0.036 mbar), buffered in N_2, a laser beam radius of about 2 mm, a laser wavelength of 942.172 cm^{-1} which corresponds to the wavelength of the absorption peak of C_2H_3Cl (see Fig. 5.19), and a constant laser pulse energy of 30 mJ. These conditions guarantee both, identical temporal shapes and peak amplitudes within the entire pressure range. The reason for this is that the occurring fast relaxation times of C_2H_3Cl in the investigated pressure range (see chapter 5) in combination with the chosen laser beam radius, generate PA pulses within the convergent regime (see section 4.1.1 and 5.4). Furthermore, the saturation of the C_2H_3Cl molecules by the selected laser fluence and wavelength eliminates the problem of different molecular absorptivity at different pressures. It can thus be assumed that a constant number of excited C_2H_3Cl molecules inside the irradiated region contributes to the generation of the PA pulse. Under such conditions the spatial temperature distribution in the gas mixture has a constant shape at all gas pressures but its amplitude is inversely proportional to the total gas pressure. Considering that the induced pressure variation is proportional to the total pressure and to the temperature variation, identical PA pulse shapes and peak amplitudes are indeed obtained under the described experimental conditions. The observed pressure dependence of the PA signal amplitude is therefore caused exclusively by the microphone responsivity. Other microphone models may exhibit a slightly different behaviour than the one plotted in Fig. 4.11 due to deviating membrane characteristics. The open points at the bottom of Fig. 4.11 represent measurements with constant relative concentration (140 ppm) of C_2H_3Cl buffered in N_2, performed under the same experimental conditions as the filled points were recorded. The division of these measured data by the total gas pressure yields the open upper points in Fig. 4.11. This represents another measurement of the microphone responsivity.

The reduction of the responsivity and consequently a reduction in sensitivity is a rather general consequence of measurements at lower pressure. However, it should be kept in mind that under other experimental conditions, e.g. other gas mixtures and concentrations with other relaxation rates, no absorption saturation, laser not tuned to the wavelength of the absorption peak, the situation can be drastically different. In this case the pressure dependence of the PA amplitude is influenced by additional factors than just the microphone responsivity and each case needs special consideration before quantitative statements can be made. In contrast to the loss of sensitivity, the advantage of PA investigations performed at a reduced pressure is often an enhanced detection selectivity due to less pronounced pressure broadening of the absorption lines. As example, a compromise between selectivity and sensitivity was chosen to analyze a mixture of six CO_2 isotopes to be discussed in the following section 4.2. At a pressure of 100 mbar a strong overlap of the absorption lines was avoided while maintaining a sufficient SNR.

4.2 Analysis of Isotopic CO_2 Mixture

Carbon dioxide (CO_2) is one of the most important gases in the terrestrial atmosphere. With its present average concentration of 350 of parts in 10^6 (350 ppm), it represents a major contributor to the greenhouse effect. The magnitude of its bipolar coefficients contributes to the well-known opacity windows in the terrestrial atmosphere. Also in planetary atmospheres, CO_2 is important. As example, it is the primary absorber in the atmospheres of Mars and Venus. Furthermore, CO_2 plays an important role in many biological and chemical processes and also in astronomical and physical research. CO_2 isotopes are employed in various fields: age determination, biological, medical and climatological research using traces of ^{13}C atoms are prominent examples.

Detection schemes for the various CO_2 isotopes that provide sufficient accuracy and sensitivity, wide dynamic range of determined concentrations from grams/m^3 (in agrochemical research) to micrograms/m^3 (in biochemical experiments), simple handling and capability to analyze multicomponent samples with one device are therefore required. Common methods are mass spectrometry and emission spectroscopy. The former offers high accuracy but is usually limited to the measurement of masses 44, 45 and 46. It is thus not readily applicable to isotopes containing ^{14}C or ^{17}O due to overlapping of the masses 46 and 48. On the other hand, emission spectroscopy, eventually in combination with isotopic dilution (Funtov et al. [1992]), fulfils all the requirements stated above. However, the analytical result can be influenced by possible distortions of the sample composition in the discharge and by wall effects. In this work we focus on the photoacoustic (PA) spectroscopic method that offers a simple and accurate analysis. We present new studies on the analysis of an isotopic mixture of CO_2 containing six different isotopes. In contrast to mass spectrometry and emission spectroscopy, PA spectroscopy also allows the simultaneous determination of absorption cross sections at the same time.

4.2.1 Photoacoustic Investigations

The PA cell presented in chapter 3 (Fig. 3.3) was filled with an isotopic mixture supplied by the Institute of Physics of the St. Petersburg University (St. Petersburg, Russia) that contained unknown amounts of the isotopes $^{12}C^{16}O_2$ (referred to as 626), $^{12}C^{18}O_2$ (828), $^{13}C^{16}O_2$ (636), $^{13}C^{18}O_2$ (838), $^{16}O^{12}C^{18}O$ (628), and $^{16}O^{13}C^{18}O$ (638). The total gas pressure was 100 mbar which represents a compromise between PA signals

with large SNR on the one hand, and too strong overlapping of absorption lines by pressure broadening on the other hand. The PA spectrum was measured throughout the entire range of continuous laser tunability in the 10P, 10R and 9R branches. Part of the measurement in the 10P branch is displayed in Fig. 4.12. It happens that all six isotopes show absorption lines in this branch of the $^{12}C^{16}O_2$ laser emission.

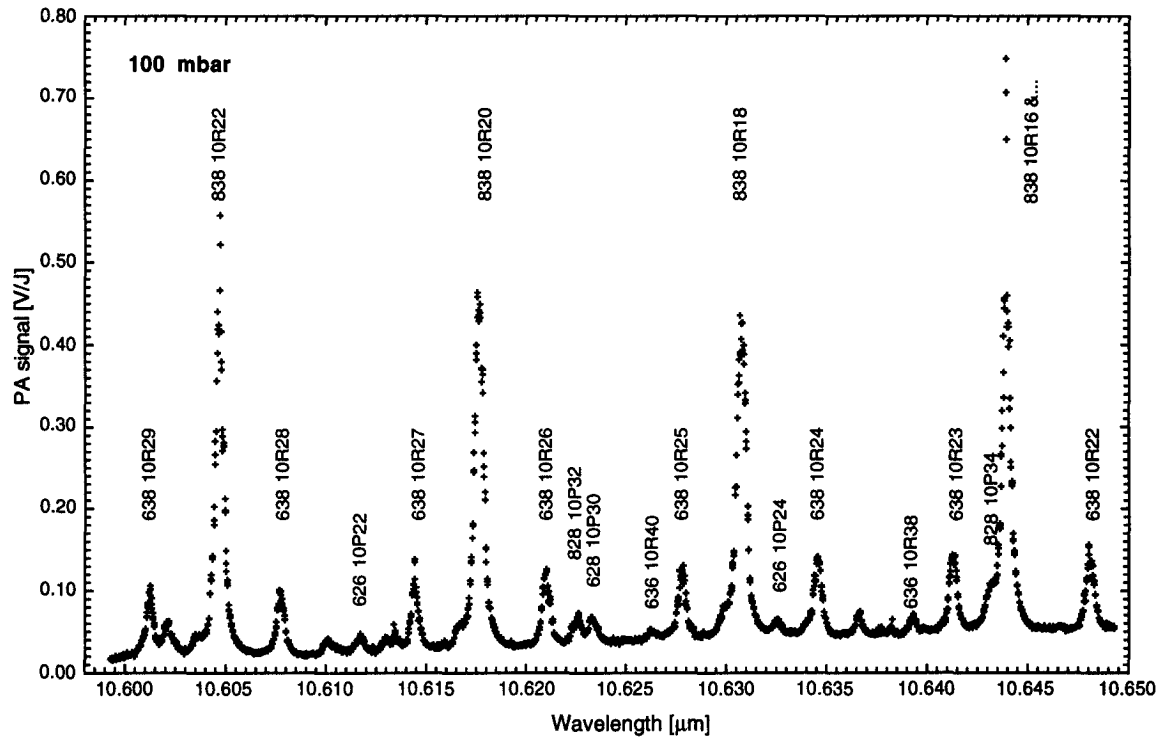

Figure 4.12. *Part of the PA spectrum of the isotopic mixture recorded in the $^{12}C^{16}O_2$ 10P laser branch at 100 mbar total pressure and room temperature. The PA signals given in [V/J] are normalized to the laser pulse energy. The 10R(16) line of the 838 isotope is not pure but overlapped by absorption lines of other isotopes.*

As shown in the Fig. 4.12, the various isotopic absorption lines could be identified and exhibit a good agreement with theoretically predicted absorption wavelengths (Witteman [1987]).

The experimental result obtained by adding a selected amount of the common 626 isotope to the mixture, confirms the expected change in the spectrum as Fig. 4.13 demonstrates. Two PA spectra, both taken at 100 mbar total pressure are shown. The spectrum of the unchanged isotopic mixture (indicated by open circles) is compared with one obtained by adding 17 % of the 626 isotope to the mixture (indicated by dots).

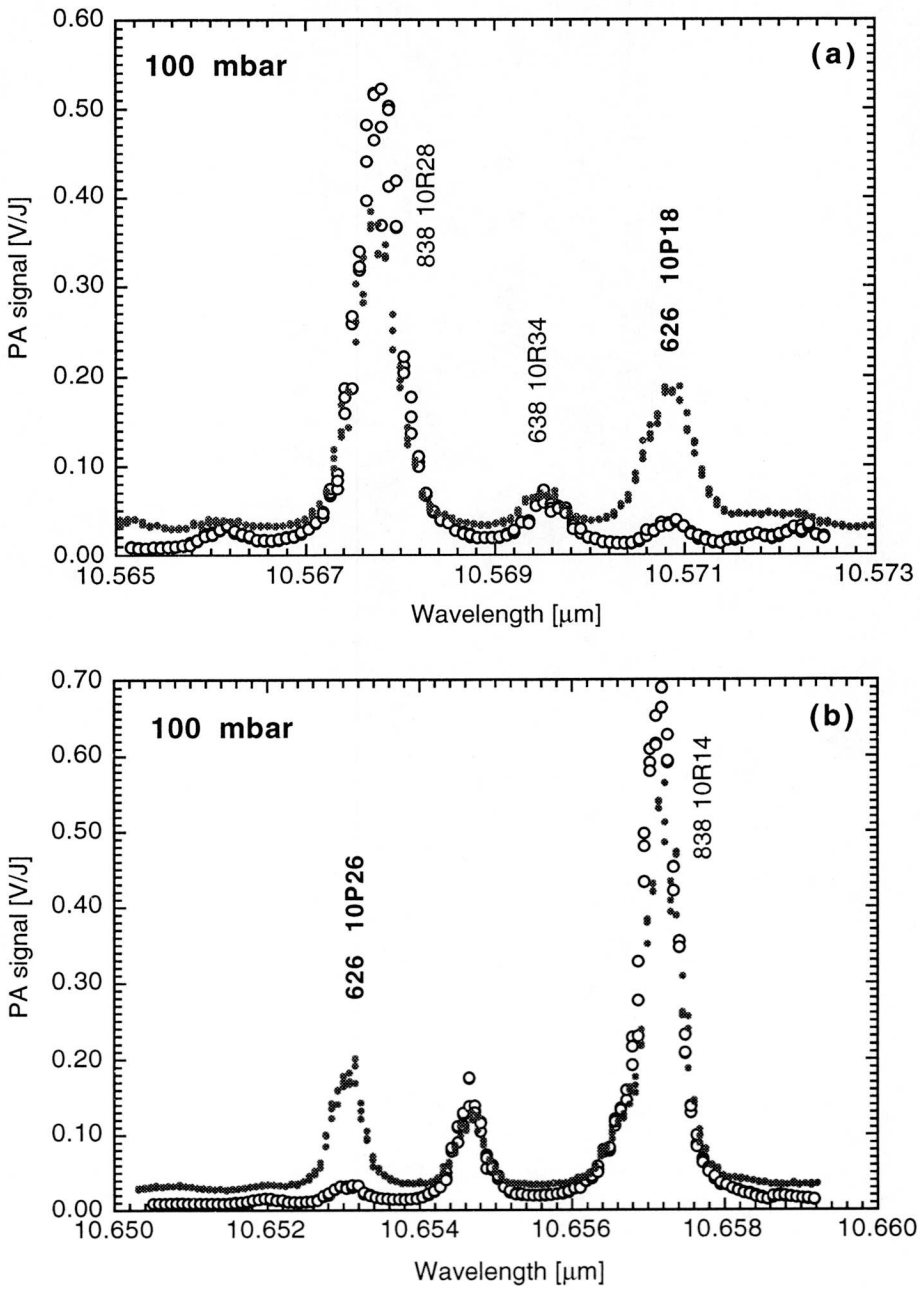

Figure 4.13. *Comparison of the PA spectra at a fixed pressure of 100 mbar between the original isotopic mixture (open circles) and the isotopic mixture buffered with 17 % of the 626 isotope (dots), illustrated for the 10P(18) CO_2 laser transition (Fig. 4.13a) and for the 10P(26) CO_2 laser transition (Fig. 4.13b).*

Figure 4.13a shows the change for the 10P(18) line and Fig. 4.13b the change for the 10P(26) absorption line of the 626 isotope. The positions of the absorption lines are in excellent agreement with literature data (Witteman [1987], Rothman et al. [1992/a]) and the quantitative changes of the amplitudes are as expected.

4.2.2 Results and Discussion

4.2.2.1 Isotopic Concentrations

The spectrum of a multicomponent gas mixture is the result of a linear superposition of the spectra of the individual compounds. The linear relationship between the signal amplitudes and the concentrations of the individual compounds allows to fit the spectrum by a linear superposition of the single spectra, and hence to determine the concentrations. However, this simple method requires quantitative cross sections of all the components. Our mixture contained three CO_2 isotopes (626, 628, and 636) with known absorption spectra listed in the Hitran database (Rothman et al. [1992/a-b]), and three other CO_2 isotopes (828, 838, and 638) for which to the best of our knowledge no spectral data are reported in the 9-11 μm range. However since the ratios of the total ^{12}C to ^{13}C concentration ($\Sigma^{12}C/\Sigma^{13}C$) and of the ^{16}O-to-^{18}O concentrations ($\Sigma^{16}O/\Sigma^{18}O$) were known, the determination of the individual isotopic concentrations was still possible. We performed a two-step approach: initially the concentrations of the 626, 636 and 628 isotopes were determined on the basis of our PA measurement and the known absorption cross sections. Then, these data were then used in combination with the known ratios mentioned above to infer the remaining three isotopic concentrations. The concentrations of the 626, 636 and 628 isotopes were derived by taking only selected parts of the spectrum in which no or only negligible overlapping of the individual absorption lines occurs. PA spectra in the 9R branch where well separated absorption lines of only three isotopes (626, 628 and 828) are present, were used to determine the concentrations of 626 and 628. Figure 4.14 depicts a part of the spectrum in the 9R branch and illustrates the method for the determination of the 626 isotope concentration. The arrows indicate two absorption lines (9R(22) and 9R(20) of the 626 isotope) that are taken from the measured spectrum on the top and transferred to a spectrum below that is then used to obtain the concentrations by a standard fitting procedure. Depending on their absorption strength and closeness to adjacent lines, the latter are also taken into account because they influence the peak height and shape of the considered lines of the 626 isotope. This method is appropriate for the determination of other isotopes with a known absorption cross section $\sigma(\lambda)$, i.e. for the 636, 626, and 628 isotopes. The determination of the concentrations of the remaining isotopes 828, 838, and 638 can consecutively be performed in a second step by using the known $\Sigma^{12}C/\Sigma^{13}C$ and $\Sigma^{16}O/\Sigma^{18}O$ ratios and under the assumption that the mixture contains only the six isotopes mentioned.

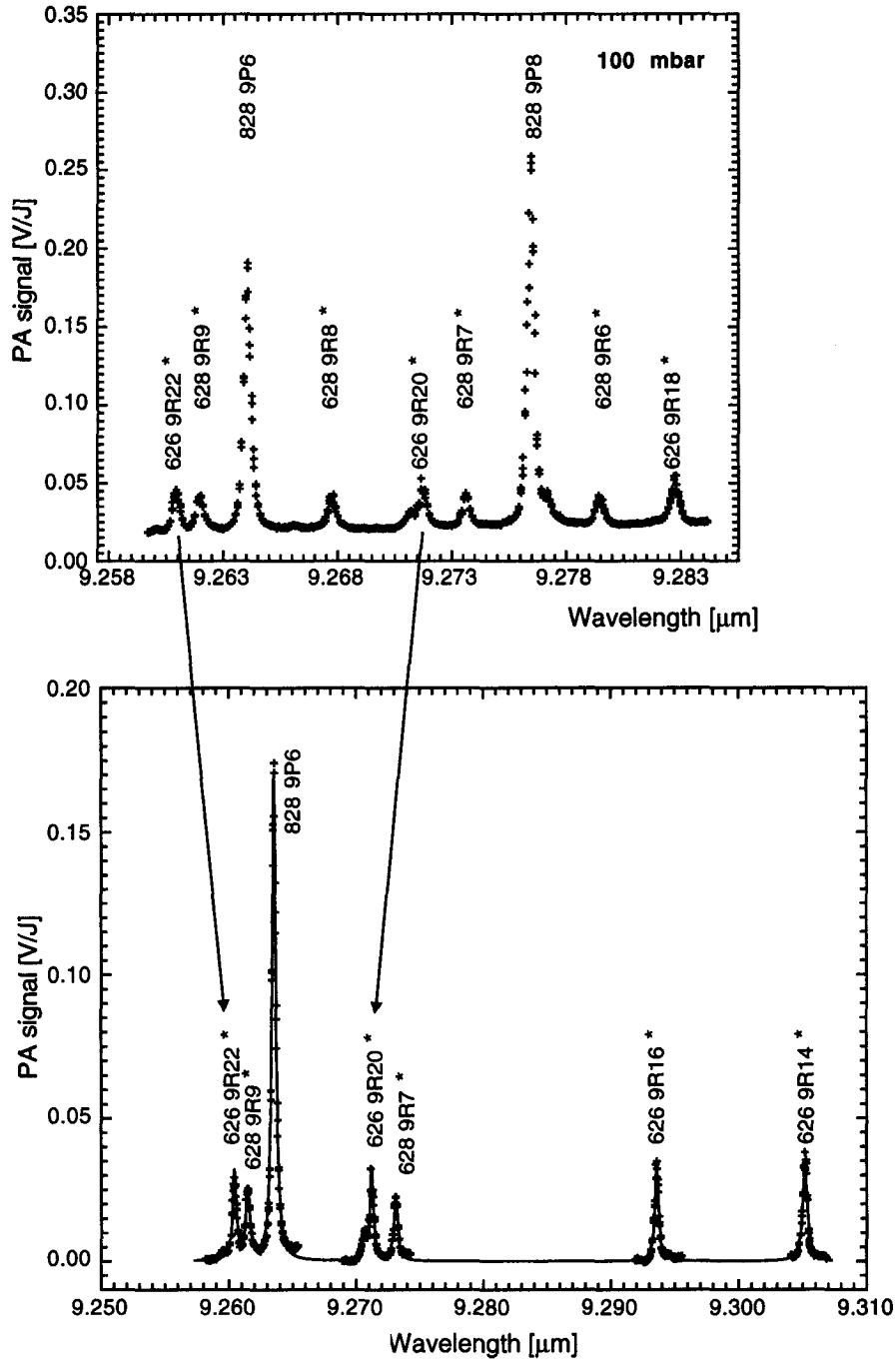

Figure 4.14. *The procedure for obtaining the concentration of individual isotopes with known absorption cross section is demonstrated for the $^{12}C^{16}O_2$ (626) isotope. Only absorption lines of the 626, 628 and 828 isotopes are present in the 9R laser branch. From these, only the absorption data of the 626 and 628 isotopes (marked by asterisks) are listed in the Hitran database (Rothman et al. [1992/a]). Selected parts of the upper spectrum recorded in the 9R branch are used to create a new spectrum (bottom). From this the concentration is derived by a standard fitting method.*

Using the normalized concentrations n_i (where i denotes the isotope), we obtain for the composition of the mixture

$$n_{626} + n_{628} + n_{828} + n_{636} + n_{638} + n_{838} = 1 \tag{55}$$

In our case, the fraction of residual gases in the mixture was known to be less that 1.5 % so that equation (55) represents a good approximation.
The ratio $\Sigma^{16}O/\Sigma^{18}O$ that holds for the O atoms yields

$$\frac{2n_{626} + 2n_{636} + n_{628} + n_{638}}{2n_{828} + 2n_{838} + n_{628} + n_{638}} = 0.228 \tag{56}$$

The factor 2 takes into account that certain isotopes contain two of the considered oxygen isotopes. The ratio $\Sigma^{12}C/\Sigma^{13}C$ that holds for the C isotope is given by

$$\frac{n_{626} + n_{628} + n_{828}}{n_{636} + n_{638} + n_{838}} = 0.159 \tag{57}$$

Table 4.6. *Isotopic composition for a total pressure of 100 mbar*

Component	Partial pressure [mbar]	Precision
$^{12}C^{16}O_2$	2.1	± 1.8 %
$^{16}O^{12}C^{18}O$	4.3	± 1.6 %
$^{13}C^{16}O_2$	1.7	± 11 %
$^{12}C^{18}O_2$	7.3	± 1.5 %
$^{13}C^{18}O_2$	59.3	± 0.5 %
$^{16}O^{13}C^{18}O$	25.3	± 2.3 %

Using the concentrations of the three isotopes derived in the first step, we can solve the equation system (55) to (57) and obtain the concentrations n_{828}, n_{838} and n_{638} for the remaining isotopes. The final results for all the isotopes, normalized to a total pressure of 100 mbar, are listed in Table 4.6. The relatively low precision of the 636 concentration is

caused by both its low concentration and the small absorption cross section at the selected lines used for the fit. In principle, stronger lines would be available but are superimposed by strong lines of other isotopes.

4.2.2.2 Absorption Cross Sections

Furthermore, emphasis was put on the determination of the unknown absorption cross sections of the 828, 838 and 638 isotopes. The relation that connects the isotopic concentration n_i to the recorded PA signal S_i, normalized by the laser pulse energy, is given by (Rosengren [1975])

$$S_i(\lambda) = n_i \cdot N_{total} \cdot \sigma_i(\lambda) \cdot C \tag{58}$$

where N_{total} denotes the total molecular number density, $\sigma_i(\lambda)$ the wavelength-dependent absorption cross section of isotope i, and C the cell constant. We determined the constant C prior to our isotopic studies by taking PA spectra of common CO_2 at a partial pressure of 100 mbar at selected laser transitions. The corresponding absolute absorption cross sections were taken from Hitran data (Rothman et al. [1992/a]). A detailed analysis of the measured spectra shows that many of the absorption lines of the 828, 838 and 638 isotopes are either weak or overlap with other lines. The determination of $\sigma_i(\lambda)$ was therefore performed with well defined absorption lines that are predominant in the 9R and in the 10P laser branches. The results with the statistical errors are reported in Tables 4.7 and 4.8. To our knowledge these data are the first absorption data reported for these molecules.

Table 4.7. *Absorption cross sections of $^{12}C^{18}O_2$ within the 9R branch of the $^{12}C^{16}O_2$ laser*

Isotope	Molecular transition	Wavenumber [cm^{-1}]	Absorption cross section σ [10^{-22} cm^2]
828	9P(10)	1076.5738	69.68 ± 2.09
	9P(12)	1075.0859	69.66 ± 2.09
	9P(14)	1073.5788	69.20 ± 2.08

Table 4.8. *Absorption cross sections of three CO_2 isotopes within the 10P branch of the $^{12}C^{16}O_2$ laser.*

Isotope	Molecular transition	Wavenumber [cm^{-1}]	Absorption cross section σ [10^{-22} cm^2]
828	10P(22)	950.1401	12.76 ± 1.15
	10P(26)	946.7378	10.42 ± 0.62
	10P(36)	937.7643	9.82 ± 0.79
838	10R(12)	937.1031	8.17 ± 0.33
	10R(20)	941.8623	10.53 ± 0.42
	10R(22)	942.9947	10.86 ± 0.43
	10R(26)	945.1901	10.69 ± 0.42
	10R(30)	947.2924	8.54 ± 0.34
638	10R(16)	935.3982	6.38 ± 0.51
	10R(17)	936.0388	6.84 ± 0.55
	10R(22)	939.1607	5.21 ± 0.37
	10R(26)	941.5607	5.04 ± 0.35
	10R(30)	943.8732	4.15 ± 0.50

Chapter 5

Photothermal Beam Deflection Investigations

The photothermal beam deflection (PTBD) technique has the great advantage of being a purely optical, non-contact scheme. It is therefore also applicable to aggressive gases or for investigations performed under extreme experimental conditions like high temperature. Furthermore, the good time resolution enables the study of fast gas density variations. This section is aimed at a detailed investigation of PTBD signals in gases under various experimental conditions with respect to the determination of molecular relaxation rates and thermal conductivity.

In this work the density fluctuation caused by the transient heat production after laser pulse excitation, and described mathematically in the theoretical part (chapter 2), is monitored with the PTBD technique. The PTBD experimental arrangement, presented in chapter 3, is applied and initial results obtained for the excitation of the ν_3 mode of SF_6 performed at different gas pressures, pump beam diameters and distances between pump and probe beams demonstrate the potential of this scheme. Measurements on C_2H_4 and SF_6 buffered in Ar or He/Ar mixtures yield excellent agreement with our theoretical description based on a three-species model. Furthermore, we developed a criterion for optimum experimental regimes under which data can be derived with a given accuracy. In particular, accuracy considerations for the determination of molecular relaxation rates and optimum distances between pump and probe laser beams are discussed. Finally, experimental results obtained for C_2H_4, and for the structurally similar vinyl chloride (C_2H_3Cl) and vinyl bromide (C_2H_3Br) diluted in nonabsorbing buffer gases such as Kr, Ar, He, N_2 and mixtures among them are presented.

5.1 Theoretical Considerations

The deflection of a (cw) probe laser beam is used in the PTBD technique to monitor the gas density fluctuation. The origin of the deflection is the refractive index variation induced by the density variation that occurs after a laser pulse excitation as outlined above in chapter 2. Mathematically, the refractive index n is usually described as a function of

the temperature and of the density of the medium as given by the Lorenz-Lorenz relationship

$$\frac{n^2-1}{n^2+2}=\frac{R_m\rho}{m} \quad , \tag{59}$$

where R_m [m^3 mol^{-1}] is the molar refractivity, ρ [kg m^{-3}] is the density, and m [kg mol^{-1}] is the molecular weight of the medium. Although R_m is temperature dependent, this dependence can be neglected for pressures below a few atmospheres and moderate temperature fluctuations. In this case, only the density change is relevant for the refractive index (Bialkowski [1996] p. 307, Barker and Rothem [1982], Jackson [1983] p. 180). The variation of the refractive index by density changes for small changes in temperature and density can thus be written as

$$\left(\frac{\partial n}{\partial \rho}\right)_T=\frac{\left(n_0^2+2\right)^2}{6n_0}\frac{R_m}{m} \quad , \tag{60}$$

where n_0 is the refractive index of the medium. By integrating equation (60) and considering that $n_0 \cong 1$ at standard conditions, we obtain a linear dependence of the refractive index on the density,

$$n(\rho)\cong\frac{3}{2}\frac{R_m}{m}\rho \quad . \tag{61}$$

The deflection of a cw probe laser caused by the refractive index variation depends on the employed PTBD scheme. The PTBD technique is generally applied in both, the parallel and the transversal pump-probe beam configuration (Bialkowski [1996], Fournier and Boccara [1988]). In this study, we applied the parallel configuration that offers the possibility to increase the deflection amplitude by a long interaction length between the pump and probe beam. In this configuration the deflection signal $S(t,r)$ detected by a weak probe beam at a radial distance $r=d$ from the pump beam axis after an interaction length l is proportional to the (cylindrical) radial partial derivative of $n(r,t)$ at $r=d$ multiplied by l (Tam et al. [1985], Tam [1986], Jackson et al. [1981])

$$S(t,r=d)\propto l^2.\left.\frac{\partial n(r,t)}{\partial r}\right|_{r=d} \quad . \tag{62}$$

It should be noted that this simple proportionality holds only for small density variations. In view of equations (60) and (32), the PTBD signal is expressed as

$$S(t,r) \propto l^2 \cdot \sum_{j=1}^{\infty} \nu_j c_j(t) J_1(\nu_j r) \quad , \tag{63}$$

where J_1 denotes the first-order Bessel function.

In all our PTBD investigations we used a numerical implementation of this equation considering 78 terms (limited by the capacity of the computer used) in the signal series expansion in order to guarantee the convergence of the theoretical results (Barker and Toselli [1988]). As outlined in chapter 2, a fit of the experimental signals permits to determine directly the relaxation time τ_{relax} or relaxation rate coefficient $k_e = 1/\tau_{relax}$ and the thermal conductivity λ from a single measurement.

5.2 Typical PTBD Signals

Our first measurements of time-dependent PT deflection signals have been performed on highly diluted SF_6/Ar mixtures. The results are illustrated in Figs. 5.1 to 5.3. Figure 5.1 shows the signals for a total pressure of 43 mbar, a pump beam radius r_b of approximately 1.75 mm and a distance d of 0.5 mm between pump and probe beam, i.e. the probe beam propagates inside the region irradiated by the pump beam. The laser was tuned to 944.2 cm^{-1} (10P(20) transition) within the ν_3 absorption band of SF_6 at a fluence of 100 mJ/cm^2. The PT deflection signal due to the density changes by an acoustic and a thermal contribution is displayed in Fig. 5.1a while Fig. 5.1b depicts the further evolution of this signal. The observed decay is caused by thermal diffusion whereas the superimposed equidistant structures represent echoes of the original acoustic signal. A time analysis thus permits an easy determination of the sound speed in a gas mixture. If the total pressure is increased to 160 mbar (Figs. 5.2 and 5.3) at identical SF_6 partial pressure and identical distance d, the signal rise sets in earlier and is steeper. Furthermore, the acoustic contribution to the signal is more pronounced resulting in the observed overshooting (5.2a). As expected, the thermal decay on the other hand becomes much slower. If d is increased up to a distance outside the pump beam region, the acoustic contribution to the PT deflection signal becomes dominant. This behaviour is reflected by the change of the temporal signal shape as seen in Figs. 5.3a and 5.3b where an increasing negative part of the signal originating solely from the acoustic contribution

is obtained. For a distance d larger than the pump beam radius, the information on the thermal diffusion is lost as is evident from Fig. 5.3b.

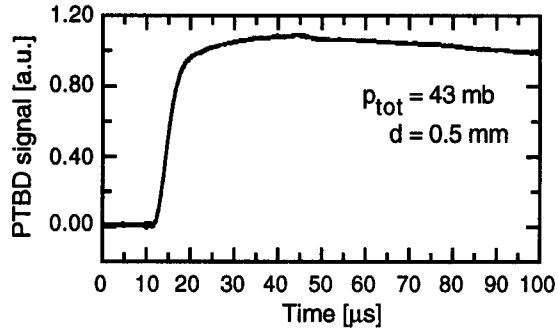

Fig. 5.1a

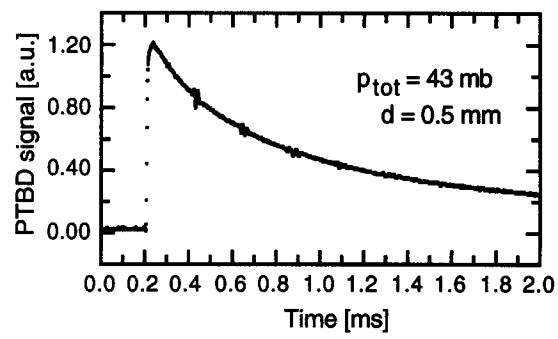

Fig. 5.1b

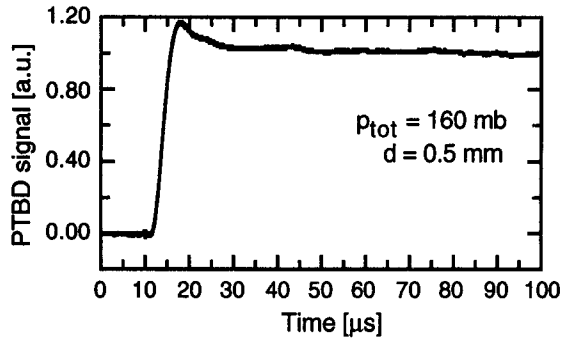

Fig. 5.2a

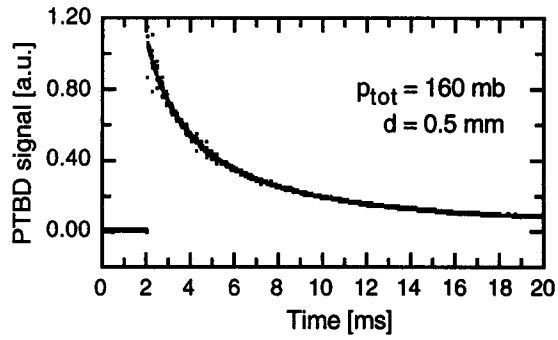

Fig. 5.2b

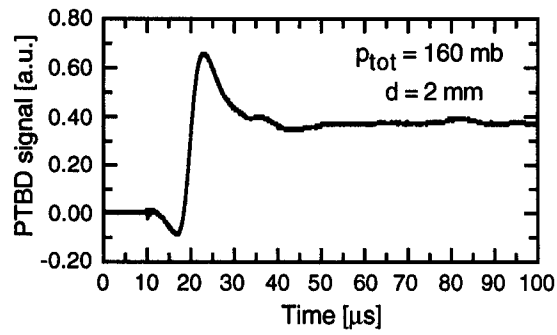

Fig. 5.3a

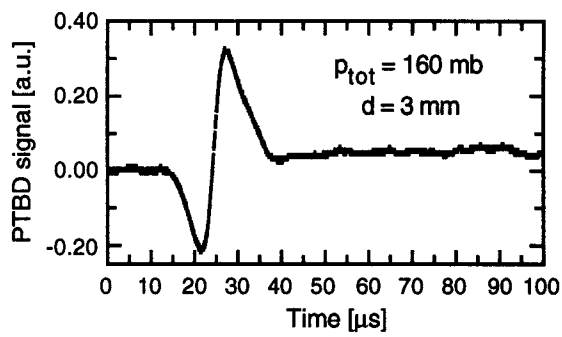

Fig. 5.3b

Figures 5.1-5.3. *Time dependence of PT deflection signal recorded at 944.2 cm^{-1} with a fluence of 100 mJ/cm^2 for a pump beam diameter of 3.5 mm in highly diluted SF_6/Ar mixtures for different total pressures p_{tot}, time scales and distances d between pump and probe beam (for further details see text).*

Thanks to the possibility to perform experiments at varying distance d, we thus gain insight into the underlying physical processes. If the probe beam propagates outside the region of pump beam, the PT signal contains information about the relaxation time τ_{relax},

the sound velocity and the diameter of the pump beam. In the region inside the pump beam both the diffusion and the thermal conductivity contribute also to the PT signal.

5.3 The Alignment of Pump and Probe Beam

Before we start with the numerical analysis of the signals, it is important to consider the alignment characteristics between pump and probe beam and to investigate the influence of misalignment onto the measured signal. The coaxial alignment of pump and probe beams is crucial for PTBD measurements with parallel alignment configuration. A parallel displacement, i.e. variation of the distance d between pump and probe beam can then easily be realized by using a mechanical translation stage. We achieved coaxial alignment using two pinholes placed at each end side of the cell and separated by a distance of 1.5 m. A further improvement was obtained by checking the probe beam signal at the position sensor while operating the pump laser. This signal should completely vanish when perfect coaxial alignment by slight adjustment of the HeNe probe laser beam axis is achieved because in this case only thermal lensing of the probe laser occurs without displacement. Any remaining small misalignments have only a negligible influence on the PTBD shape as is demonstrated in Fig. 5.4a-b.

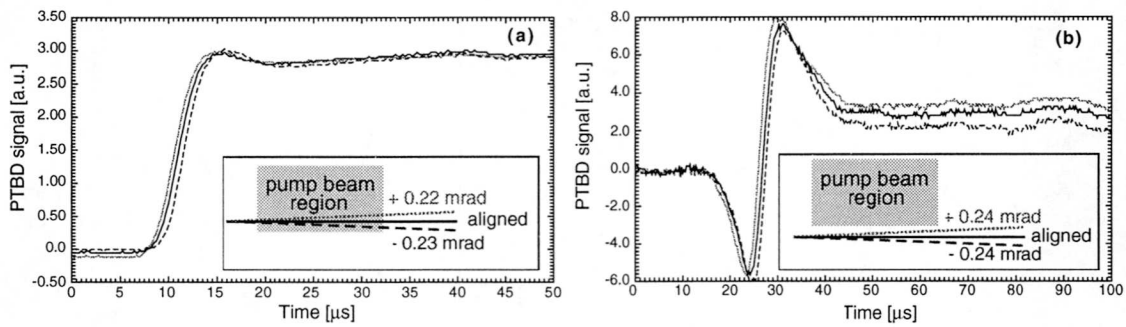

Figure 5.4. *PTBD signals for a pump beam radius of 2.5 mm, measured inside (a) and outside (b) the pump region at a distance d of 1.7 mm and 5.5 mm, respectively, with a pump-probe misalignment on the order of 0.23 mrad. The dotted line indicates a misalignment towards the pump beam, the solid line denotes perfect coaxial alignment and the dashed line results from a misalignment away from the pump beam. The inserts depict the corresponding configurations.*

Here results are shown for both cases of the probe beam inside or outside the pump beam region for an assumed deviation of ≅ 0.23 mrad from coaxiality, a value much larger than achieved in practice. The negligible influence of the assumed alignment on the temporal PTBD signal shape is explained by the fact that the displacement at the cell end after the

interaction length of 55 cm, amounts to only 0.1 mm which is still small compared to the pump beam radius. It is interesting to note that in case (b) the misalignment directed towards the pump beam presents a larger signal than that for the opposite case because this beam senses the thermal diffusivity first.

5.4 Analysis of PTBD Signals

5.4.1 Derivation of Physical Parameters

In the following we apply the mathematical model outlined in chapter 2 to describe our experimental PTBD results. We discuss experimental situations where the theoretical treatment proposed by Barker and Toselli (Barker and Toselli [1988]) fails but where our approach with a three-species model is successful. In Fig. 5.5 we present time-dependent PTBD signals recorded at room temperature and a total gas pressure of 150 mbar for the following gas mixtures: 1.0% SF_6 buffered in pure Ar (Fig. 5.5a) and 1.0% C_2H_4 buffered in (He/Ar) mixtures with He-to-Ar concentration ratios $c_{(He/Ar)}$ of 0.0, 92.7 and 100.0% (Figs. 5.5b-d, respectively). All experiments are performed far below absorption saturation, in fact less than 0.01% of the number of absorbing molecules are excited. The signal shown in Fig. 5.5a was recorded within the ν_3 band of SF_6 at 949.479 cm^{-1}, whereas for the signals shown in Figs. 5.5b-d the laser was tuned to the ν_7 ethylene absorption band at 949.433 cm^{-1}. The curves obtained by the use of Barker's model are represented by dotted lines, whereas the solid lines correspond to the fits performed with our new three-species treatment. The experimentally observed superimposed equidistant structures present in the decaying part of the signals (light symbols) are not considered in the numerical analyses of these measurements. As previously commented (Calasso et al. [1996], Barker and Toselli [1988], Jacobs [1989]) these structures represent echo signals, i.e. acoustic waves reflected from the cell walls. In the attempt to keep the numerical description in a simple form, we used zeroth-order Bessel functions to describe the gas density fluctuation. However, this approach imposes incorrect boundary conditions (Barker and Toselli [1988], Toselli et al. [1990], Jacobs [1989]). As a consequence, the theoretically predicted echoes appear at the correct times but their phases are incorrect and their amplitudes are by far too large and have thus no further meaning for our comparisons with experimental data.

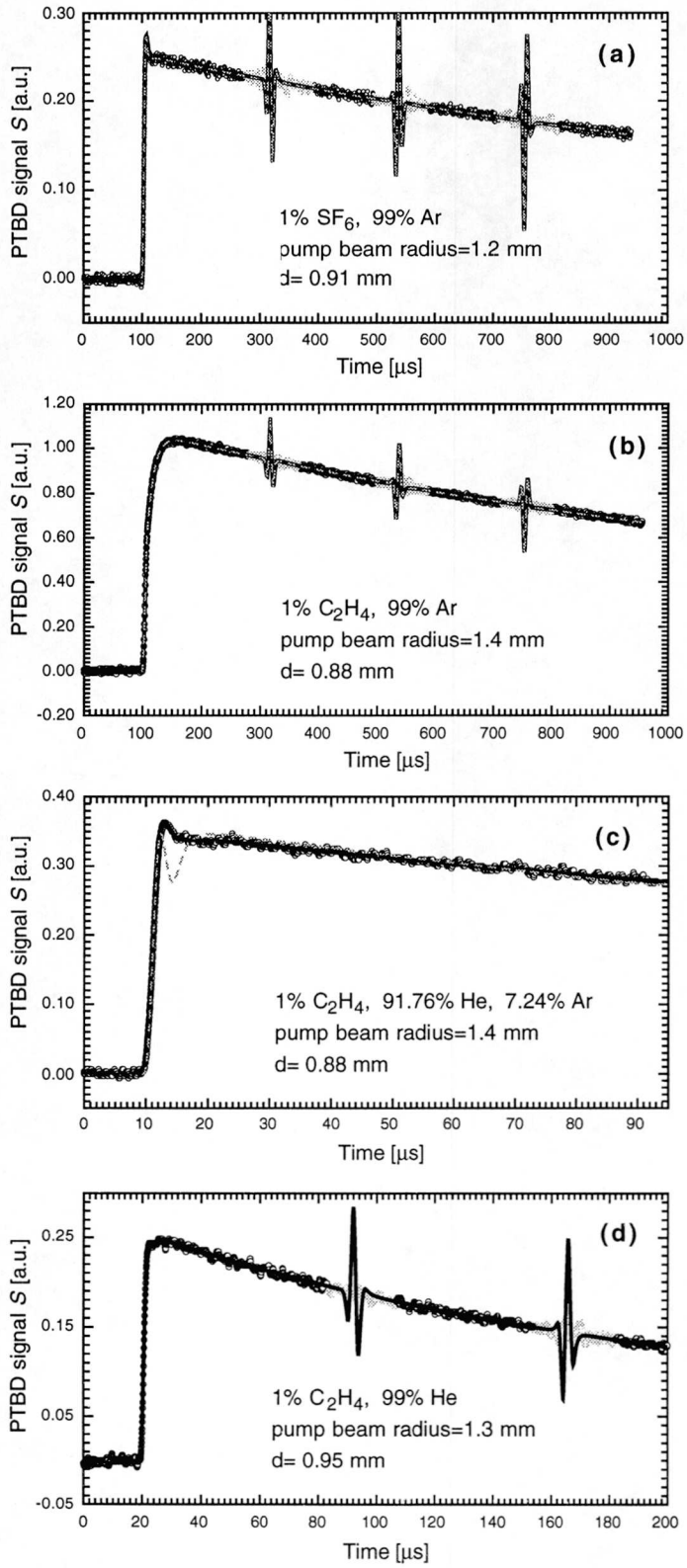

Figure 5.5. *Time-dependent photothermal beam deflection signals obtained at room temperature and a total pressure of 150 mbar for (a) SF_6 /Ar and (b-d) C_2H_4 /(He/Ar) gas mixtures. The gas composition, pump beam radius r_b and distance d between pump and probe beam are indicated in each case. The solid black and dotted gray lines represent the theoretical curves obtained by fitting the experimental data (indicated by non-filled circles) to the three- and two-species model, respectively. The experimental data represented by the light open circles (signal echoes) are not used for the fits (see text). The derived relaxation rate coefficient k_e per unit pressure and thermal conductivities λ are presented in Table 5.1.*

The first order relaxation rate coefficient $k_e = 1/\tau_{relax}$ where τ_{relax} corresponds to the V-T energy transfer process in our case of infrared excitation (see Figs. 5.1-5.3), dominates the fast rising part of the signal whereas the thermal conductivity λ is responsible for the slow signal decay. These two parameters can be derived by both theoretical models and the corresponding data are listed in Table 5.1. Figures 5.5a-b imply that both models yield identical signal shapes for the SF_6/Ar and C_2H_4/Ar samples, in excellent agreement with the experimental data. The small differences between the derived relaxation times and thermal conductivities for these samples (see Table 5.1) also indicate that for the energy conditions present in these experiments, the use of the two- and the three-species models are equivalent even for mass relationships m_1/m_2 of about 3.6 between absorbing gas and buffer gas (see Eq. (6a-b)) in accordance with previously reported experimental results (Calasso et al. [1996], Toselli et al. [1990]). However, as pointed out in chapter 2, this situation can be radically different for other energy conditions and/or other (larger) m_1/m_2 ratios. It should also be remembered that the buffer gas only appears as collision partner M within the theoretical models. Only its average molar mass is relevant whereas its composition does not play any role. It is thus not important whether the buffer gas consists of one or more species. As shown in Fig. 5.5c this latter experimental condition is fulfilled, e.g., for a sample of C_2H_4 buffered in a He/Ar mixture with a concentration ratio $c_{(He/Ar)} = 92.7\%$. In this case, the average molar mass of the buffer gas, expressed as $m_2 = c_{(He/Ar)} m_{He} + (1 - c_{(He/Ar)}) m_{Ar}$ in terms of the He and Ar molar masses m_{He}, m_{Ar} respectively, yields a ratio $m_1/m_2 \approx 4.22$. In contrast to the former cases (Figs. 5.5a,b), substantial discrepancies between the theoretical curves derived by the two theories become evident. In particular, shortly after the initial rise of the signal, a sudden drop followed by a recovering signal rise before the characteristic slow thermal decay is predicted by the two-species treatment. This behaviour is neither observed in the experimental signal, nor obtained by our three-species modelling. Despite these discrepancies a numerical fit was performed with both approaches. As tabulated in Table 5.1, the derived relaxation rate coefficient k_e per unit pressure and thermal conductivity λ exhibit large deviations. The discrepancies between the two models are even more pronounced for the C_2H_4/He sample with $m_1/m_2 = 7$. The two-species model fails completely in this case and its predictions are thus not included in Fig. 5.5d nor can the parameters k_e and λ be derived. However, our three-species approach yields excellent agreement with the experiment as shown in 5.5d. Only small deviations from literature data obtained with the beam deflection method (Gagné and Chin [1991]) and with the laser-induced fluorescence method (Yuan et al. [1973/a-b]) are observed. The larger deviation for the C_2H_4/Ar mixture is explained by the higher concentration of 1% of absorbing gas used in our experiments.

Table 5.1. *First-order relaxation rate coefficient $k_e = 1/\tau_{relax}$ per unit pressure and thermal conductivity λ derived with the two- and our new three-species approach from the experimental data of Fig. 5.5 for 1% concentration of absorbing gas. Furthermore, the buffer gas concentration ratios $c_{(He/Ar)}$ for the gas mixtures of C_2H_4 in (He/Ar) and the molecular mass ratios m_1/m_2 between absorbing and buffer gas are indicated. Available literature data are included for comparison. The indicated absolute and relative errors are obtained from Eq. (64) below.*

		SF_6/Ar	C_2H_4/(He/Ar)		
$c_{(He/Ar)}$[%]		0.0	0.0	92.7	100.0
m_1/m_2		3.650	0.700	4.223	7.000
$\frac{k_e}{p} = \frac{1}{\tau_{relax}\, p}$	two species	1.9	0.38	2.9	---
	three species	1.9±0.2	0.38±0.03	3.7±0.4	3.9±0.4
[ms^{-1} $mbar^{-1}$]	literature	~1.90[a]	0.35[b]	---	4.09[b]
λ	two species	18.4	22.2	67.4	---
$[\frac{mW}{m \cdot K}]$	three species	18.5	22.0	113.9	170.0
	literature*	~18.5[c]		---	~146.8[d]

** It should be noted that these literature data correspond to the values of pure Ar and pure He and not of the actual mixtures. ([a] Gagné and Chin [1991], [b] Yuan et al. [1973/b], [c] Bailey et al. [1981], [d] Handbook of Chem. and Phys. [1977])*

We found that the theory is also appropriate for fitting the complete PT signal evolution in the low-pressure regime where binary diffusion between excited and unexcited molecules is present during the relaxation time as well as for the high-pressure regime where the molecules relax much faster resulting in a steeper signal.

When the distance d between the pump and the probe beam, is increased beyond the pump beam radius (see e.g. Fig. 5.3a-b above), the PT signal is determined solely by the generated pressure pulse, i.e. the contribution by the thermal conductivity can be ignored.

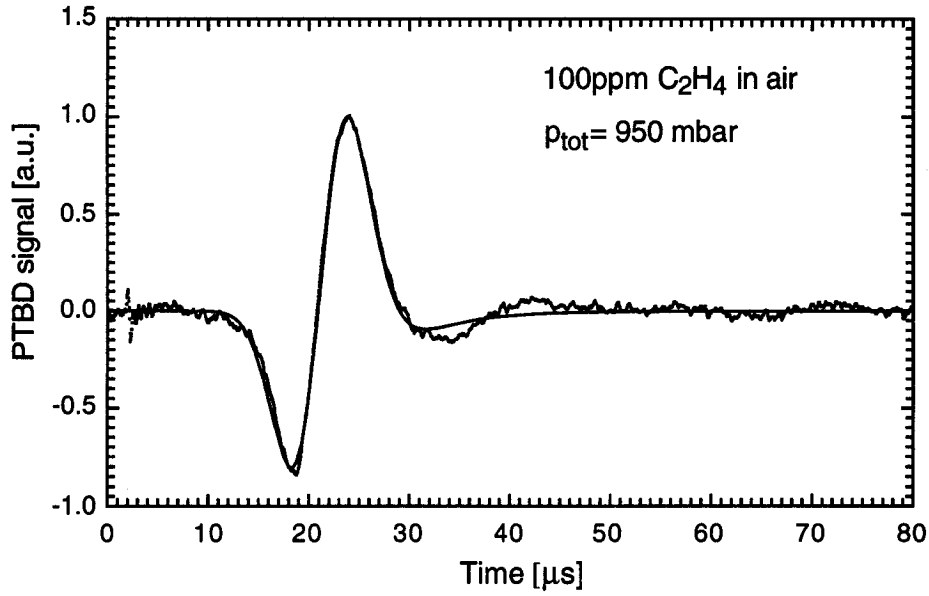

Figure 5.6. *Comparison between measured and calculated PT beam deflection signals for r_b = 1.35 mm and d = 5 mm. The derived relaxation time is τ_{relax} = 2.5 µs for p_{tot} = 950 mbar.*

Figure 5.6, which shows the recorded PTBD signal for 100 ppm C_2H_4 buffered in synthetic air at 950 mbar with a pump radius r_b of 1.35 mm and a distance d of 5 mm, implies that excellent agreement between experiment and theory is also obtained in this case. The derived relaxation time τ_{relax} = 2.5 µs again agrees with literature data as reported below on the basis of measurements obtained for the configuration with $d < r_b$.

5.4.2 Accuracy Considerations

The numerical simulation of beam deflection signals under different experimental conditions permits to explore experimental regimes for which physical parameters can be derived from measured PTBD signals with a given accuracy. In particular we studied the critical situation that is present when the relaxation time τ_{relax} is shorter than the acoustic transit time $\tau_s = r_b / v_s$, where r_b and v_s denote the pump beam radius and the sound speed, respectively. In this adiabatic case, the heat produces an immediate change in temperature and in pressure but the density variation, which is the origin of the refractive index change, does not develop until the pressure wave in the gas has crossed the

absorption region. In this case, the rise time of the PTBD signal approaches the transit time τ_s. Therefore, photo-detectors with a rise time well below τ_s should be used for the signal detection (in our case the detector rise time was 0.3 µs) in order to resolve the signal rise. The shorter the relaxation time, the smaller is the change in the signal shape. Such a convergent trend is illustrated in Fig. 5.7a. Here we present beam deflection signal shapes for τ_{relax} between 8.0 and 0.5 µs, calculated for SF_6/Ar mixtures at a total gas pressure of 160 mbar with, r_b = 3.5 mm and d = 0.5 mm. An example for the convergent behaviour of experimental signal shapes for short relaxation times is illustrated in Fig. 5.7b where four signals obtained for increasing gas pressures resulting in decreasing relaxation times are depicted.

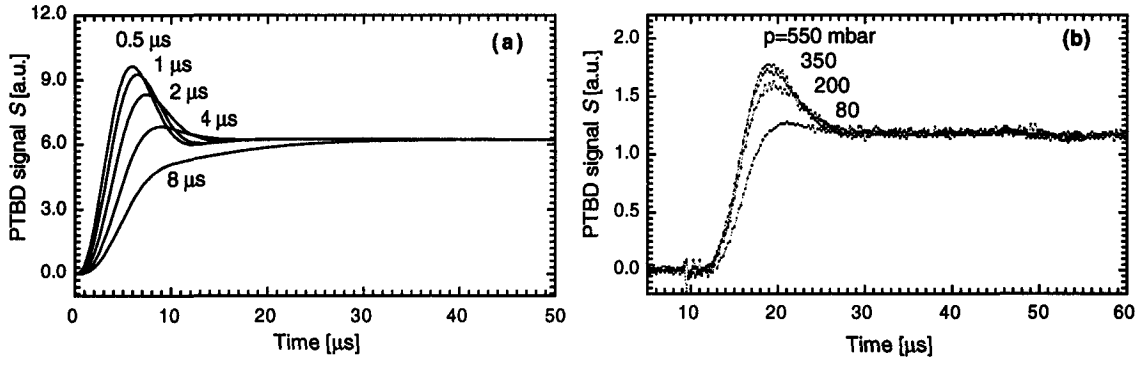

Figure 5.7. *Convergent trend of beam deflection photothermal signal shapes for SF_6/Ar mixtures for short relaxation times. (a) Theoretical calculations for relaxation times τ_{relax} of 8.0, 4.0, 2.0, 1.0 and 0.5 µs for a total gas pressure of 160 mbar, pump beam radius r_b of 1.75 mm and distance d of 0.5 mm between pump and probe beam. (b) Experimental curves obtained for total gas pressures of 80, 200, 350 and 550 mbar. These experimental signals were recorded at r_b = 1.75 mm and d = 1.2 mm.*

The converging signal shapes indicate that longer relaxation times can be determined from experimental data with higher accuracy than shorter times, since this accuracy strongly depends upon the degree of shape deviations between theoretical signals under the existent (obviously limited) instrumental precision conditions. To determine the shortest reliable relaxation time which can be obtained under particular experimental noise conditions, we refer to the statistical definition of variance (Press et al. [1992]). We introduce the relaxation time-dependent function

$$y^2(\tau_{relax}) := \frac{\int_0^{t_0} [S(r,t;\tau_{relax} - \Delta\tau_{relax}) - S(r,t;\tau_{relax} + \Delta\tau_{relax})]^2 \, dt}{t_0} \qquad (64)$$

to achieve a quantitative estimation of the degree of shape deviation of a PTBD signal $S(r,t;\tau_{relax})$ corresponding to a given τ_{relax} in the above mentioned convergent region. In equation (64), t_0 represents a characteristic time at the decreasing parts of the signals involved, for which the signal shapes cannot be distinguished any more (see e.g. Fig. 5.7). In order to monitor changes occurring for short relaxation times with higher accuracy we consider the increment $\Delta\tau_{relax}$ of Eq. (64) as proportional to τ_{relax}. This proportionality constant $g := \Delta\tau_{relax} / \tau_{relax}$ (< 1) can be used to represent the percentual degree of inaccuracy or relative error in the value of τ_{relax} we are willing to accept when performing a fit of an experimental signal. For a maximum signal noise N we may determine the relaxation times τ_{relax} that can be obtained within a relative error g by comparing N with the shape deviation function y introduced in Eq. (64). If for a given τ_{relax} and relative error g the corresponding y is larger than the noise N, a fit of the experimental signal can still yield an accurate value for τ_{relax} with the error g. Since the maximum signal-to-noise ratio S/N rather than the noise itself is characteristic for the experiment, the accuracy condition ($y>N$) is better stated in terms of S/N and $A_{max} / y(\tau_{relax})$, where A_{max} represents the maximum amplitude of the theoretical signal, as

$$S/N > A_{max} / y(\tau_{relax}) \quad . \tag{65}$$

As expected, short relaxation times can only be derived from signals with optimized S/N ratios. For constant N this can be achieved by varying the distance d until the largest experimental signal amplitude S is reached. Since the signal is proportional to the derivative of $\rho(r,t)$ with respect to r at $r = d$, the largest signal amplitude is obtained for $d = r_b / \sqrt{2}$ for a Gaussian pump beam profile with radius r_b.

An illustration on how the discrimination criterion introduced above can be applied in practice for the optimization of the PTBD experimental configuration is shown in Fig. 5.8. Here, the gas composition and pressure are those used for the measurements shown in Fig. 5.5a (1% SF_6 diluted in Ar) for various characteristic times τ_s, and thus pump beam radii r_b, as indicated. The dotted curve denotes the calculated function $A_{max} / y(\tau_{relax})$ for PTBD signals for τ_s = 4.7 µs (corresponding to r_b = 1.5 mm), under consideration of a relative error $g = 10\%$. Focusing or defocusing of the pump laser beam yields the results indicated by the solid lines for the corresponding functions $A_{max} / y(\tau_{relax})$.

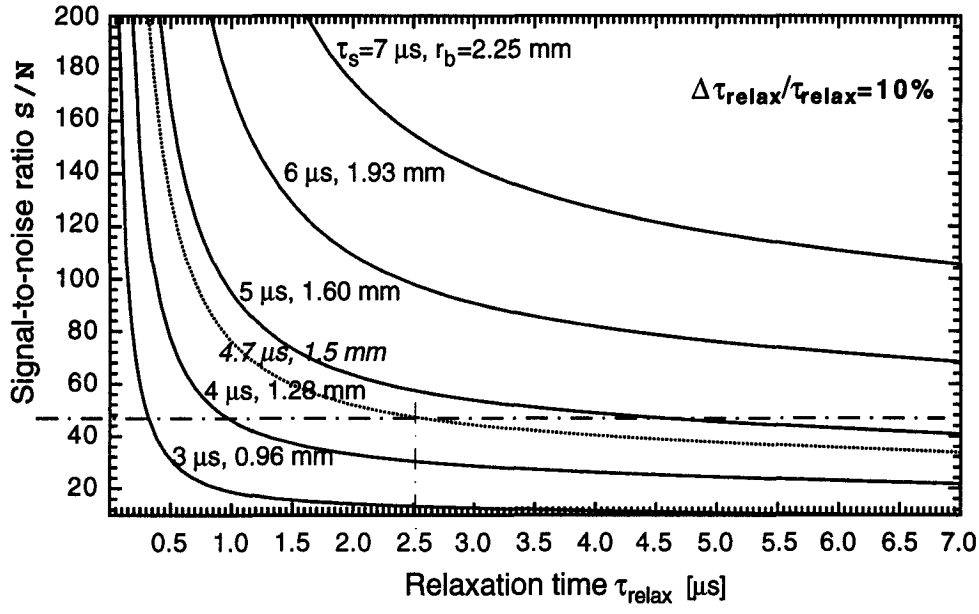

Figure 5.8. *Illustration of the practical application of the criterion (Eq. (65)) for the determination of the shortest relaxation time τ_{relax} to be obtained for a given experimental signal-to-noise S/N ratio (horizontal dashed-dotted line) and acceptance of a 10% error. The dotted curve represents the calculated function $A_{max}/y(\tau_{relax})$ for photothermal beam deflection signals for τ_s = 4.7 µs (corresponding to a pump beam radius r_b = 1.5 mm) and for the gas composition and pressure as in Fig. 5.5a. The corresponding functions $A_{max}/y(\tau_{relax})$ under conditions of focusing (r_b = 1.28 and 0.96 mm) and defocusing (r_b = 1.6, 1.93 and 2.25 mm) of the pump laser beam are represented by solid lines. The condition of Eq. (65) is fulfilled in each case for those relaxation times τ_{relax} for which the $A_{max}/y(\tau_{relax})$ curve lies below the indicated experimental S/N level, e.g. for $\tau_{relax} \leq 2.5$ µs only radii $r_b \leq 1.5$ mm are appropriate. For all calculations the pump-probe beam distance was $d = r_b/\sqrt{2}$.*

The horizontal dashed-dotted line represents the signal-to-noise level of our experiment shown in Fig. 5.5. It is seen that under the given conditions, the minimum τ_{relax} that can be determined within the assumed accuracy of 10% for τ_s = 4.7 µs (r_b = 1.5 mm) is approximately 2.6 µs and that this minimum can be shifted by changing the focusing conditions of the pump laser beam. For example, if τ_s = 5.0 µs (r_b = 1.6 mm, i.e. less focused pump laser beam) the accurate determination of relaxation times τ_{relax} shorter than 4.6 µs is not feasible, because the condition of Eq. (65) is not fulfilled. On the other hand, in order to determine shorter relaxation times τ_{relax}, the measurements should be performed with a better focused pump laser beam; e.g. τ_{relax} of 1.0 µs with a pump beam radius $r_b \leq 1.3$ mm for our case of an absorbing gas diluted in Ar. It should be remarked, however, that the applicability of this concept is limited in practice, because tighter focusing may increase the alignment difficulties between pump and probe laser beam and in addition absorption saturation may occur at high pump beam fluences.

Finally, it should be mentioned that the accuracy in the determination of τ_{relax} cannot be improved any further by considering a different relationship between r_b and d than the above stated $d = r_b / \sqrt{2}$ which optimizes the signal amplitude in the case of a Gaussian pump beam profile. In order to verify this hypothesis it is sufficient to consider a more simplified function for the degree of shape deviation than the one given in Eq. (64). We use the function $1 - S(r = d, t; \tau_{relax} + \Delta\tau_{relax}) / S(r = d, t; \tau_{relax})$ that is independent of the signal amplitude and which monitors the normalized difference between two signals S detected at $r = d$ for the distinct relaxation times $\tau_{relax} + \Delta\tau_{relax}$ and τ_{relax} and demonstrate that this function (or its equivalent $S(r = d, t; \tau_{relax} + \Delta\tau_{relax}) / S(r = d, t; \tau_{relax})$) does not depend on d. In other words, the following mathematical relationship should hold

$$S(d_1, t; \tau_{relax}) \cdot S(d_2, t; \tau_{relax} + \Delta\tau_{relax}) = S(d_2, t; \tau_{relax}) \cdot S(d_1, t; \tau_{relax} + \Delta\tau_{relax}) \qquad (66)$$

for all d_1 and d_2. The proof of Eq. (66) is achieved under the assumption that the signal with a relaxation time τ_{relax} incremented by $\Delta\tau_{relax}$ can be approximated by

$$S(r = d, t; \tau_{relax} + \Delta\tau_{relax}) = \frac{\partial S(r = d, t; \tau_{relax})}{\partial \tau_{relax}} \Delta\tau_{relax} \quad . \qquad (67)$$

Since all the information on the parameter τ_{relax} is contained in the $c_j(t)$ expansion coefficients of the density fluctuation $\rho(r,t)$, substitution of Eqs. (67) and (63) into (66) yields the obviously true expression

$$\sum_{ij} c_j \nu_j J_1(\nu_j d_1) \frac{\partial c_i}{\partial \tau_{relax}} \nu_i J_1(\nu_i d_2) = \sum_{ij} c_j \nu_j J_1(\nu_j d_2) \frac{\partial c_i}{\partial \tau_{relax}} \nu_i J_1(\nu_i d_1) \quad . \qquad (68)$$

This result demonstrates that the information contained in the signal $S(r = d, t; \tau_{relax})$ about the relaxation time τ_{relax} is independent of the chosen experimental parameter d.

5.5 Deactivation Rate Measurements on Different Gases and Gas Mixtures

5.5.1 Ethylene (C_2H_4)

The absorption of $H_2C{=}CH_2$ in the spectral region considered in this study is produced mainly by the excitation of the ν_7 vibrational mode, in which the four hydrogen atoms move in phase perpendicular to the molecular plane ("butterfly"-vibration). Part of the absorption spectra in the 10P branches recorded with our PA setup is shown in Fig. 5.9.

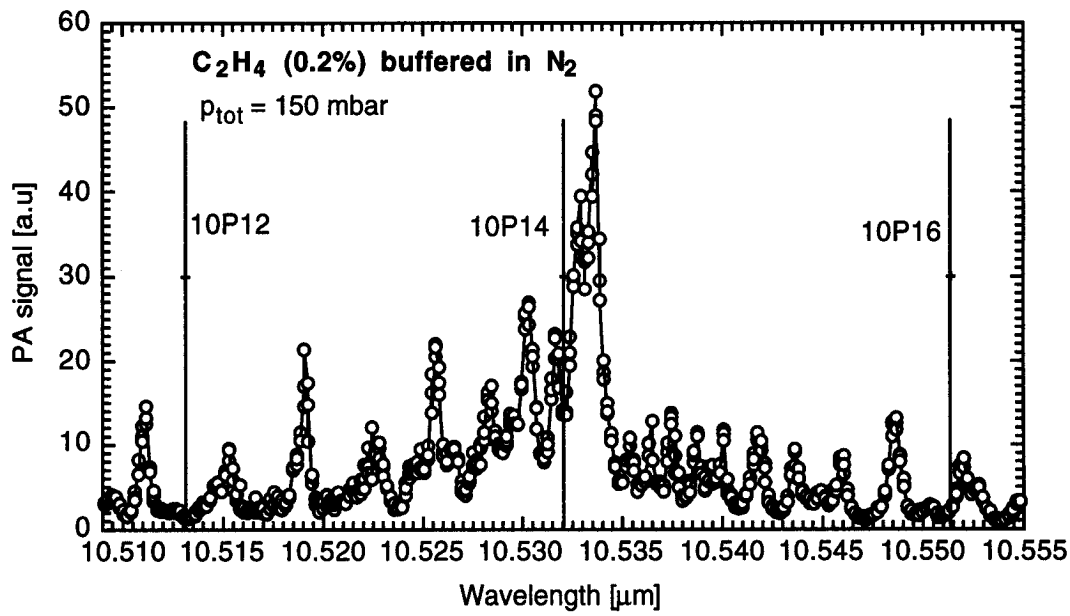

Figure 5.9. *PA spectrum of 0.2 % ethylene in N_2 at a total pressure of 150 mbar and room temperature in the 10P CO_2 branch. The vertical lines indicate CO_2 laser transitions.*

The well-defined structures are produced by the excitation of rotational-vibrational transitions in the ν_7 vibrational band. The large absorption peak near the 10P14 CO_2 laser line corresponds to the centre of the ν_7 band. The peaks observed in Fig. 5.9 are due to transitions between rotational sublevels of the vibrational ground state. On the right hand part of the spectrum, the Q-branch transitions ($\Delta J = 0$) are observed whereas on the left-hand part the P-branch transitions ($\Delta J = -1$) dominate. A detailed analysis is found in the literature (Herzberg [1991], Hollas [1982], Smith and Mills [1964]).

After a C_2H_4 molecule is pumped to the excited vibrational state in the ν_7 band it may relax by two general pathways. First, the molecule can be deexcited to nearby vibrational levels such as the ν_{10}, ν_8 and the ν_4 levels (Yuan et al. [1973/b]) via vibrational-vibrational (V-V) energy transfer processes (Chap. 2.1). In addition, it can be deactivated to the ground state by vibration-translation/rotation (V-T/R) energy transfer processes. Previous studies using the infrared double resonance techniques have demonstrated that V-V relaxation is approximately 50 times faster than V-T/R relaxation.

Unlike, e.g., the infrared laser double resonance scheme, the PTBD method does not sense explicitly a specific population density of an energy level, but instead monitors the overall transformation of the absorbed energy into thermal energy (V-T/R process). The different heat contributions resulting from the various relaxation processes can thus not be resolved by the PTBD method. In the case of the C_2H_4 molecule, however, the small energy gap between the involved vibrational levels results in a relatively small heat production by V-V compared to that by V-T energy transfer. Therefore only a small influence of V-V processes on the PTBD signal is expected despite their high efficiency in C_2H_4 (Yuan et al. [1973/b]). In fact our PTBD measurements did not give any indication of the occurrence of heat production processes in addition to the V-T energy transfer.

Finally, it should be remarked that we have investigated the ν_7 band of C_2H_4 with different pump wavelengths in order to find potential differences in relaxation processes. As expected, we did not find any differences. Therefore, almost all of our PTBD investigations on ethylene have been performed with the laser tuned to the highest absorption peak near the 10P14 CO_2 transition line (Fig. 5.9) in order to obtain optimum signal-to-noise ratio.

5.5.1.1 Pressure Dependent Relaxation-time

Molecules usually gain and loose vibrational and rotational energy through collisions (Lambert [1977]). What "collision" for molecules exactly means is difficult to define, considering the intermolecular potential. However, it is convenient to consider both energy transfer and chemical kinetics to define a "gas kinetic collision rate " Z, as the number of occasions per second at which the molecular centres approach within a certain distance (Rowlinson [1961]). Similar to elementary kinetic theory, where the molecules are considered as hard spheres, the gas kinetic constant rate, i.e. the number of collisions Z made by one molecule per second with a similar one, can be written as

$$Z = 4N\delta^2\sqrt{\frac{\pi kT}{m}} \quad . \tag{69}$$

Here N is the number of molecules per unit volume, δ is the interaction distance, and m the molecular mass.

In the case of a multicomponet mixture different collisional possibilities and therefore different parameters Z should be distinguished. Introducing Z_{relax} as the average number of collisions required for a molecule in an excited state to deactivate, the relaxation time is given by

$$\tau_{relax} = \frac{Z_{relax}}{Z} \quad . \tag{70}$$

A theoretical estimation of Z_{relax} can be found in the theories of Schwartz, Slawsky and Herzfeld "SSH" (Schwartz et al. [1952, 1954]) and of Shin (Shin [1972]). In contrast to the former models, the latter also considers molecular rotational effects. Since Z is proportional to the number of molecules and hence to the gas pressure as implied by Eq. (69) which is valid for pure gases as well as for multicomponet mixtures, the related relaxation time τ_{relax} varies inversely with total pressure. This behaviour is confirmed by our measurements performed at different pressures as shown in Fig. 5.10 and Fig. 5.12 for samples containing 0.2 % C_2H_4 buffered in Ar and for pure C_2H_4.

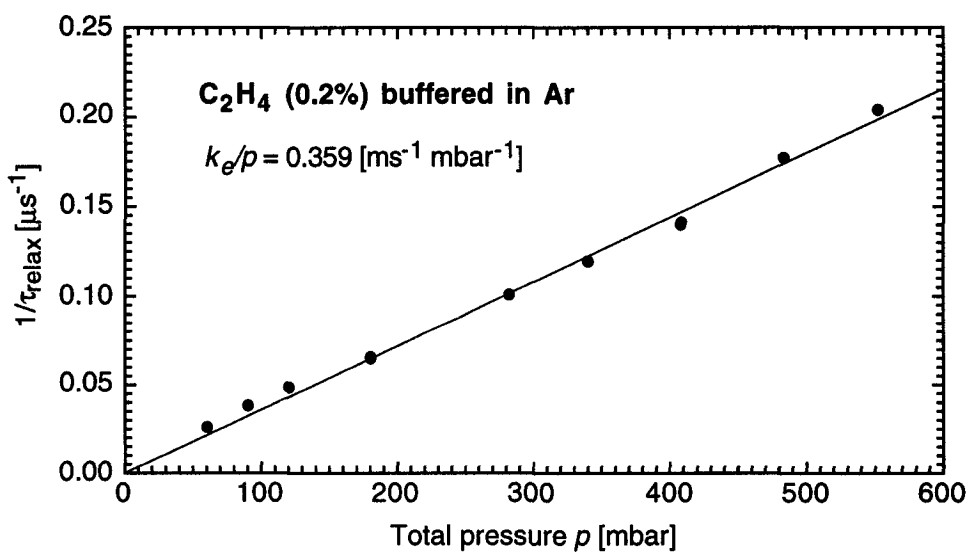

Figure 5.10. *Reciprocal relaxation time in function of total pressure for 0.2 % C_2H_4 buffered in Ar. The measured data points show a linear behaviour. The fit with a line yields a relaxation rate constant* $\beta = k_e/p = 0.359 \pm 1\ \%\ [ms^{-1}\ mbar^{-1}]$.

Based on such linear relationship it is convenient to introduce the pressure-independent relaxation rate constant $\beta = k_e/p$, where k_e is the relaxation rate coefficient and p the total pressure. The measurement presented in Fig. 5.10 yields a relaxation rate constant $\beta = 0.359 \pm 1$ % [ms^{-1} mbar^{-1}]. With this result and the estimation of $Z = 7.8 \cdot 10^3$ [ms^{-1} mbar^{-1}] (Yuan et al. [1973/b]), the average number of collisions needed for relaxation is about $Z_{relax} = 21700$. Considering the C_2H_4 concentration in the mixture and Z_{relax}, those numbers imply that statistically one C_2H_4 molecule collides with another C_2H_4 molecule after 500 collision, and that there are more than 43 collisions between two C_2H_4 molecule involved in the relaxation process. Considering the high efficiency of a V-V transfer, we expect that there is also some V-V energy transfer involved during deexcitation. However such V-V processes are not detectable by the PTBD method. This is confirmed by PTBD measurements on pure C_2H_4, where the highest number of V-V relaxation processes occurs. Figure 5.11 shows measurements obtained at 15 mbar of pure C_2H_4.

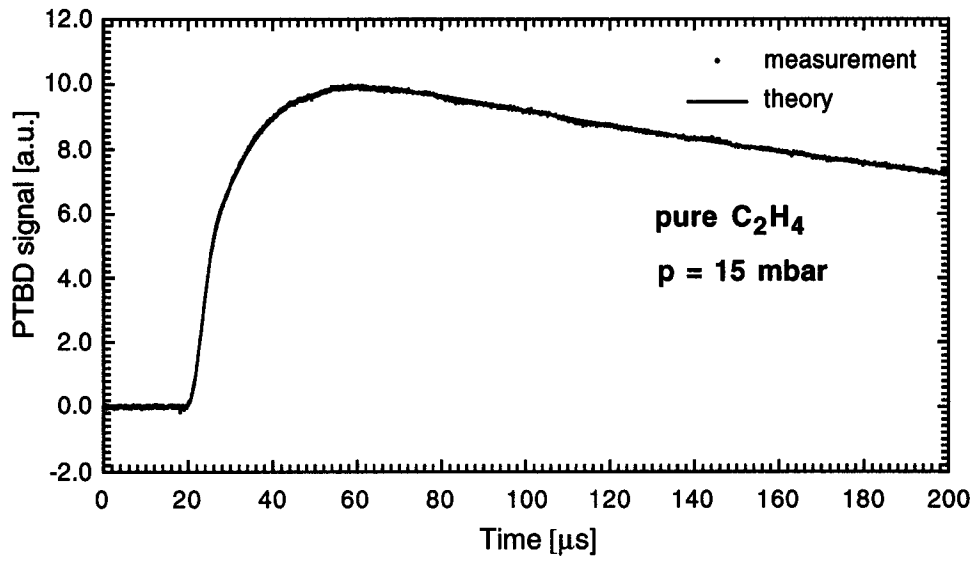

Figure 5.11. *PTBD measurement and fitted curve for pure C_2H_4 at 15 mbar with r_b = 1.32 mm, and d = 0.85 mm.*

The excellent agreement between the fitted curve and the measurement indicates that the signal is formed from a single relaxation process as assumed in the theoretical treatment. It should be noted that in order to avoid too strong absorption in this case the laser wavelength was shifted to a longer wavelength at 10.535 µm corresponding to a dip in the C_2H_4 absorption spectrum (Fig. 5.9). This adjustment is also chosen for the measurements performed at different pressures of pure C_2H_4 shown in Fig. 5.12.

Our measurements on pure C_2H_4 have been limited to low pressures, between 10 and 100 mbar, to avoid strong absorption and to maintain the accuracy of the derived relaxation time accuracy below 10 % considering the convergent signal behaviour for higher pressure, i.e. faster relaxation times (Chap. 5.4).

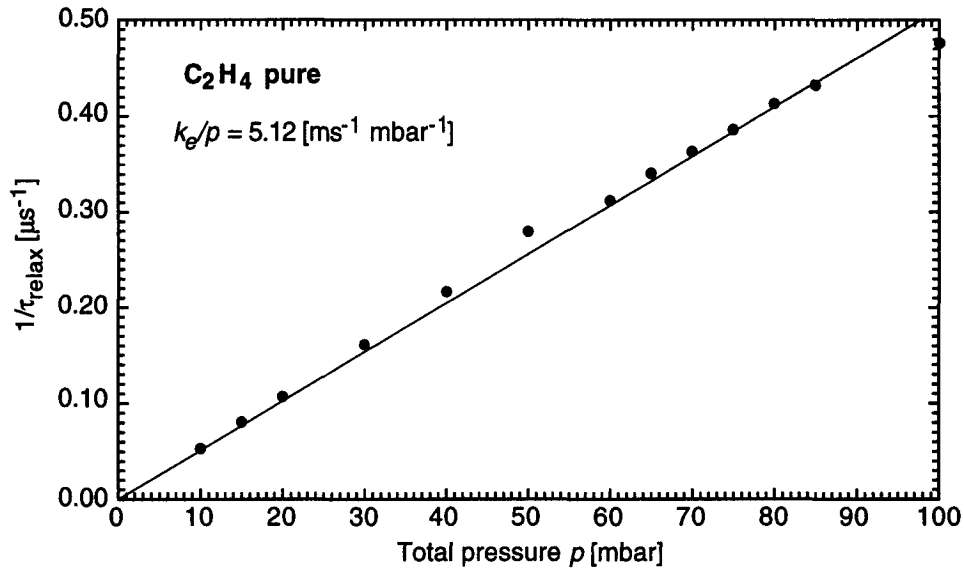

Figure 5.12. *Reciprocal relaxation time in function of pressure of pure C_2H_4 gas. The linear fit yields a relaxation rate constant $\beta = k_e/p = 5.12$ [ms^{-1} $mbar^{-1}$].*

The linear fit yields a relaxation rate constant $\beta = 5.12$ [ms^{-1} $mbar^{-1}$]. This is the fastest relaxation rate constant obtained for all measurement with C_2H_4. Such a high relaxation rate constant is explained by the largest number of V-V relaxation processes involved in this relaxation which favours V-T relaxation from lower energy levels which is more efficient and thus faster due to the smaller energy gap.

5.5.1.2 Deexcitation in Rare Gases

If a relaxing gas A is mixed with a non-relaxing gas B, such as a rare gas, there are two kinds of V-T deexcitation collision processes via which the excited relaxing gas A^* may transfer energy

(1) $A^* + A \rightarrow A + A$ (71a)

(2) $A^* + B \rightarrow A + B$. (71b)

Since (1) and (2) have different efficiencies, the result is a combined relaxation rate constant β_{A^*} for A^*, given by

$$\beta_{A^*} = x \cdot \beta_1 + (1-x) \cdot \beta_2 \quad , \tag{72}$$

where x is the mole fraction of A in the mixture and β_1 and β_2 are the relaxation rate constants for process (1) and (2), respectively.
To verify this relationship, we have performed measurements on C_2H_4 buffered in Kr, Ar, He and mixtures thereof.

A. C_2H_4 Buffered in Kr

Figure 5.13 shows measurements of relaxation rate constants of C_2H_4 buffered in Kr at several concentrations. The relaxation rate constant β is presented as function of the mole fraction of C_2H_4 in the C_2H_4/Kr mixture. The data are well fitted by the linear relationships predicted by Eq. (72). At low C_2H_4 concentrations (see insert) a larger scattering of data is observed due to the small signal.

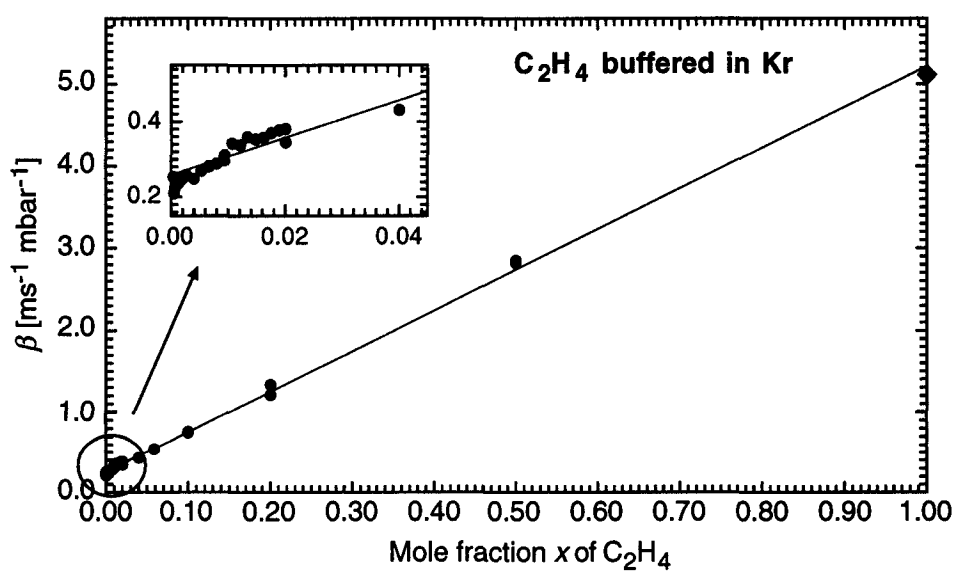

Figure 5.13. *Relaxation rate constant β of C_2H_4 buffered in Kr versus the mole fraction of C_2H_4 present in the gas mixture. The insert shows the part of low concentration in more detail. The diamond point at concentration "1" is obtained from the measurement made with pure ethylene. The data points evidence the expected linear behaviour. For very low C_2H_4 concentrations the V-T relaxation rate constant converges to $\beta = 0.26$ [ms^{-1} $mbar^{-1}$].*

The linear fit yields the following function for the relaxation rate constant β

$$\beta = 4.96 \cdot x + 0.26 \quad [\mathrm{ms^{-1}\ mbar^{-1}}] \ , \tag{73}$$

where x denotes the mole fraction of C_2H_4. Obviously, the V-T relaxation rate constant for C_2H_4 in Kr for very low concentrations is given by the intersection point of the fitted line with the ordinate yielding $\beta = 0.26$ [$\mathrm{ms^{-1}\ mbar^{-1}}$].

B. C_2H_4 Buffered in Ar

Figure 5.14 shows the measurement of relaxation rate constant β of C_2H_4 buffered in Ar for various concentrations.

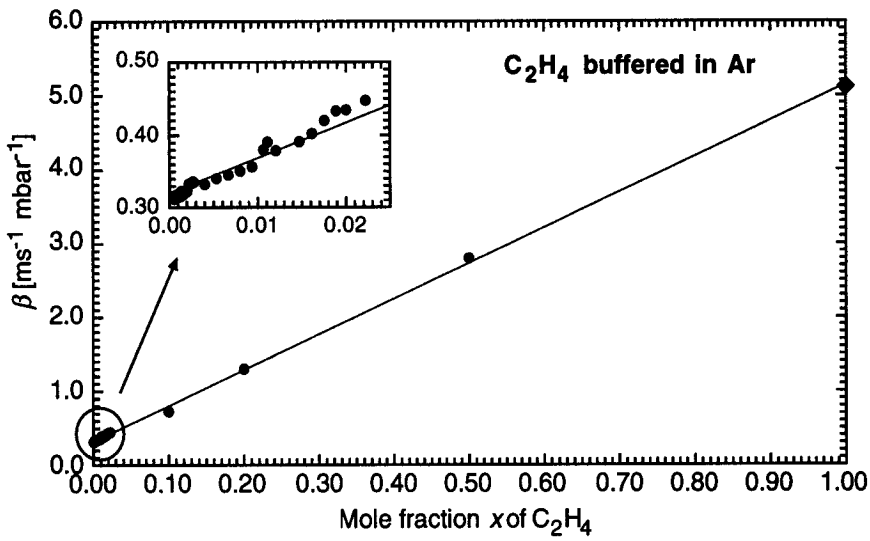

Figure 5.14. *Relaxation rate constant of C_2H_4 buffered in Ar versus the mole fraction of C_2H_4 present in the gas mixture. Like in Fig. 5.13 for Kr, the insert shows the data for low concentrations. The diamond point at concentration "1" refers to measurements made with pure ethylene. For very low C_2H_4 concentrations the V-T relaxation rate constant β converges to $\beta = 0.32$ [$\mathrm{ms^{-1}\ mbar^{-1}}$].*

The linear fit yields the relaxation rate constant β in dependence of the C_2H_4 concentration x

$$\beta = 4.82 \cdot x + 0.32 \quad [\mathrm{ms^{-1}\ mbar^{-1}}] \ . \tag{74}$$

At low concentrations β becomes 0.32 [$\mathrm{ms^{-1}\ mbar^{-1}}$].

C. C_2H_4 Buffered in He

Figure 5.15 implies that the relaxation rate constant β for C_2H_4 mixtures in He gives a larger scattering of data than what is observed for Kr and Ar mixtures. This scatter is probably caused by the small mass of He since it involves a larger concentration inaccuracy by the mixing process with the MKS gas mixing unit. Furthermore, the small mass impedes the preparation of a homogeneous gas mixture within the PTBD cell.

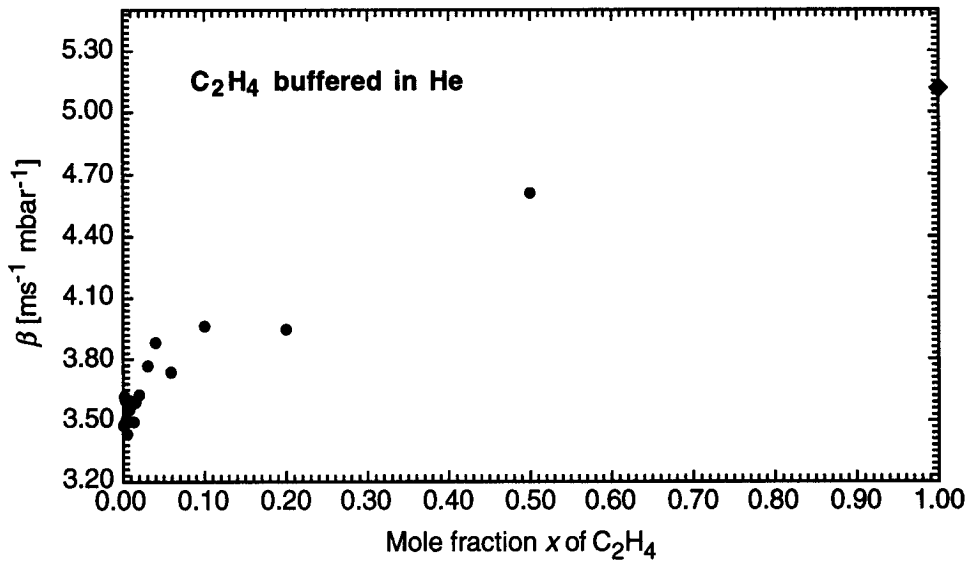

Figure 5.15. *Relaxation rate constant β of C_2H_4 buffered in He versus the mole fraction of C_2H_4 present in the gas mixture. The diamond point at concentration "1" refers to the measurement made with pure ethylene. For very low C_2H_4 concentrations the V-T relaxation rate constant β converges to 3.45 [ms^{-1} $mbar^{-1}$].*

Unlike for the measurements with Ar and Kr used as buffer gas we did not use a linear fit to derive β owing to the large scatter of data. Instead, we relied on the reasonable accuracy of data at low concentrations and have derived $\beta = 3.45$ [ms^{-1} $mbar^{-1}$].

A comparison of the relaxation rate constants obtained for C_2H_4 buffered in He, Ar, Kr confirms the expected behaviour that due to the less frequently occurring collisions slower relaxation processes occur for heavier buffer molecules.

D. C_2H_4 Buffered in an Ar/Kr and an Ar/He Mixture

Measurements obtained for 1 % C_2H_4 buffered in Kr/Ar mixtures and in Ar/He mixtures are represented in Fig. 5.16 and 5.17, respectively.

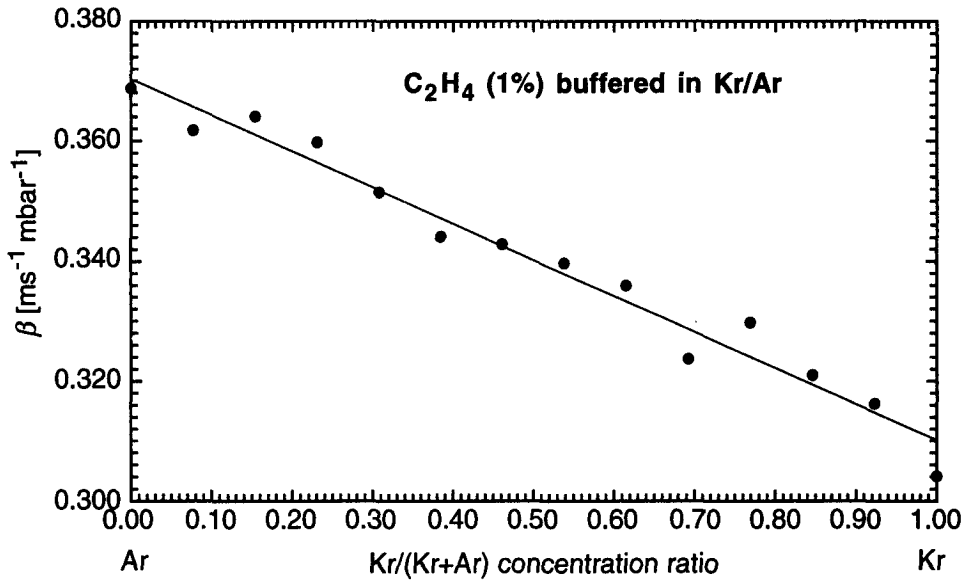

Figure 5.16. *Measurements of the relaxation rate constant β of 1 % C_2H_4 buffered in a mixture of Kr/Ar at a varying concentration ratio. Concentration "0" refers to pure Ar, "1" refers to pure Kr used as buffer gas.*

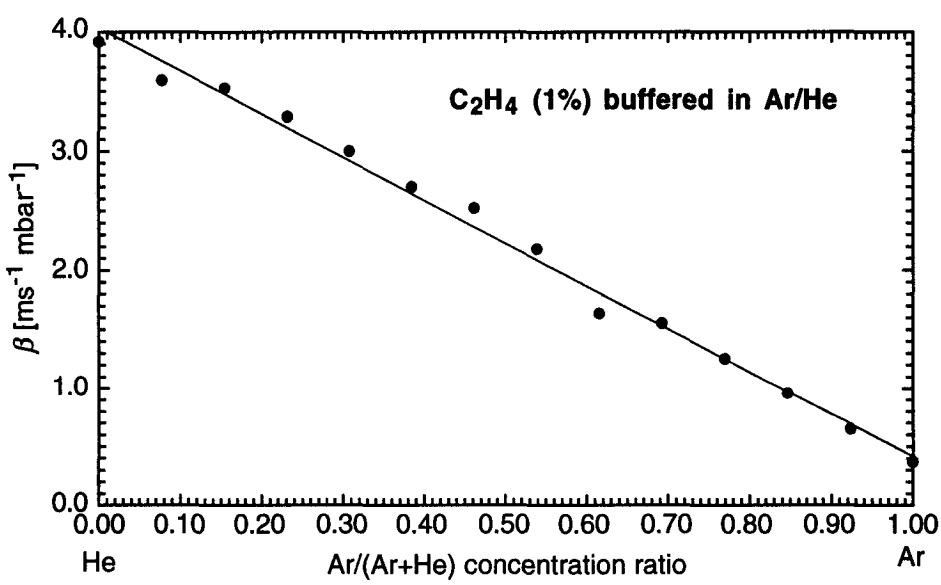

Figure 5.17. *Measurements of the relaxation rate constant β of 1 % C_2H_4 buffered in a mixture of Ar/He at a varying concentration ratio. Concentration "0" refers to pure He, "1" refers to pure Ar used as buffer gas.*

The linear behaviour in both measurement series between relaxation rate constant β and relative concentration of the Ar/Kr and Ar/He mixture indicates that no new relaxation processes occur in the mixture except those occurring in He, Ar, and Kr.

Furthermore, it should be pointed out that the relaxation rate constants of C_2H_4 buffered in pure He, Ar, and Kr at concentration "0" or "1" of this measurements are less accurate than the previous ones. This is on one hand due to the different averaging procedure in the measurements and on the other hand due to a mixing error of our gas mixing unit that allows small amounts residual gas to escape through the valve when in "closed" position. The concentrations "0" and "1" therefore do not correspond actually to the pure concentrations. This deviation is more noticeable in the case of pure He due to its high mobility.

5.5.1.3 C_2H_4 Buffered in N_2

Unlike the monoatomic buffer gases He, Ar and Kr, polyatomic buffer gases offer a large number of vibrational/rotational energy levels which favour V-V energy transfers with the excited molecule. Nitrogen (N_2) however, exhibits only a limited number of vibrational energy levels (the lowest one at 2331 cm^{-1}) and hence does not offer the possibility of vibrational energy transfer with the C_2H_4 molecule.

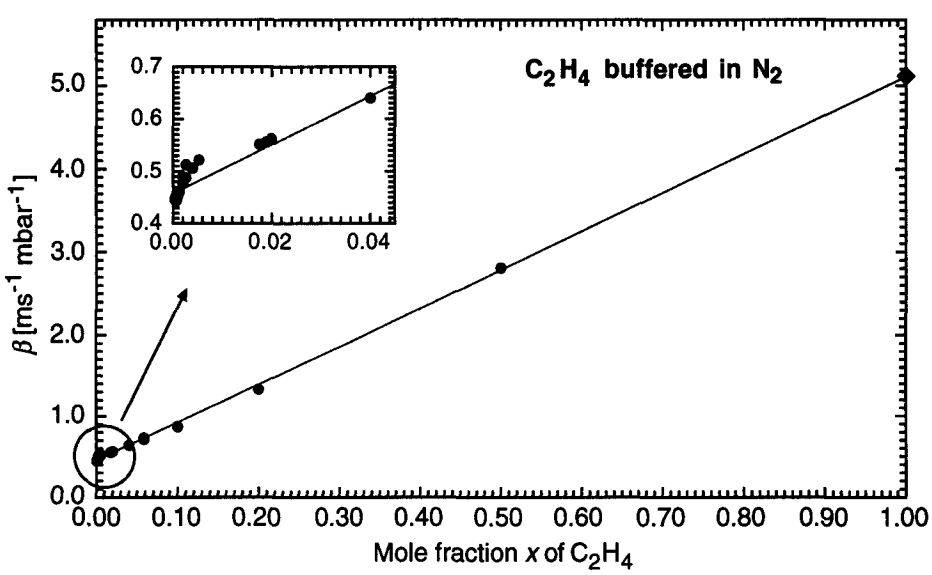

Figure 5.18. *Relaxation rate constant β of C_2H_4 buffered in N_2 versus the mole fraction of C_2H_4 present in the gas mixture. The insert shows the data at low concentrations. The diamond point at concentration "1" refers to measurements made with pure ethylene. For very low C_2H_4 concentrations, the V-T relaxation rate constant β converges to 0.46 [ms^{-1} $mbar^{-1}$].*

Therefore, relaxation of excited C_2H_4 molecules buffered in N_2 or other diatomic gases is similarly to that in monatomic gases with the main difference being the fact that N_2 collisions are more efficient and the relaxation process is thus faster (Jensen et al. [1978]). Figure 5.18 shows the measurements of the relaxation rate constant β of C_2H_4 buffered in N_2 in dependence of the C_2H_4 concentration x. The linear fit yields the relaxation rate constant

$$\beta = 4.65 \cdot x + 0.46 \quad [\mathrm{ms^{-1}\ mbar^{-1}}] \ , \tag{75}$$

where x represents the C_2H_4 concentration in N_2. At low concentration β becomes 0.46 [ms^{-1} $mbar^{-1}$].

The expected higher efficiency of N_2 collisions compared to monoatomic gas collisions with identical molar mass could not be demonstrated with our measurements. However, the relaxation rate constant for C_2H_4 buffered in N_2 is between the slower rate for Ar and the faster obtained for He. The simple comparison of the N_2 data with those of the measurements of C_2H_4 buffered in Ar-He mixtures (see Fig. 5.17) does not allow to demonstrate the expected higher efficiency of N_2 molecules in contrast to monoatomic molecules. In fact, at the mole fraction of 0.66 that corresponds to the molar mass 28 of N_2 one deduces a relaxation rate constant $\beta \approx 1.6$ [ms^{-1} $mbar^{-1}$], i.e. relaxation processes in N_2 are about 3.5 time slower than in monatomic mixtures. A different situation is obtained for relaxation processes of pure C_2H_4 (also molar mass 28). In this case, thanks to V-V energy transfers, the fastest relaxation rate constant for C_2H_4 is derived.

5.5.2 Vinyl -Chloride and -Bromide Buffered in N_2

Vinyl chloride (C_2H_3Cl) and vinyl bromide (C_2H_3Br) molecules both have a molecular structure similar to ethylene. The only difference is the fact that a hydrogen atom is substituted with either a Cl or a Br atom. Both of these vinyl molecules exhibit an absorption peak in the 10P branch of the CO_2 laser just like C_2H_4, but these are shifted to lower energies between the 10P22 and the 10P24 CO_2 laser transitions, with a more pronounced shift observed for the heavier C_2H_3Br molecule. Figure 5.19 shows the PA absorption spectrum obtained for 0.2 % C_2H_3Cl buffered in N_2 at 150 mbar and Fig. 5.20 the PA spectrum for C_2H_3Br obtained under the same conditions.

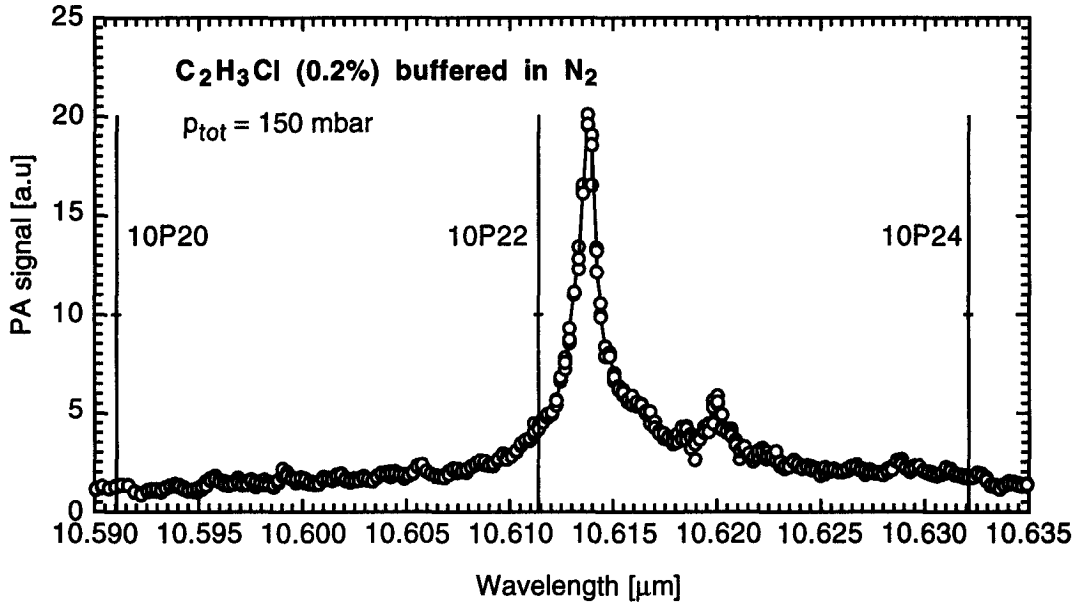

Figure 5.19. *PA spectrum of 0.2 % C_2H_3Cl in N_2 at a total pressure of 150 mbar and room temperature in the 10P CO_2 branch. The vertical lines indicate the CO_2 laser transitions.*

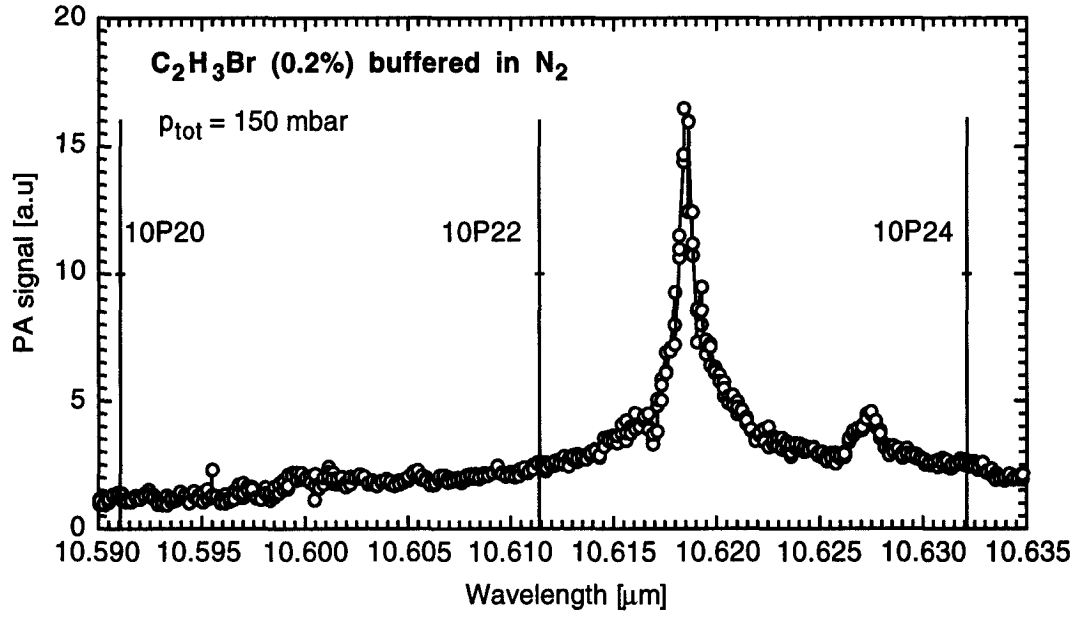

Figure 5.20. *PA spectrum of 0.2 % C_2H_3Br in N_2 at a total pressure of 150 mbar and room temperature in the 10P CO_2 branch. The vertical lines indicate the CO_2 laser transitions.*

Since these molecule have weak absorption at the wavelengths of a conventional line-tunable CO_2 laser, they have scarcely been studied, and we have found neither accurate data on absorption peak positions nor relaxation rate data. Our PA investigations yield the absorption data. Table 5.2 lists the derived peak positions and the absorption strength

relative to C_2H_4. Normalized to a total pressure of 150 mbar, the absorption strength of C_2H_3Cl is 2.0 ±0.1 and that of C_2H_3Br 2.5 ±0.1 times weaker than that of C_2H_4.

Table 5.2. *Results of the PA measurement concerning position of the absorption peak and absorption strength of C_2H_3Cl and C_2H_3Br relative to C_2H_4 in the 10P CO_2 laser branch at 150 mbar.*

	Peak wavelength ±0.005 [cm^{-1}]	Relative line strength
C_2H_3Cl	942.172	0.5
C_2H_3Br	941.752	0.4
C_2H_4	949.354	1

Relaxation measurements for C_2H_3Cl and C_2H_3Br buffered in N_2 at various concentrations have been performed with our PTBD setup. The results are presented in Figs. 5.21 and 5.22.

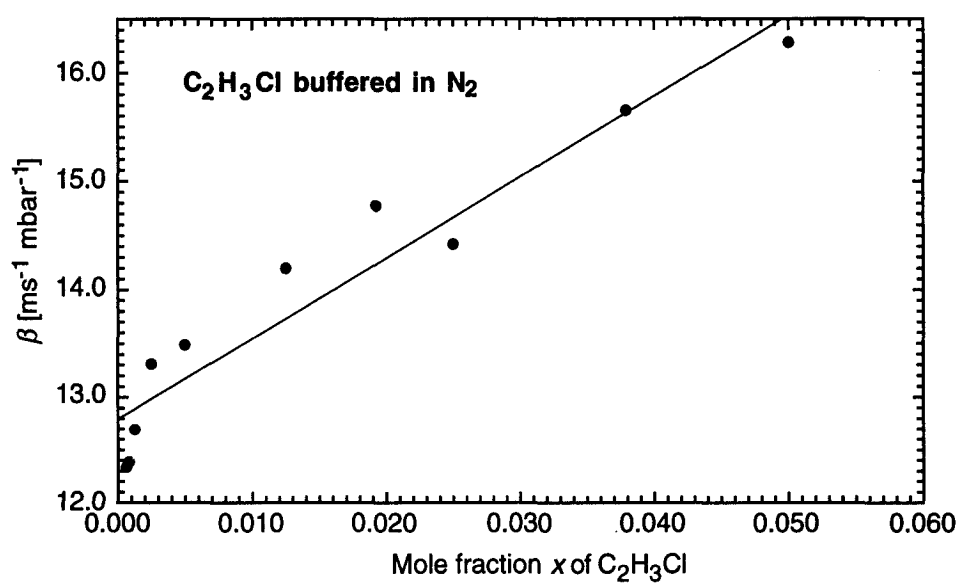

Figure 5.21. *Measurement of the relaxation rate constant β of C_2H_3Cl buffered in N_2 at various concentrations. For very low C_2H_3Cl concentrations the V-T relaxation rate constant β converges to 12.8 [ms^{-1} $mbar^{-1}$].*

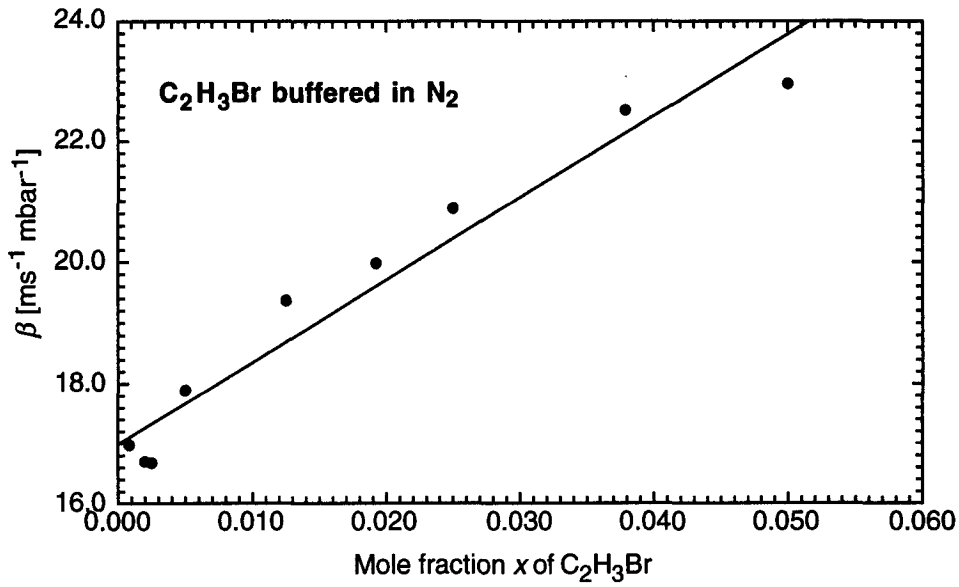

Figure 5.22. *Measurement of the relaxation rate constant β of C_2H_3Br buffered in N_2 at various concentrations. For very low C_2H_3Br concentrations the V-T relaxation rate constant β converges to 17.0 [ms^{-1} mbar^{-1}].*

The maximum concentration of 0.05 (5 %) in the measurement corresponds to the certified mixture concentration of our gas bottle. For both measurements the pump beam is tuned to the absorption peak of the investigated molecule as listed above in Table 5.2. In both figures each data point represents the averaged results of measurements performed at a total pressure of 10, 15, 20, and 30 mbar. We have deliberately chosen such a low pressure regime in order to avoid any convergent behaviour of the PTBD signal in view of fast relaxation.

The linear fit yields the following relaxation rate function for C_2H_3Cl

$$\beta = 74.7 \cdot x + 12.8 \quad [\text{ms}^{-1}\ \text{mbar}^{-1}] \tag{76}$$

with β = 12.8 [ms^{-1} mbar^{-1}] at low C_2H_3Cl concentrations.

The corresponding function for C_2H_3Br is

$$\beta = 135.9 \cdot x + 17.0 \quad [\text{ms}^{-1}\ \text{mbar}^{-1}] \tag{77}$$

with β = 17.0 [ms^{-1} mbar^{-1}] at low C_2H_3Br concentrations. A deactivation process much faster for both C_2H_3Cl and C_2H_3Br than for C_2H_4 is obtained. This behaviour originates from the asymmetric structure of both vinyl molecules which results in a more efficient V-T deactivation by collisions and a larger number of V/R energy levels where faster V-V deexcitations occur thereby distributing the stored energy rapidly. In order to further

investigate the advantageous situation of a larger number of energy levels involved in the relaxation processes, we have studied a gas mixture containing 2.5 % C_2H_3Br, 2.5 % C_2H_3Cl and 95 % N_2. In this gas mixture the vibrational states of both vinyl molecules are suitable for V-V energy transfer. The larger number of vibrational states compared to that of a single vinyl molecule should yield faster relaxation processes. This is also confirmed by a measurement where the CO_2 laser wavelength is first tuned to the absorption peak of C_2H_3Cl and then to that of C_2H_3Br. In the former case a relaxation rate constant β = 22.9 [ms^{-1} $mbar^{-1}$] is obtained, whereas in the latter case we get β = 23.7 [ms^{-1} $mbar^{-1}$]. Obviously, the deexcitation process is faster than for a single vinyl molecule where a smaller number of V-V processes is involved in the deexcitation.

5.6 Thermal Conductivity

Various procedures are available for the determination of the thermal conductivity of pure gases or gas mixtures. Simple and straightforward methods for estimating thermal conductivities of mixtures are the linear molar mixing rule (Kennard [1938]), the reciprocal mixing rule (Brokaw [1955]) and a combination of both. These schemes, however, give only a poor estimation of the thermal conductivity (Touloukian et al. [1970]). Other more sophisticated techniques are unsatisfying as well. The transient hot wire method is probably the most widely used one. This method requires that a very fine and fragile platinum wire be suspended in the sample and that it be connected to external electrical circuitry. The electrically heated wire acts as a heater as well as a thermometer. By measuring the heat input by the current and the temperature via their resistance, the dissipated energy and therefore the heat conduction can be deduced. This method already introduced by Andrews in 1840 (Andrews [1840]), remained essentially invariant. The modern versions differ primarily in the procedure adopted to eliminate, reduce, or correct for the portion of thermal energy that escapes by conduction along the wire. However, some restrictions are imposed to this method. For example, in some cases, the wire may catalyse sample decomposition making the hot wire approach impossible. Furthermore, general limitations are inherent in the instrument by the nature of its design, mode of operation, and need of calibration (Srivastava and Saxena [1957]). It is thus highly desirable to develop reliable and simple procedures for the determination of thermal conductivity in gases.

In this work, we apply the PTBD method for the measurement and the model presented in the Chap. 2 for the derivation of the thermal conductivities. The PTBD technique offers a valuable alternative to conventional methods.

Unlike the hot wire method the PTBD technique has the great advantage of being a purely optical, non-contact scheme. The PTBD method is similar to the thermal lens technique (PTL) (Bailey et al. [1980, 1981, 1982]) and requires a pump laser beam to induce thermal effects. If the gas to be analyzed does not absorb the radiation of the pump beam, traces of an absorbing gas, e.g. SF_6 or C_2H_4 if a CO_2 laser is used as pump laser, are sometimes added without affecting the thermal conductivity.

For PTBD measurements aimed at deriving relaxation rate constants, it is also possible (although net favourable) to choose a configuration with the probe beam propagating outside the pump beam, i.e. $d > r_b$ (see Fig. 5.6) whereas for thermal conductivity studies only the opposite is true, i.e. $d < r_b$. The reason for this is the fact that the induced temperature changes outside the pump beam region are substantially reduced in this case (see section 5.3).

The PTBD technique offers a simple tool to determine thermal conductivities. As example, we have studied a He/Ar and a Ar/Kr mixture containing 1 % of C_2H_4 as absorbing gas. Using the same computer implementation of equation (33) as applied for the determination of the relaxation rate constant, we have derived the thermal conductivity. The results are illustrated in Fig. 5.23.

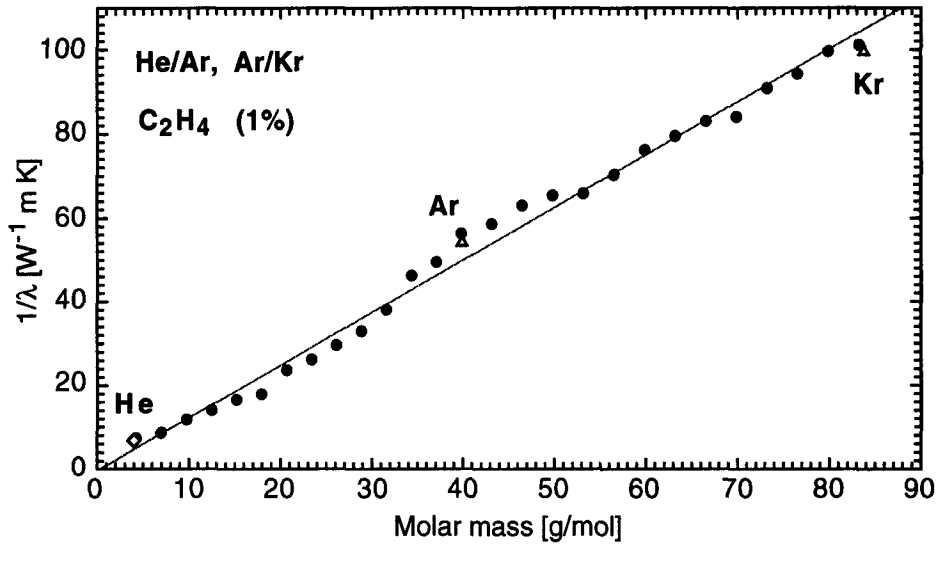

Figure 5.23. *Thermal conductivity derived from PTBD signals obtained for a He/Ar and Ar/Kr mixture containing 1 % C_2H_4 as absorbing gas. The reciprocal thermal conductivity is plotted versus the molar mass of the gas mixture. Measured data are represented by circles whereas the diamond point denotes literature data for He (Handbook of Chemistry and Physics [1977]) and the triangle points for Ar and Kr (Bailey et al. [1981]).*

Here the reciprocal thermal conductivity is plotted as a function of the molar mass of the mixture. The solid line represents a guide to the eye rather than the expected behaviour. The diamond point denotes literature data of He (Handbook of Chemistry and Physics [1977]). The triangles refers to literature data reported in Bailey and co-workers (Bailey et al. [1981]) for Ar and Kr measured with the thermal lens method. To achieve these thermal lens data the authors have added traces of SF_6 as absorbing gas to Ar and Kr and configured the experiments so that a simplified theoretical approach that neglects the influence of the generated acoustic wave could be used (Bailey et al. [1980]). In contrast, our approach is suitable under any experimental conditions and could also be applied to thermal lens experiments. In that case, the measured signal is proportional to the second derivative of the density equation (33) instead of the first derivative as in the case of the deflection (Eq. (62)). In order to facilitate the comparison between literature and measured data we list the thermal conductivity data for He, Ar, Kr in Table 5.3.

Table 5.3. *Comparison of the thermal conductivity for He, Ar and Kr in mixtures with 1 % C_2H_4 at room temperature with literature data for pure He, Ar, and Kr.*

	λ [mW m^{-1} K^{-1}] our measurement	λ [mW m^{-1} K^{-1}] literature	deviation %
He	136.0	146.8 [a]	8
Ar	17.75	18.48 [b]	4
Kr	9.88	10.05 [b]	2

[a] *Handbook of Chemistry and Physics p. E-3 [1977] at 290 K,*
[b] *Bailey et al. [1981] measured with the thermal lens method at 296 K*

The column on the right represents the relative deviation between the data. For the comparison of our results with literature data it should be considered that the gas samples are somewhat different. In our measurements the mixture contains a relatively large amount of C_2H_4 (1 %). This concentration changes slightly the actual mass of the mixture and the thermal conductivity of the gas. This is especially true for He where the largest difference occurs. The mass difference between pure He gas and our mixture with 1 % C_2H_4 amounts to 6 %. For heavier gases this effect is reduced, e.g. to 0.7 % for Kr. Furthermore, despite the rather good agreement, it should be emphasized that our experimental conditions are not optimized for the determination of thermal conductivities.

The accuracy of our data is approximately 5 %, mainly influenced by the accuracy of radial dimensions of the pump beam used to fit the measurements. This parameter has a much higher impact on the accuracy of the inferred thermal conductivity than it has on the relaxation rate constant. Hence, when thermal conductivity measurements are emphasized, the quality of both pump and probe beams needs special attention. The PTBD and thermal lens schemes are similar in this respect.

Chapter 6

Conclusions

The time-resolved gas density evolution after laser pulse excitation is theoretically described using an improved version of a model developed previously for thermal lens signals. In particular, we have included a third molecular species that takes into account that not all of the absorbers are actually excited by the laser pulse. An excellent agreement with experimental signal shapes acquired by the photothermal beam deflection (PTBD) setup is obtained, even in cases where previous models failed, e.g. for strongly different molecular masses between an absorbing gas and a light buffer gas. This novel approach is suitable for the description of acoustic signal shapes, photothermal beam deflection signals as well as thermal lens signals.

The continuously tunable CO_2 laser described in chapter 3, previously successfully applied to photoacoustic (PA) trace gas monitoring, has been applied for the first time in a PTBD study. Its broad tuning range of a total of 76 cm^{-1} in the 9 to 11 μm region and its narrow linewidth of only 0.017 cm^{-1} render it a powerful tool for spectroscopic studies. However, its low pulse repetition rate of 1 Hz, although increased from 0.2 Hz in the present study, results in time-consuming studies whenever a broad wavelength range needs to be scanned. An increase of the repetition rate to values beyond a few Hz would, however, require a new design of the laser gas flow, i.e. a change from the longitudinal to a transverse flow configuration.

To our knowledge we present the first detailed investigation concerning the dependence of temporal PA signal shapes on the microphone characteristics as encountered in pulsed, non-resonant photoacoustics. The results enable the selection of the microphone giving optimum detection performance. The key issues are as follows: i) The peak amplitude of the recorded microphone signal increases with decreasing laser beam radius r_b. However, for standard microphones with a bandwidth of ≈ 20 kHz, there is no reason to use $r_b < 0.5$ mm because the spectral composition of the signal shape for frequencies < 20 kHz remains unchanged. ii) A large microphone bandwidth of a few 100 kHz that is capable of resolving the temporal evolution of the PA signal is actually disadvantageous for trace gas monitoring. In fact, the general relation between microphone bandwidth and responsivity (Eq. (43)), as well as the occurrence of external noise imply a reduction of the SNR for very large microphone bandwidths (see Eq. (44)). iii) We introduce an analytical function that allows the simulation of the measured SNR

for a given microphone specification. Such simulation permits the selection of the most appropriate microphone for maximum SNR.

An additional improvement in detection sensitivity is achieved by adding the signals of several microphones. In such a configuration the signal increases with the number of microphones used, whereas the microphone random noise decreases with the square root of their number. Electret microphones are particularly suited owing to their small size which enables the integration of a large number of microphones even in a small volume. Further improvements can be expected by inserting an electrical filter which cuts the low frequency components of the signal (up to 1 kHz) that contribute less to the increase of the SNR than do higher frequencies. Furthermore, the frequency response of the microphone pre- and amplifier stages should be similar to that of the microphone in order to fully exploit all the sensed frequency contributions except noise components at frequencies not contributing to the acquired signal.

The excellent performance of the system, particularly with respect to detection selectivity, is demonstrated in a study on a mixture of six CO_2 isotopes ($^{12}C^{16}O_2$, $^{12}C^{18}O_2$, $^{13}C^{16}O_2$, $^{13}C^{18}O_2$, $^{16}O^{12}C^{18}O$, $^{16}O^{13}C^{18}O$). Besides the quantitative determination of the individual concentrations, previously unknown absorption cross sections of three of the isotopes could be derived. It should be emphasized that the capability of analyzing isotopic gas mixtures without any pretreatment or preconcentration is of great interest in different fields like biology, medicine or planetary science.

Apart from the detection selectivity, the achievable sensitivity is another key issue. Besides the proper selection of the microphone, the sensitivity is essentially determined by the absorption strength of the species under study, and thus by the wavelength range of the laser used. In this respect, the CO_2 laser range is far from optimum for detecting CO_2, in fact a 10^5 fold better sensitivity permitting the detection of 10 ppb concentration level appears feasible when measuring in the 4.26 μm wavelength region where CO_2 exhibits maximum absorption. However, at present tunable primary lasers at this wavelength are not yet readily available. In this respect, sources based on difference frequency mixing are very promising. Of course, the method is not restricted to certain isotopes but can be extended to any other multicomponent mixture depending on the availability of tunable narrowband sources.

We have not only applied photoacoustics to trace gas detection but also to study molecular dynamics in gases. The information on relaxation time present in a PA pulse does not differ from that present in the signal shape obtained by other detection methods based on sensing the density variation such the photothermal beam deflection (PTBD) or the thermal lens (TL) scheme: This implies that for equal SNR in a measurement performed with these photothermal detection methods, identical relaxation times and

accuracy are expected. This can be easily demonstrated mathematically using the density equation (33). However, for relaxation time measurement with PA methods, piezoelectric transducers with a large bandwidth were previously used (Beck and Gordon [1988]). Due to their low responsivity and consequently low SNR, these sensors are not ideal for that purpose. In order to perform time-resolved investigations on the molecular dynamics of gas molecules, the photothermal beam deflection (PTBD) scheme is preferable. The PTBD technique senses the gas density variation after laser pulse excitation optically with a probe laser beam and allows measurements inside and outside of the gas region excited by the pump laser beam. The maximum SNR is obtained at a distance $d = r_b/\sqrt{2}$ between pump beam (radius r_b) and probe beam.

PTBD schemes have also been used for trace gas studies (Vries [1994]). In that case the signal amplitude is important and small pump radii ($r_b < 0.5$ mm) are advantageous for high sensitivity. In contrast, the temporal signal profile is essential for studies on molecular dynamics. This implies the use of laser pump radii of a few mm in order to reduce the effect of misalignment between pump and probe beam.

We present a new concept which permits optimization of experimental parameters, essentially r_b and d, to derive relaxation times in the μs range with a specified accuracy for a given SNR.

Vibrational-translational (V-T) relaxation rates as well as thermal conductivity data were deduced from our PTBD measurements on gas mixtures. Besides the discussion of many new data, the good agreement with results from previous investigations performed by other methods is emphasized. Accurate results can only be obtained if the pump beam profile is well known. This is even more true for thermal conductivity data than for the relaxation rates.

Finally, it should be pointed out that the PTBD scheme is a rather simple method which can also be applied in aggressive environments owing to its contact-less character. It should be kept in mind, however, that PTBD senses exclusively V-T relaxation processes and does not provide information on other intramolecular energy transfers such as for example V-V processes.

References

T. Andrews [1840]
Proc. Roy. Irish Acad. **1**, 465

R.T. Bailey, F.R. Cruickshank, D. Pugh and W. Johnstone [1978]
The time resolved geometrical optics of thermal lens
Chem. Phys. Lett. **59**(2), 324-329

R.T. Bailey, F.R. Cruickshank, D. Pugh, and W. Johnstone [1980]
Pulsed Source Thermal Lens, Part 1. Theoretical Analysis
J. Chem. Soc., Faraday Trans. II **76**, 633-647

R.T. Bailey, F.R. Cruickshank, D. Pugh, and W. Johnstone [1981]
Pulsed-suorce Thermal Lens, Part 2. Experimental Tests of the Theory
J. Chem. Soc., Faraday Trans. II **77**, 1387-1397

R.T. Bailey, F.R. Cruickshank, D. Pugh, A. McLeod and W. Johnstone [1982]
Gas Phase Thermal Diffusivities by a Thermal Lens Technique
Chem. Phys. North-Holland **68**, 351-357

R.T. Bailey, F.R. Cruickshank, D. Pugh, and K. M. Middleton [1985]
Vibration-Vibration Energy -transfer Kinetics Monitored by Thermal Lens
J. Chem. Soc., Faraday Trans. II **81**, 255-265

J.R. Barker and T. Rothem [1982]
Theory of the time-dependent-thermal-lensing (TDTL) technique as used in energy-transfer experiments
Chem. Phys., North-Holland **68**, 331-339

J.R. Barker and B.M. Toselli [1988]
"Photothermal studies of energy transfer and reaction rates"
in *Photothermal investigations in solids and fluids*
J.A. Sell, ed., Academic Press, New York, pp. 155-190

K.M. Beck, R.J. Gordon [1988]
Theory and application of time-resolved optoacoustic in gases
J. Chem. Phys. **89**(9), 5560-5567

S.E. Bialkowski [1996]
Photothermal Spectroscopy Methods for Chemical Analysis
Chemical Analysis, Vol. 134, J. Wiley & Sons, Inc., New York

A.C. Boccara, D. Fournier and J. Badoz [1979]
Thermo-optical spectroscopy by the 'mirage effect'
Appl. Phys. Lett. **36**(2), 130-132

R.S. Brokaw [1955]
Estimating Thermal Conductivities for Nonpolar Gas Mixtures Simple Empirical Method
Ind. Eng. Chem. **47**, 2398-2400

Brüel & Kjær [1982]
Condenser Microphones and Microphone Preamplifiers for acoustic measurements
Data Handbook, Brüel & Kjær

I.G. Calasso, M. Chirtoc and M.W. Sigrist [1996]
Time-resolved photothermal studies on gas mixtures with continuously tunable high pressure CO_2 laser
9th International Conference on Photoacoustic and Photothermal Phenomena,
Progress in Natural Science **6**, S 618-S 621, 1996

I.G. Calasso, V. Funtov and M.W. Sigrist [1997]
Analysis of isotopic CO_2 mixtures by laser photoacoustic spectroscopy
Appl. Opt. **36**(15), 3212-3216

I.G. Calasso, I. Delgadillo and M.W. Sigrist [1998]
Modelling and analysis of experimental photothermal beam deflection signals in gases
Chem. Phys. **229**, 181-191

F. Cannemeyer and A.E. de Vries [1974]
Vibrational Relaxation of CO_2 in CO_2-N_2 and CO_2-O_2 Mixtures
Physica **74**, 196-204

T.L. Cottrell [1965]
Dynamic Aspects of Molecular Energy States
Universiy Chemical Texts, Oliver & Boyd, Edinburgh and London

D.A. Cremers and R.A. Keller [1982]
Thermooptic-based differential measurements of weak solute absorption with an interferometer
Appl. Opt. **21**(9), 1654-1662

C.C. Davis and S.J. Petuchowski [1981]
Phase fluctuation optical heterodyne spectroscopy of gases
Appl. Opt. **20**(14), 2539-2554

G.J. Diebold [1989]
"Application of the Photoacoustic Effect to Studies of Gas Phase Chemical Kinetics"
in *Photoacoustic, Photothermal and Photochemical Processes in Gases*
P. Hess, ed., Topics in Current Physics, Springer-Verlag, pp. 125-172

G.J. Ernst [1983]
Compact Uniform-Field Electrode Profiles
Opt. Commun. **47**, 47-51

G.J. Ernst [1984]
Uniform-Field Electrodes with Minimum Width
Opt. Commun. **49**, 275-277

W.H. Flygare [1968]
Molecular relaxation
Accounts of chemical research **1,** 121-127

W.H. Flygare [1978]
Molecular Structure and Dynamics,
Prentice Hall, Englewood Cliffs, New Jersey

G.W. Flynn [1973]
"Laser-Induced Fluorescence and Absorption Studies of Molecular Energy Transfer in Gases"
in *Fundamental and Applied Laser Physics*
M. S. Feld, A. Javan, and A. Kurnit, eds., Wiley, New York, pp. 277-292

D. Fournier, A.C. Boccara, N.A. Amer and R. Gerlach [1980]
Sensitive in situ trace-gas detection by photothermal deflection spectroscopy
Appl. Phys. Lett. **37**(6), 519-521

D. Fournier and A.C. Boccara [1988]
"Photothermal investigation of solids: basic physical principles"
in *Photothermal investigations in solids and fluids*
J.A. Sell, ed., Academic Press, New York, pp. 35-79

V.N. Funtov, A.M. Nemets, V.M. Nemets, A.A. Petrov and A.A. Soloviov [1992]
Isotopic spectral analysis of inorganic gases
Analyst **117**, 1049-1054

M.-C. Gagné and S.L. Chin [1991]
Energy Relaxation Time in a Gas Mixture Measured by a Photothermal Probe Beam Deflection Technique
Appl. Phys. B **52**, 352-358

F.G. Gebhardt and D.C. Smith [1972]
Kinetic Cooling of a Gas by Absorption of CO_2 Laser Radiation
Appl. Phys. Lett. **20**(3), 129-132

F.R. Grabiner, D.R. Siebert, and G.W. Flynn [1972]
Laser induced time-dependent thermal lensing studies of vibrational relaxation: translational cooling in CH_3F.
Chem. Phys. Lett. **17**(2), 189-194

J. Häger, W. Krieger, and T. Rüegg [1979]
Vibrational energy transfer in ethylene and ethylene-rare-gas mixtures
J. Chem. Phys. **70**(6), 2859-2863

Handbook of Chemistry and Physics [1977]
57th edition, CRC press

G. Herzberg [1991]
Infrared and Raman Spectra of Polyatomic Molecules
Krieger, Malabar, Florida

J.O. Hirschfelder, C.F. Curtiss and R.B. Bird [1964]
Molecular theory of gases and liquids
John Wiley & Sons Inc., New York

J.M. Hollas [1982]
High Resolution Spectroscopy
Butterworth, London

W.B. Jackson, N.M. Amer, A.C. Boccara and D. Fournier [1981]
Photothermal deflection spectroscopy and detection
Appl. Opt. **20**(8),1333-1344

J.D. Jackson [1983]
Klassische Elektrodynamic
J. D. Jackson, ed., 2. Auflage, Walter de Gruyter, Berlin

S.J. Jacobs [1989]
The Fluid Mechanics of Photothermal Systems
Chem. Phys. **132**, 71-81

T. Jaeger and G. Wang [1987]
"Tunable Lasers"
in *Topics in Applied Physics* ***59***
L. F. Mollenauer and J. C. White, eds., Springer-Verlag, Berlin

C.C. Jensen, J.I. Steinfeld, and R.D. Levine [1978]
Information theoretic analysis of multiphoton excitation and collisional deactivation in polyatomic molecules,
J. Chem. Phys. **69**(4), 1432-1439

E.H. Kennard [1938]
Kinetic Theory of Gases, With an Introduction to Statistical Mechanics
McGraw-Hill Book Company, New York and London

R. Kesselring, A.W. Kälin, H.J. Schötzau, and F.K. Kneubühl [1993]
Picosecond CO_2 Laser-Pulse Generation and Amplification
IEEE J. Quant. Electr. **29**(3), 997-1005

L.E. Kinsler, A.E. Frey, A.B. Coppens, J.V. Sanders [1982]
Fundamentals of Acoustics
John Wiley & Sons, New York

J. Knittel, D.P. Scherrer, and F.K. Kneubühl [1995]
High-Pressure Single-Mode CO2 Laser with ps Plasma Shutter
Opt. Eng. **34**, 2000-2016

J.D. Lambert [1977]
Vibrational and Rotational Relaxation in Gases
J.D. Lambert, Clarendon Press, Oxford

N. Melander [1997]
Adsorption under near ambient conditions
PhD Thesis, University of Copenhagen, Denmark

P.L. Meyer and M.W. Sigrist [1990]
Atmospheric Pollution Monitoring Using CO_2-Laser Photoacoustic Spectroscopy and other Techniques
Rev. Sci. Instr. **61**(7), 1779-1807

P.M. Morse [1936]
Vibration and Sound
P.M. Morse, McGraw-Hill Book Company, Inc., New York and London, 1936

W.H. Press, B.P. Flannery, S.A. Teukolsky, W.T. Vetterling [1992]
Numerical recipes - the art of scientific computing
University Press, Cambridge

D. Pugh [1989]
"Theoretical Foundation of Photoacoustic in the Frequency and Time Domains"
in *Photoacoustic, Photothermal and Photochemical Processes in Gases*
P. Hess, ed., Topics in Current Physics, Springer-Verlag, pp. 15-36

D.N. Raouf [1987]
UV and X-ray Preionized High-Pressure CO_2 Lasers and Line Narrowing for Spectroscopic Studies
PhD Thesis, University of Hull, England

P. Repond and M.W. Sigrist [1994]
Photoacoustic spectroscopy on gases with high pressure continuously tunable CO_2 laser
J. de Phys IV, Coll. C7, supplément de Physique III, **4**, C7-523 - 525

P. Repond [1995]
Photoacoustic Spectroscopy on Gases with a Continuously Tunable High Pressure CO_2 Laser
PhD Thesis No. 11047, Swiss Federal Institute of Technology, Zürich, Switzerland

P. Repond and M.W. Sigrist [1996 /1]
Continuously Tunable High-Pressure CO_2 Laser for Spectroscopic Studies on Trace Gases
IEEE J. Quant. Electr. **32**(9), 1549-1559

P. Repond and M.W. Sigrist [1996 /2]
Photoacoustic Spectroscopy on Trace Gases with continuously tunable CO_2 Laser
Appl. Opt. **35**(21), 4065-4085

L.G. Rosengren [1975]
Optical optoacoustic detector design
Appl. Opt. **14**(8), 1960-1976

L.S. Rothman, R.R. Gamache, R.H. Tipping, C.P. Rinsland, M.A.H. Smith, D.C. Benner, V. Malathy Devi, J.-M. Flaud, C.Camy-Peyret, A. Perrin, A. Goldman, S.T. Massie, L.R. Brown, and R.A. Toth [1992 /1]
The Hitran molecular database: editions of 1991 and 1992
J. Quant. Spectrosc. Radiat. Transfer **48**(5/6), 469-507

L.S Rothman, R.L. Hawkins, R.B. Wattson, R.R. Gamache [1992 /2]
Energy levels, intensities, and linewidths of atmospheric carbon dioxide bands
J. Quant. Spectrosc. Radiat. Transfer **48**(5/6), 537-566

J.S. Rowlinson [1961]
The rate of molecular collisions in gases composed of 'soft' molecules
Molec. Phys. **4**, 317-320

S. Schäfer [1997]
Quantitative Analyse des photoakustischen Signals bei gepulster Laseranregung
PhD Thesis, University of Heidelberg, Germany

R. N. Schwartz, Z. I. Slawsky, K. F. Herzfeld [1952]
Calculation of Vibrational Relaxtion Times in Gases
J. Chem. Phys. **20**(10), 1591-1599

R.N. Schwartz and K.F. Herzfeld [1954]
Vibrational Relaxation Times in Gases (Three-Dimensional Treatment)
J. Chem. Phys. **22**(5), 767-773

H.K. Shin [1972]
Temperature Dependence of Vibrational Transition Probabilities for O_2, N_2, CO, and Cl_2 in the Region below 300 K
J. Chem. Phys. **57**, 1363-1364

D.R. Siebert, F.R. Grabiner and G.W. Flynn [1974]
Time-resolved thermal lensing studies of laser-induced translational energy fluctuations in CD_4, SO_2, and OCS^*
J. Chem. Phys. **60**(4), 1564-1574

M.W. Sigrist [1994]
Air Monitoring by Spectroscopic Techniques
M.W. Sigrist., ed., J. Wiley & Sons, New York

W.L. Smith and I.M. Mills [1964]
Coriolis Perturbations in the Infrared Spectrum of Ethylene
J. Chem. Phys. **40**(8), 2095-2109

H. Sontag, A.C. Tam and P. Hess [1987]
Energy relaxations in CS_2 and in NO_2-N_2O_4 vapors following pulsed laser excitation at 337.1 nm by probe beam deflection measurements
J. Chem. Phys. **86**(7), 3950-3958

B.N. Srivastava and S.C. Saxena [1957]
Thermal Conductivity of Binary and Ternary Rare Gas Mixtures
Proc. Phys. Soc. (London) Section B **70**, part 1, 369-378

J.I. Steinfeld, J.S. Francisco, W.L. Hase [1989]
Chemical Kinetics and Dynamics
Prentice Hall, Englewood Cliffs, New Jersey, Chap. 13

A.C. Tam, H. Sontag and P. Hess [1985]
Photothermal probe beam deflection monitoring of photochemical particulate production
Chem. Phys. Lett. **120**(3), 280-284

A.C. Tam [1986]
Applications of photoacoustic sensing techniques
Rev. of Mod. Phys. **58**(2), 381-431

B.M. Toselli, T.L. Walunas and J.R. Barker [1990]
Time dependent thermal lensing measurements of V-T energy transfer from highly excited NO_2
J. Chem. Phys. **92**(8), 4793-4804

Y.S. Touloukian, P.E. Liley, S.C. Saxena [1970]
Thermal conductivity, Nonmetallic Liquids and Gases
in Thermophysical Properties of Matter **3**, IFI/Plenum, New York-Washington

H.S.M. de Vries [1994]
Local trace gas measurements by laser photothermal detection; physics meets physiology
PhD Thesis, Katholieke Universiteit Nijmegen, Nederlands

E. Weitz and G. Flynn [1974]
Laser studies of vibrational and rotational relaxation in small molecules.
Ann. Rev. Phys. Chem. **25**, 275-315

U. Werling [1988]
Entwicklung eines abstimmbaren Hochleistungslasersystems für die nichtlineare Spektroskopie in fernen Infrarot
PhD Thesis, University of Regensburg, Germany

J.R. Whinnery [1967]
Thermal Convection and Spherical Aberation Distortion of Laser Beams in Low-Loss Liquids
IEEE J. Quant. Electr. **QE-3**, 382-383

W.J. Witteman [1987]
The CO_2 laser
Springer Series in Optical Sciences, Vol. 53, Springer-Verlag, Berlin

A.D. Wood, M. Camac, and E.T. Gerry [1971]
Effects of 10.6-μ Laser Induced Air Chemistry on the Atmospheric Refractive Index
Appl. Opt. **10**(8), 1877-1884

R.C.L. Yuan and G.W. Flynn [1973/1]
*Laser induced combination band fluorescence study of vibrational deactivation of ethylene in C_2H_4-X mixtures**
J. Chem. Phys. **58**(2), 649-655

R.C.L. Yuan, J.M. Preses, and G.W. Flynn [1973/2]
V-V and V-T/R energy transfer studies of C_2H_4 by infrared laser double resonance
J. Chem. Phys. **59**(11), 6128-6135

Acknowledgements

I am deeply obliged to Prof. Dr. M.W. Sigrist for giving me the opportunity to work on this project and for his engaging support during the course of this work. I am grateful to Prof. Dr. H. Melchior and to Dr. W. Faubel (Forschungszentrum Karlsruhe, Germany) for their interest and comments on my thesis and I owe special thanks to Prof. Dr. D.D. Bicanic (Wageningen University, The Netherlands) for all the interesting discussions and comments on my thesis.

I would further like to express my thanks to Dr. Isabell Delgadillo and to Dr. Mihai Chirtoc for their friendly and fruitful collaboration.

I am very grateful to Prof. Dr. F.K. Kneubühl, and to the all members of the Infrared Physics Laboratory at ETH, all of whom contributed in some way to the success of this project. In particular, I acknowledge the inspiring discussions by my colleague and friend Dr. Francesco Pepe. For the fruitful collaboration I would like to thank my colleagues and friends Dr. Andreas Bohren with whom I shared the laboratory during these years, Albert Romann, Markus Naegele, Michael Seiter, and Dr. Mark Moeckli. It was a great pleasure to work with them.

I am obliged to all of the technical staff. In particular special thanks go to Josef Böhi, Bruno Nussberger, Edwin Treichler and Eveline Trüb. I appreciate their always friendly and open manner and hold them in high regard for their competence.

Furthermore, I wish to express my thanks to the branch of the Brüel & Kjaer Company in Switzerland, and in particular to Harald Meierhofer for allowing me to test the microphones and for supplying information regarding these microphones.

Profonda stima e gratitudine va a Domenico A. Vitale. La sua guida da insegnante nel periodo scolastico medio e superiore e poi la sua amicizia mi hanno segnato particolarmente.

Ringrazio i miei genitori per avermi sostenuto per lungo tempo e sempre incoraggiato nella mia scelta professionale.

In fine, ma non per ultimo, un sincero grazie va a Graziella Ambrosio che apprezzo e stimo e che con la quale condivido sia una fantastica bambina di nome Lara Francesca che i momenti felici e meno felici della vita.

This study was supported by the Swiss National Science Foundation and ETH Zürich.

Curriculum Vitae

1966 born in Melendugno (Lecce), Italy

1972-1980 primary and secondary education completed in Italy and Switzerland,

1980-1984 Italian high school in Zugerberg (Switzerland), Maturità Scientifica

1985 entrance examination at the Swiss Federal Institute of Technology (ETH)

1985-1994 study and employments:

study: Physics at the Swiss Federal Institute of Technology (ETH), Zürich

employments:
- 8 years as an instructor in Computer Science at the School for Further Education of Adults ECAP, Zürich
- 4 years as a high school teacher in Computer Science at the high school Liceo Linguistico Vermigli, Zürich
- diversity of other positions held

1994 Diploma Thesis (M.S.) in Quantum Electronics,
"Q-Switching" - Instabilität in passiv - modengekoppelten Festkörperlaser
at the Laboratory of Ultrafast Laser Physics, ETH Zürich
under the supervision of Dr. F.X. Kärtner and Prof. Dr. U. Keller

1994-1998 Teaching Assistant in Laboratory Sessions, as well as
in courses in Physics, Laser Physics and Quantum Electronics
taught by Prof. Dr. J. Bilgram, Prof. Dr. F.K. Kneubühl,
Prof. Dr. H.R. Ott and Prof. Dr. M.W. Sigrist

1998 Ph.D. Thesis,
Photoacoustic and Photothermal Laser Spectroscopy Applied to Trace Gas Detection and Molecular Dynamics